2015

High resolution mass spectrometry for molecular characterization of pyrolysis products and kinetics

Daniel Paul Cole
Iowa State University

High resolution mass spectrometry for molecular characterization of pyrolysis products and kinetics

by

D. Paul Cole

A dissertation submitted to the graduate faculty

in partial fulfillment of the requirements for the degree of

DOCTOR OF PHILOSOPHY

Major: Analytical Chemistry

Program of Study Committee:
Young-Jin Lee, Major Professor
R. Sam Houk
Emily A. Smith
Thomas A. Holme
Javier Vela
Mark Mba Wright

Iowa State University

Ames, Iowa

2015

TABLE OF CONTENTS

NOMENCLATURE

HRMS	High Resolution Mass Spectrometry
FTICR	Fourier Transform Ion Cyclotron Resonance
TOF	Time-of-Flight
MS	Mass Spectrometer
GC	Gas Chromatography
M/Z	Mass-to-charge
ESI	Electrospray Ionization
APPI	Atmospheric Pressure Photoionization
APCI	Atmospheric Pressure Chemical Ionization
EI	Electron Ionization
µPy	Micropyrolysis
DBE	Double bond equivalent
BIO-OIL	Biomass Pyrolysis Oil
SYNGAS	Synthesis Gas
PAH	Polyaromatic Hydrocarbon
CFP	Catalytic Fast Pyrolysis

ACKNOWLEDGMENTS

I would foremost like to thank my major professor, Young-Jin Lee, for the opportunity to join his group and develop into the analytical chemist I am today. I cannot fully state his importance in contributing to my success as a graduate student, such as providing opportunities to experience mass spectrometry at annual American Society of Mass Spectrometry conferences or recommendations that bestowed fellowships, honors, and awards. He has been a constant role model and mentor that challenged me to become a better scientist and person. I especially admire his brilliance, cleverness, and dedication to overcome obstacles and diversity. I would like to thank my committee members, R. Sam Houk, Emily Smith, Thomas Holme, Javier Vela, and Mark Mba Wright, for their guidance and support throughout my research.

In addition, I would also like to thank my fellow Lee group colleagues, especially Carolyn Hutchinson and Erica Dalluge, for their helpful suggestions and conversation throughout my graduate research experience. I extend my appreciation to Brown group members for their collaboration, which provided samples, ideas, and assistance. I want to also offer my thanks to Dave Appy, Zak Weinstein, Mark Juetten, and other friends for their unwavering friendship and entertainment in activities away from research that made my time at Iowa State University a wonderful experience.

I would like to thank my parents, Russ and Tae Cole, and my brother, Tim, for their love, encouragement, and confidence that saw me through my adventure. They have sacrificed far more than I can ever repay in order to put me in a position to succeed and realize my dreams. Last, I would like to thank Sidra Akhter for her love and affection that saw me through my highs and lows during my PhD.

Although he may never read my acknowledgment, I would like to thank Professor Bruce Mattson at Creighton University for the most enjoyable and entertaining General Chemistry course that made me realize that majoring in mathematics was ridiculous and that chemistry was not only exciting, but practical and fulfilling. Through his energy, humor, and teaching, I embraced chemistry as my destiny and began my journey into molecules and beyond.

This acknowledgment is for Lynette Edsall, the best Graduate Student Services Specialist ever. I would like to offer my appreciation for keeping me informed on all deadlines and everything else you have done for me.

ABSTRACT

In recent decades, thermochemical conversion of biomass, such as pyrolysis, has gained popularity as a source for renewable materials. Pyrolysis generates three products: biochar that has shown promise as a soil amendment and carbon sequestration agent, bio-oil that could supplement petroleum-based products and transportation fuel, and syngas that is useful for ammonia, methanol, or hydrocarbon/aromatic production. At the molecular level, these samples are complex and difficult to analyze, which creates a bottleneck for thorough understanding. This dissertation utilizes high-resolution mass spectrometry (HRMS) to overcome the sample complexity and improve understanding at the molecular level.

HRMS was applied to understanding organic molecules entrapped in biochar during pyrolysis and gasification of switchgrass. Extraction of organic molecules used toluene and a mixture of water/methanol for hydrophobic aromatic compounds and hydrophilic polar compounds, respectively. Orbitrap mass spectrometric data acquisition revealed that molecular compounds previously known in bio-oils were observed for fast pyrolysis biochar, whereas polycyclic aromatic hydrocarbons (PAHs) with various ring sizes were observed for gasification and slow pyrolysis biochars.

Bio-oils from fast pyrolysis of switchgrass harvested at various times throughout the year were studied using high-resolution mass spectrometry. Nearly three hundred total nitrogen-containing species were detected through efficient ionization and accurate mass information. Nitrogen-containing species, particularly N_2 compounds, were highly abundant for early summer bio-oils, but decrease significantly in later harvest times. Contour plots of double bond equivalent (DBE) versus carbon number and tandem mass spectrometric analysis were utilized to

determine the major structural motif for N_1 and NO class compounds as pyridine and N_2 class compounds as imidazole. The dramatic decrease in nitrogen compounds correlates to the decomposition of proteins as the perennial plant senesces.

Catalytic deoxygenation of cellulose pyrolysis was evaluated using micropyrolyzer-gas chromatography (μPy-GC) coupled to dopant-assisted atmospheric pressure chemical ionization (dAPCI) time-of-flight mass spectrometry (TOF MS). A vast majority of compounds produced via catalysis and/or pyrolysis cannot be found in the database. However, dAPCI-TOF MS produces soft ionization and accurate mass measurement for direct chemical composition analysis of GC-separated molecules. This analytical technique demonstrated the ability to evaluate catalytic efficiency and monitor the change in reaction products. A total of 142 compounds could be analyzed with this approach compared to 38 compounds in traditional Py-GC-EI-MS analysis.

Finally, HRMS is utilized for the real-time monitoring of fast pyrolysis products of glucose-based carbohydrates. The soft ionization and rapid-scanning capabilities provided new insights into molecular-level understanding of pyrolysis chemistry. Comparing time evolution profiles and yields for individual products revealed that hydrogen bonding may play a larger role in degradation of cellulose and that cyclodextrin does not appear to be a good surrogate for understanding cellulose pyrolysis. More work is necessary to piece together all the information, but the first steps have been taken toward unraveling the complex network of elementary reactions.

CHAPTER I

INTRODUCTION

Short Discourse on (High Resolution) Mass Spectrometry

Mass spectrometry is a vital, ubiquitous, and powerful analytical tool in chemistry, biochemistry, biology, pharmaceuticals, and many other fields. Some knowledge of mass spectrometry is required for virtually all researchers in these areas. Sequencing biomolecules, molecular distribution in tissues, structural elucidation and identification of unknowns, environmental sampling, and quality control of drugs and food are a few examples of mass spectrometry applications [1-6].

Mass spectrometry operates on the basic principle of generating gas phase ions, separating these ions by mass-to-charge ratios (*m/z*), and detecting the individual ions by *m/z* and abundance. Ionization can occur through numerous means: thermally, electric fields, energetic electrons, ions, or photons [7]. Separating the ions by *m/z* is achieved by passing the ions through electric or magnetic fields, or even field-free zones as demonstrated by time-of-flight analyzers. The final piece is detecting the ions, which occurs when the charged species induce or produce a current. Charged molecules either oscillate near a pair of metal plates to produce an image current (cf. Fourier transform ion cyclotron resonance and orbitrap MS) or impact a surface to produce a signal (cf. electron multiplier or multichannel plate detectors).

Early mass spectrometry involved low-resolution instruments used for the discovery of stable elemental isotopes, separating isotopes of uranium for the Manhattan Project, and quantitative gas analysis when coupled with gas chromatography (GC) [8-11]. The earliest mention of high-resolution instrumentation for organic analysis appears in a 1951 letter to the

editor by Berry and Rock describing improvements to resolve isobaric peaks such as N_2^+ and $C_2H_4^+$ that have a mass difference of 0.09% at *m/z* 28 [12]. In fact, high-resolution instruments were improving upon *mass accuracy*, and as noted by VanLear and McLafferty, a better term might actually be "high mass-accuracy" mass spectrometry [13]. Thus, improving the mass accuracy measurements of ions beyond nominal values (i.e., adding more decimals to measured values) enabled more peaks to be resolved in a spectrum. Combined with high sensitivity and large data sets, mass spectrometry suddenly became useful in more applications such as drug analysis in biological assays or petroleum fractions [14,15].

Recent advances in Fourier transform MS (FTMS) and ionization techniques has pushed mass spectrometry even further, ushering in a new era of data analysis due to the extreme capabilities to resolve large number of molecules. For example, Fourier transform ion cyclotron resonance mass spectrometers (FTICR MS) have achieved mass resolving powers exceeding 1,000,000 and sub-ppm mass accuracies [16]. Put into perspective, an electron measures 0.0005486 u in a mass spectrum, which requires 2.7 ppm mass accuracy at *m/z* 200. The FTICR MS can easily differentiate the loss of a single electron! Using FTICR MS, Marshall and co-workers were able to assign chemical compositions to over 20,000 compounds in petroleum oils [17]. Terms such as "petroleomics" and "metabolomics" were coined as a result of systematic methods of analyzing and understanding complex data sets at the molecular level [17,18].

Biochar and Bio-oil: Production and Characterization

Thermochemical conversion of biomass offers an attractive means for producing biorenewable materials. Pyrolysis thermally decomposes organic matter to generate solid, liquid, and gas products termed biochar, bio-oil, and syngas, respectively. Process temperature,

residence time, and amount of oxygen during conversion are key parameters to maximize the yield of certain products [19,20]. Slow pyrolysis uses process temperatures between 300−800 °C without oxygen for long residence times (from 1 h to days) to favor biochar production. Fast pyrolysis also occurs in the absence of oxygen but at moderate temperatures between 400−600 °C with short residence times (normally < 2 s) to maximize bio-oil. Last, gasification employs controlled amounts of oxygen and high temperatures between 750−900 °C to increase conversion to syngas comprised mainly of CO and H_2 [19,20].

Biochar is the blackened remnants of thermally degraded biomass that closely resembles charcoal. Recent studies for biochar applications have shown positive benefits as a soil amendment and a carbon sequestration agent [21-24]. These studies observed soil quality improvements through increased moisture and nutrient retention, increased microbial activity, and decreased bioavailability of organic contaminants [25-27]. Biochar can be produced from biomass and municipal waste and through various thermochemical processes [28]. All factors contribute to diverse biochar properties that require thorough analysis prior to its use.

Commonly employed analysis techniques of biochar include Fourier transform infrared (FTIR) and ^{13}C nuclear magnetic resonance (NMR) [29-31]. Brown and co-workers utilized both techniques to effectively characterize biochars from various thermochemical conversion processes and feedstocks. For example, FTIR spectra showed oxygen-containing functional groups were most dominant in fast pyrolysis spectra, weak in slow pyrolysis, and nearly absent in gasification. However, FTIR and NMR generally provide average functional group information and do not provide individual molecular-level information. GC−MS has been used to study volatile organic compounds (VOCs) within biochar through headspace desorption [32]. Spokas et al. identified over 140 unique compounds but were limited to volatile gases with

molecular weights mostly below 100. Recent application of HRMS achieved more comprehensive understanding of individual organic molecules. Several studies employing FTICR MS have successful characterized hundreds of organic molecules on biochar and dissolved organic matter from naturally degraded charcoal [33,34]. Comprehensive molecular-level understanding of biochar is important prior to soil application due to leeching of potentially harmful chemicals [27,35].

Bio-oil is a dark brown, biphasic liquid product containing an aqueous and an oily phase. Although physically resembling petroleum crude oils, bio-oil is chemically much different in composition. Petroleum crude generally lacks oxygen content whereas bio-oil can contain up to 50 wt% of oxygen arising from biomass composition, namely glucose and phenol-based degradation products from hemicellulose/cellulose and lignin biopolymers, respectively [36,37]. The oxygen content is problematic for most applications, especially in the transportation fuel sector, which causes the bio-oil to be unstable, corrosive, and immiscible with current hydrocarbon fuels [38,39].

Characterization of bio-oil focuses on bulk property measurements such as pH, water and ash content, viscosity, and elemental composition [40,41]. FTIR, NMR, and GC–MS are also commonly used analytical methods to provide molecular details of bio-oils [42,43]. However, FTIR and NMR average functional group information in the mixture while GC–MS can only characterize individual molecules after GC separation that is limited to volatile components. The highly energetic conversion process generates numerous compounds, particularly nonvolatile molecules, not present in the database or commercially available, which makes identification difficult. HRMS coupled with appropriate ionization methods has been adapted to thoroughly characterize hundreds of compounds that are not observed in traditional analytical techniques

[44-46]. For example, this approach enabled direct chemical composition analysis of over 800 species in red oak bio-oil using negative electrospray ionization (ESI) FTICR MS [46].

Catalytic Conversion of Pyrolysis Vapors

Bio-oil is plagued by several issues that prevent its use as a supplement to petroleum-based products. In its crude state, bio-oil is incompatible with conventional fuels due to high oxygen and solids content, high viscosity, and instability [38,39]. Thus, production of transport fuels such as diesel or gasoline requires full deoxygenation and further refining. Several methods for physically, chemically, and/or catalytically upgrading bio-oils have been proposed in recent decades [20]. Physical upgrading that improves undesirable bio-oil properties includes filtration, solvent addition, or emulsions [47-49]. However, the drawback of these methods is increased fuel production cost due to high energy, solvent, and surfactant needs.

Catalytically upgrading bio-oil could offer a better way to improve biofuel characteristics. Either complete or partial catalysis refines bio-oil to a product that is more compatible with conventional refinery streams, which could potentially reduce production cost and enable biofuel to better compete with traditional fuels. Current methods include hydrotreatment, catalytic vapor cracking, esterification, and gasification to syngas followed by hydrocarbon or alcohol synthesis [20]. Hydrotreating and catalytic cracking of bio-oils have been rigorously investigated as potential processes for refinement [50-54]. Hydrotreating removes oxygen as water via catalytic reactions with H_2 and metal catalysts, e.g. sulfided CoMo [51,52]. Currently, it has been deemed economically unsustainable due to the substantial H_2 necessary, high cost from maintaining high-pressure vessels and metal catalysts, and catalyst deactivation via coking [20,55].

Catalytic cracking using zeolite catalysts deoxygenates bio-oil by removing CO_2 [38,56]. Key advantages over hydrotreatment include absence of H_2, operation at atmospheric pressure, and cheap aluminosilicate zeolite catalysts. Zeolite cracking is also plagued by catalyst deactivation by coking, although the zeolites could be regenerated by oxidation of the coke [57]. Unfortunately, technical and economic modeling purports processing costs as too high, rendering the products not competitive with traditional fossil fuels [58]. However, only bench-scale level research has been performed and further development is necessary for success. Efficient screening and evaluation of new catalysts is critical before expanding to an industrial scale in order to reduce cost and time.

Biomass Pyrolysis Kinetics

Upgrading and refining bio-oil are pieces of a much larger picture when generating a product capable of competing with petroleum-based products. Understanding the underlying kinetics and mechanisms involved in biomass pyrolysis could have significant consequences in controlling the quality of the final products and the economics of the process. Thus, scientists have been investigating kinetic parameters of biomass pyrolysis for many years but with conflicting results [20,37,56].

Experiments performed to measure kinetic information generally utilize thermogravimetric analysis (TGA) and μPy-GC–MS [56,59,60]. However, TGA methods cannot provide heating rates that occur during fast pyrolysis conversion (typically 1-150 °C min^{-1} versus > 1000 °C min^{-1}) [61,62]. Due to the low temperature ramps employed in TGA experiments, the decomposition of individual biopolymers (hemicellulose, cellulose, and lignin) occurs in distinct temperature zones [63]. Thermal decomposition of biopolymers during extreme heating rates

involved in fast pyrolysis processes is far more ambiguous. The shortcomings of TGA prevent molecular-level information and result in lumped, condition-specific kinetic models for specific biopolymers. For example, the Broido–Shafizadeh mechanism was developed utilizing TGA to measure experimental rate constants, which could also accurately predict mass volatilization rates for cellulose [64,65]. This simplistic kinetic model ignores the complex, molecular-level chemistry and instead groups reactants, intermediates, and products by phase, i.e., vapor, gas, and char.

Several studies have been performed to address the need for detailed descriptions of molecular-level processes occurring in biomass pyrolysis. One small breakthrough occurred in 2009 by Dauenhauer and co-workers, who employed a novel analysis technique utilizing high-speed photography to capture images of cellulose pyrolysis [66,67]. They confirmed the presence of a liquid intermediate termed molten biomass, which has been suggested to be "active cellulose" (a proposed intermediate step during pyrolysis that initiates two competing pathways to either volatiles or char/gas) [68]. A more recent study from Dauenhauer and co-workers demonstrated the development of thin-film cellulose pyrolysis experiments [56,69]. Thin-films eliminated conduction effects caused by large particles during the pyrolysis process and enabled isothermal, kinetically limited data for use in developing molecular-level kinetic models.

Broadbelt et al. presented experimental data and mechanistic modeling to investigate the reaction mechanism of cellulose and other glucose-based carbohydrates [70,71]. In a two part publication, they developed a full map for mechanistic decomposition of cellulose and then used experimental data to validate and evaluate their model. A particular strength of their model is its wide applicability to predict experimental yields of various pyrolysis products at different pyrolysis temperatures.

The shortcomings of these recent studies should be noted. First, μPy-GC–MS and flame ionization detector (FID) were used to identify and quantify pyrolysis products, respectively. Four fundamental flaws of the instrumentation include: (1) the loss of kinetic data due to GC separation, which is generated afterwards by combining experimental product yields and computer modeling, (2) loss of short-lived intermediate species that would provide valuable information for more elaborate mechanistic models, (3) possibly incorrect experimental results and kinetics arising from mass transport effects caused when pyrolysis vapors escaping from the bottom of the crucibles become partially "trapped" in the turbulent He stream and consequently increasing vapor residence times, and (4) lack of identification and understanding of unique pyrolysis products not in the NIST database. Second, the load weight of pyrolyzed material in the Broadbelt study ranged from 200-500 μg, which is likely kinetically and conduction limited. Hence, molecular-level kinetics of individual species will not be "pure" in the sense that Arrhenius parameters were determined using quantum chemical calculations and fitted to experimental product yields, which might not accurately represent the kinetics of individual chemical species.

Initial research of fundamental cellulose pyrolysis kinetics reveals the daunting and complex nature of the task. Thorough understanding of molecular kinetics for biomass pyrolysis remains a barrier to reactor optimization and consequently commercial adoption. Surmounting the severe limitations previously described requires new instrumentation and techniques that can more accurately probe an individual molecule's fate.

Dissertation Organization

This dissertation is organized into six chapters. The first chapter (above) serves as a broad introduction to provide context for our efforts of applying high-resolution mass spectrometry to the analysis and characterization of biomass pyrolysis products and kinetics. Chapters two through four are reproductions of peer-reviewed publications. The second chapter utilizes HRMS for molecular-level characterization of molecules extracted from biochars produced from pyrolysis and gasification. Chapter three expands the application of HRMS to study nitrogen-containing species in fast pyrolysis bio-oils of switchgrass harvested at various times. Chapter four presents a novel application of dopant-assisted atmospheric pressure chemical ionization (dAPCI) GC–MS for *in situ* catalytic fast pyrolysis (CFP) product analysis. A high-resolution time-of-flight mass spectrometer (TOF MS) directly determined chemical compositions of CFP products that enabled efficient comparison and evaluation of catalytic deoxygenation. The fifth chapter presents novel application of micropyrolysis and HRMS for real-time monitoring of fast pyrolysis products from thin-films of glucose-based carbohydrates and cellulose. The sixth and final chapter discusses general conclusions and provides future directions and applications of the developed HRMS techniques.

References

[1] Maux, D.; Enjalbal, C.; Martinez, J.; Aubagnac, J.-L.; Combarieu, R. *J. Am. Soc. Mass Spectrom*. **2001**, 12, 1099−1105.

[2] Spengler, B. *Anal. Chem.* **2015**, 87, 64−82.

[3] Yost, R.A.; Enke, C.G. *Anal. Chem.* **1979**, 51, 1251A−1262A.

[4] Hughey, C.A.; Rodgers, R.P.; Marshall, A.G. *Anal. Chem*. **2002**, 74, 4145−4149.

[5] Farag, M.A.; Porzel, A.; Mahrous, E.A.; El-Massry, M.M.; Wessjohann, L.A. *Anal. Bioanal. Chem.* **2015**, 407, 1937−1949.

[6] Angeletti, R.; Gioacchini, A.M.; Seraglia, R.; Piro, R.; Traldi, P. *J. Mass Spectrom.* **1998**, 33, 525−531.

[7] De Hoffmann, E.; Stroobant, V. *Mass Spectrometry - Principles and Applications*; 2nd ed.; John Wiley & Sons: Chichester, **2001**.

[8] Aston, F.; Fowler, R.H. *Philos. Mag. Ser.* **1922**, 43, 255.

[9] Squires, G. *J. Chem Soc, Dalton Trans.* **1998**, 3893−3900.

[10] Settle, F.A. *Anal. Chem.* **2002**, 74, 36A−43A.

[11] Watson, J.T.; Biemann, K. *Anal. Chem.* **1965**, 37, 844−851.

[12] Berry, C.E.; Rock, S.M. *J. Chem. Phys.* **1951**, 19, 1208−1209.

[13] VanLear, G.E; McLafferty, F.W. Annu. Rev. Biochem. **1969**, 289−322.

[14] Tatematsu, A., Goto, T. *J. Pharm. Soc. Japan* **1965**, 85, 624

[15] Carlson, E.G.; Paulissen, G.T.; Hunt, R.H.; O'Neal, M.J. *Anal. Chem.* **1960**, 21, 1489−1498.

[16] Marshall, A.G. *Int. J. Mass Spectrom.* **2000**, 200, 331–356.

[17] Marshall, A.G.; Rodgers, R.P. *Acc. Chem. Res.* **2004**, 37, 53–59.

[18] Oliver, S.G.; Winson, M.K.; Kell, D.B.; Baganz, F. *Trends Biotechnol.* **1998**, 16, 373–378.

[19] Sohi, S.P.; Krull, E.; Lopez-Capel, E.; Bol, R. *Adv. Agron.* **2010**, 105, 47–82.

[20] Bridgwater, A.V. *Biomass Bioenergy* **2012**, 38, 68–94.

[21] Laird, D.A.; Fleming, P.; Davis, D.D.; Horton, R.; Wang, B.; Karlen, D.L. *Geoderma* **2010**, 158, 443– 449.

[22] Laird, D.A. *Agron. J.* **2008**, 100, 178–181.

[23] Steinbeiss, S.; Gleixner, G.; Antonietti, M. *Soil Biol. Biochem.* **2009**, 41, 1301–1310.

[24] Rogovska, N.; Laird, D.; Cruse, R.; Fleming, P.; Parkin, T.; Meek, D. *Soil Sci. Soc. Am. J.* **2011**, 75, 871–879.

[25] Yu, X.-Y.; Ying, G.-G.; Kookana, R.S. *Chemosphere* **2009**, 76, 665–671.

[26] Yang, Y.; Sheng, G.; Huang, M. *Sci. Total Environ.* **2006**, 354, 170–178.

[27] Wen, B.; Li, R.-J.; Zhang, S.; Shan, X.-Q.; Fang, J.; Xiao, K.; Khan, S. U. *Environ. Pollut.* **2009**, 157, 968–974.

[28] Özçimen, D.; Ersoy-Meriçboyu, A. *Renewable Energy* **2010**, 35, 1319–1324.

[29] Brewer, C.E.; Schmidt-Rohr, K.; Satrio, J.A.; Brown, R.C. *Environ. Prog. Sustainable Energy* **2009**, 28, 386–396.

[30] Brewer, C.E.; Unger, R.; Schmidt-Rohr, K.; Brown, R.C. *Bioenergy Res.* **2011**, 4, 312–323.

[31] Lee, J.W.; Kidder, M.; Evans, B.R.; Paik, S.; Buchanan, A.C., III; Garten, C.T.; Brown, R.C. *Environ. Sci. Technol.* **2010**, 44, 7970–7974.

[32] Spokas, K.A.; Novak, J.M.; Stewart, C.E.; Cantrell, K.B.; Uchimiya, M.; DuSaire, M.G.; Ro, K.S. *Chemosphere* **2011**, 85, 869–882.

[33] Podgorski, D.C.; Hamdan, R.; McKenna, A.M.; Nyadong, L.; Rodgers, R.P.; Marshall, A.G.; Cooper, W.T. *Anal. Chem.* **2012**, 84, 1281–1287.

[34] Hockaday, W.C.; Grannas, A.M.; Kim, S.; Hatcher, P.G. *Org. Geochem.* **2006**, 37, 501–510.

[35] Warnock, D.; Lehmann, J.; Kuyper, T.; Rillig, M. *Plant Soil* **2007**, 300, 9–20.

[36] Czernik, S.; Bridgwater, A.V. *Energy Fuels* **2004**, 18, 590–598.

[37] Mohan, D.; Pittman, C.U.; Steele, P.H. *Energy Fuels* **2006**, 20, 848–889.

[38] DOE, *Conversion Technologies for Advanced Biofuels: Preliminary Roadmap & Workshop Report*, Arlington, VA: **2011**.

[39] Talmadge, M.S.; Baldwin, R.M.; Biddy, M.J.; McCormick, R.L.; Beckham, G.T.; Ferguson, G.A.; Czernik, S.; Magrini-Bair, K.A.; Foust, T.D.; Metelski, P.D.; Hetrick, C.; Nimlos, M.R. *Green Chem.* **2014**, 16, 407–453.

[40] Wilson, D.M.; Dalluge, D.L.; Rover, M.; Heaton, E.A.; Brown, R.C. *Bioenergy Res.* **2013**, 6, 103–113.

[41] Peacocke, G.V.C.; Russel, P.A.; Jenkins, J.D.; Bridgwater, A.V. *Biomass Bioenergy* **1994**, 7, 169–178.

[42] Nayan, N.K.; Kumar, S.; Sing, R.K. *Bioresour. Technol.* **2012**, 124, 186–189.

[43] Pan, S.; Pu, Y.; Foston, M.; Ragauskas, A.J. *Bioenerg. Res.* **2013**, 6, 24–34.

[44] Marshall, A.G.; Rodgers, R.P. *Acc. Chem. Res.* **2004**, 37, 53–59.

[45] Smith, E.A.; Lee, Y.J. *Energy Fuels* **2010**, 24, 5190–5198.

[46] Smith, E.A.; Park, S.; Klein, A.T.; Lee, Y.J. *Energy Fuels* **2012**, 26, 3796–3802.

[47] Diebold, J.P.; Czernik, S.; Scahill, J.W.; Philips, S.D.; Feik, C.J. In *Biomass Pyrolysis Oil Properties and Combustion Meeting*, Milne, T.A. (ed.), Boulder, CO: **1994**, 90–108.

[48] Diebold, J.P.; Czernik, S. *Energy Fuels* **1997**, 11, 1081–1091.

[49] Ikura, M.; Slamak, M.; Sawatzky, H. 'Pyrolysis liquid-in-diesel oil microemulsions'. U.S. Patent 5,820,640: **1998**.

[50] Bridgwater, A.V. *Catal. Today* **1966**, 29, 285–295.

[51] Elliott, D.C.; Baker, E. In *Energy from Biomass and Wastes X*, Klass, D. (ed.), I.G.T.: **1983**, 765–782.

[52] Blin, J.; Volle, G.; Girard, P.; Bridgwater, A.V.; Meier, D. *Fuel* **2007**, 86, 2679–2686.

[53] Williams, P.T.; Nugranad, N. *Energy* **2000**, 25, 493–513.

[54] Carlson, T.R.; Vispute, T.P.; Huber, G.W. *Chem. Sus. Chem.* **2008**, 1, 397–400.

[55] Cottam, M.-L.; Bridgwater, A.V. *Biomass Bioenergy* **1994**, 7, 267–273.

[56] Mettler, M.S.; Paulsen, A.D.; Vlachos, D.G.; Dauenhauer, P.J. *Energy Environ. Sci.* **2012**, 5, 7864–7898.

[57] Ibanez, M.; Valle, B.; Bilbao, J.; Gayubo, A.G.; Castano, P. *Catal. Today* **2012**, 195, 106–113.

[58] Bridgwater, A.V.; Cottam, M.-L. *Energy Fuel* **1992**, 6, 113–120.

[59] White, J.E.; Catallo, W.J.; Legendre, B.L. *J. Anal. Appl. Pyrolysis* **2011**, 91, 1–33.

[60] Bahng, M.-K.; Mukarakate, C.D.; Robichaud, J.; Nimlos, M. R. *Anal. Chim. Acta* **2009**, 651, 117–138.

[61] Mettler, M.S.; Mushrif, S.H.; Paulsen, A.D.; Javadekar, A.D.; Vlachos, D.G.; Dauenhauer, P.J. *Energy Environ. Sci.* **2012**, 5, 5414–5424.

[62] Lin, Y.C.; Cho, J.; Tompsett, G.A.; Westmoreland, P.R.; Huber, G.W. *J. Phys. Chem. C* **2009**, 113, 20097–20107.

[63] Yang, H.; Yan, R.; Chen, H.; Lee, D.H.; Zheng, C. *Fuel* **2007**, 86, 1781–1788.

[64] Bradbury, A.G.W.; Sakai, Y.; Shafizadeh, F. *J. Appl. Polym. Sci.* **1979**, 23, 3271–3280.

[65] Broido, A.; Nelson, M.A. *Combust. Flame* **1975**, 24, 263–268.

[66] Dauenhauer, P.J.; Colby, J.L.; Balonek, C.M.; Suszynski, W.J.; Schmidt, L.D. *Green Chem.* **2009**, 11, 1555–1561.

[67] Teixeira, A.R.; Mooney, K.G.; Kruger, J.S.; Williams, C.L.; Suszynski, W.J.; Schmidt, L.D.; Schmidt, D.P.; Dauenhauer, P.J. *Energy Environ. Sci.* **2011**, 4, 4306–4321.

[68] Lédé, J. *J. Anal. Appl. Pyrolysis* **2012**, 94, 17–32.

[69] Paulsen, A.D.; Mettler, M.S.; Dauenhauer, P.J. *Energy Fuels* **2013**, 27, 2126–2134.

[70] Zhou, X.; Nolte, M.W.; Mayes, H.B.; Shanks, B.H.; Broadbelt, L.J. *Ind. Eng. Chem. Res.* **2014**, 53, 13274–13289.

[71] Zhou, X.; Nolte, M.W.; Shanks, B.H.; Broadbelt, L.J. *Ind. Eng. Chem. Res.* **2014**, 53, 13290–13301.

CHAPTER II

HIGH-RESOLUTION MASS SPECTROMETRIC CHARACTERIZATION OF MOLECULES ON BIOCHAR FROM PYROLYSIS AND GASIFICATION OF SWITCHGRASS

A paper published in *Energy and Fuels*

Energy Fuels **2012**, 26, 3803–3809.

D. Paul Cole, Erica A. Smith, and Young Jin Lee

Abstract

Organic molecules entrapped in biochar during pyrolysis and gasification of switchgrass have been studied using high-resolution mass spectrometry. Two solvent systems, toluene and a mixture of water/methanol, were used to extract hydrophobic aromatic compounds and hydrophilic polar compounds, respectively. Laser desorption ionization and atmospheric pressure photoionization were used for toluene extracts, while electrospray ionization was used for water/methanol extracts, followed by orbitrap mass spectrometric data acquisition. Molecular compounds previously known in bio-oils were observed for fast pyrolysis biochar, with phenolic and carbohydrate-derived compounds originating from the pyrolysis of lignin and holocellulose, respectively. In contrast, polycyclic aromatic hydrocarbons (PAHs) with various ring sizes were observed for gasification biochar and also for slow pyrolysis biochar in low abundance.

Introduction

Once thought to be a low-value waste byproduct of biomass pyrolysis, biochar has shown promise as a soil amendment and a carbon sequestration agent [1-4]. Biochar application can improve soil quality through increased moisture and nutrient retention, increased microbial

activity, and decreased bioavailability of organic contaminants [5-7]. Biochar is produced from various feedstocks (including cornstover, wood, and even municipal waste) via various thermochemical conversion processes, such as pyrolysis and gasification [8-9]. Pyrolysis involves heating of organic matter in the absence of oxygen to maximize either bio-oil, as in fast pyrolysis, or biochar, as in slow pyrolysis. The difference between fast and slow pyrolysis involves the heating rate and heating temperature: fast pyrolysis occurs at 400−600 °C with less than 2 s of heating time, and slow pyrolysis occurs at 300−800 °C for at least 1 h. Alternatively, gasification systems rapidly heat biomass in the presence of oxygen to produce syngas (CO and H_2). Gasification generally produces the least amount of biochar (~10% of biomass weight converted to solid char), followed closely by fast pyrolysis (~12%), and surpassed by slow pyrolysis (~35%) [9]. Brown and co-workers have characterized biochars from various thermochemical conversion processes and various feedstocks [10,11]. Fourier transform infrared (FTIR) spectra showed functional groups unique to the thermochemical conversion method. Oxygen-containing functional groups, specifically hydroxyl stretch at 3400 cm^{-1} and carboxylic carbon stretch at 1700 cm^{-1}, were dominant in fast pyrolysis spectra, weak in slow pyrolysis, and almost absent in gasification. Additionally, ^{13}C direct polarization nuclear magnetic resonance (NMR) spectra showed highly abundant oxygen-containing carbons in fast pyrolysis biochar compared to slow pyrolysis or gasification. Aromatic carbons dominated the NMR spectra for all biochars. The aromatic C−H was most abundant for slow pyrolysis (~30%), slightly lower for fast pyrolysis (~23%), and lowest for gasification (~10%). Similar results were obtained by Lee and co-workers in their FTIR analysis of fast pyrolysis and gasification chars from corn stover [12]. FTIR and NMR techniques provide valuable information about chemical bonds and functional groups; however, they cannot separate the information from each individual molecule

and only provide the average information of the whole mixture. Volatile organic compounds (VOCs) within biochar were studied by Spokas and co-workers using gas chromatography−mass spectrometry (GC−MS) analysis with headspace desorption at 150 °C for 10 min [13]. Over 140 unique compounds were identified but limited to volatile gases with molecular weights mostly below 100. A comprehensive understanding of all organic molecules would be very important for soil application of biochar because they might be released to the soil and affect soil microbial systems [7,14]. Ultrahigh-resolution mass spectrometry, such as Fourier transform ion cyclotron resonance mass spectrometry (FT-ICR MS), is a major tool for petroleomics, allowing for direct chemical composition analysis of complex crude oils, and was successfully applied to characterize tens of thousands of compounds in petroleum crude oils [15-17]. Podgorski and co-workers adapted desorption atmospheric pressure photoionization (DAPPI) for direct molecular characterization of intact biochar materials using FT-ICR [18]. DAPPI−FT-ICR analysis on combusted char showed a bimodal distribution of aromatic (low H/C and O/C ratios) and aliphatic (high H/C and O/C ratios) compounds originating from lignin and holocellulose, respectively. Pyrolyzed oak biomass displayed increased aromaticity and lacked the aliphatic distribution. FT-ICR MS was also used in a study by Hockaday and co-workers that examined dissolved organic matter from naturally degraded charcoal particles over a period of 100 years [19].

A petroleomic approach was first adapted by our group for the analysis of bio-oils [20]. Using laser desorption ionization (LDI) as an ionization method, we have analyzed over 100 nonvolatile lignin pyrolysis products in bio-oils. Recently, we have further expanded this approach using negative electrospray ionization [(−) ESI] and could characterize over 800 chemical compositions [21]. (−) ESI could analyze most volatile compounds with *m/z* >100,

including pyrolysis products of not only lignin but also cellulose and hemicellulose. In the current study, we adapt this high-resolution mass spectrometry approach to characterize molecular components in the biochar produced by three different thermochemical processes.

Experimental Section

Materials

Switchgrass biochar samples were obtained from Robert Brown at Iowa State University. The fast pyrolysis biochar was produced on a fluidized-bed reactor at 450 °C [10]. Gasification char was produced on a bubbling fluidized-bed reactor at 824 °C under steam/ oxygen-blown conditions. Slow pyrolysis biochar was generated in a paint can heated at a rate of 15 °C min^{-1} up to 500 °C and held for 30 min. The three biochars are the same material as biochars 7, 10, and 13 in the report by Brown's group, corresponding to fast pyrolysis, gasification, and slow pyrolysis chars, respectively [11]. Elemental analysis of fast pyrolysis switchgrass biochar showed carbon, hydrogen, nitrogen, and oxygen percent contents at 37.5, 2.2, 0.5, and 8.9, respectively; 25.4, 0.4, 0.3, and 4.5 for gasification, respectively; 39.4, 1.3, 0.7, and 5.6 for slow pyrolysis, respectively.[11] Water and methanol were purchased at the highest available purity from Fisher Scientific (Fair Lawn, NJ). High-performance liquid chromatography (HPLC)-grade toluene (≥99.9%) was purchased from Sigma-Aldrich (St. Louis, MO).

Mass spectrometry

A linear ion trap-orbitrap mass spectrometer (LTQ-Orbitrap Discovery, Thermo Scientific, San Jose, CA) was used for the current study. For the LDI−MS study, the instrument was configured with a matrix-assisted laser desorption ionization (MALDI) system operating at

intermediate vacuum pressure (75−80 mTorr). A nitrogen laser (MNL 100, Lasertechnik Berlin, Berlin, Germany) was used to vaporize and ionize samples spotted on a MALDI plate. MALDI plates were deep-cleaned prior to analysis according to the instruction manual. A total of 5 mL of toluene was added to 50 mg of biochar samples and sonicated for 10 min. A 1 mL aliquot of the liquid fraction was centrifuged to separate unsettled char, and 500 μL of the supernatant was taken for the analysis. Extraction efficiency using toluene was ∼5 mg g^{-1} for fast pyrolysis and gasification chars and <0.5 mg g^{-1} for slow pyrolysis char. The extracts were spotted in three increments of 0.5 μL on the MALDI plate, allowing each drop to airdry between spotting. The laser power was carefully adjusted, and 15−35 μJ per pulse of laser power was used with two neutral density filters, reducing the actual laser power to 25%. A tandem mass spectrometry (MS/MS) study was performed for a few major compounds in the linear ion trap of the mass spectrometer at a collision energy of 35% and with an isolation width of 1.8 Da.

For ESI and atmospheric pressure photoionization (APPI), the MALDI source was removed from the mass spectrometer and the atmospheric pressure ionization chamber was reconfigured. A vacuum ultraviolet (UV) lamp (PhotoMate, 10.0/10.2 eV, Syagen, Tustin, CA) was used for APPI−MS analysis of toluene extracts with IonMax source (Thermo) and API probe. The API probe vaporization temperature ranged from 380 to 400 °C with the MS inlet capillary held at 275 °C and the tube lens voltage set at 70 V. A 50:50 mixture of water and methanol (v/v) was used to extract polar compounds entrapped in biochar with a similar sampling process as toluene extraction. Extraction efficiency using the water/methanol solvent system is ∼48 mg g^{-1} for fast pyrolysis char, ∼19 mg g^{-1} for gasification char, and 0.2 mg g^{-1} for slow pyrolysis char. ESI in negative-ion mode was used for the water/methanol extracts. All of the experiments were performed in three replicates.

Data analysis

Composer (Sierra Analytics, Modesto, CA) was used for spectra calibration, chemical composition assignment, and molecular visualization of the data sets acquired from the extracts of fast pyrolysis chars. The data obtained from the orbitrap was exported in a text file using QualBrowser (Thermo Scientific) for the peaks above 0.5% relative abundance; they are all above 6 times the baseline noise. The orbitrap was calibrated externally according to the procedure provided by the manufacturer, and its mass accuracy is confirmed with previously characterized bio-oil samples obtained at the same condition: <3 ppm for (+) LDI and <5 ppm for (−) ESI. Mass errors in positive-ion mode are consistent within the same spectrum, further confirming its reliability in mass measurement; e.g., all major peaks in Figure 1 have a mass error from −1 to −3 ppm. Mass calibration in negative-ion mode had more errors (up to 5 ppm); nonetheless, most peaks show at low mass (<*m/z* 200), where misassignment of the chemical composition is not likely. Peak assignment was further confirmed through the Kendrick mass chart. The chemical composition analysis was performed with Composer for extracted compounds, and the chemical compositions were limited to 30 carbons, 60 hydrogens, 15 oxygens, and 5 nitrogens, with a mass accuracy tolerance of 5 ppm. No ^{34}S isotope was observed, and sulfur was not included as a possible element.

Results and Discussion

Overall strategy

We first attempted direct LDI−MS analysis of biochars by attaching the biochar particles to the MALDI plate using double-sided tape (Supplemental Figure 1). This approach generated large distributions of fullerene-like compounds produced in the high-energy, high-density laser

plume, which is consistent with the initial discovery of fullerenes by laser vaporization of graphite [22]. Hence, the subsequent studies focused on the solvent extracts of biochar to separate and enrich the small molecules from solid char materials. We used two different solvent systems, toluene and a mixture of water and methanol. Toluene was chosen to extract lignin-derived aromatic compounds that might have been adsorbed on the surface of polyaromatic biochar. Water/ methanol was chosen to extract hydrophilic polar compounds, particularly originating from cellulose or hemicellulose. Toluene extracts were investigated by LDI and APPI, because of their efficient ionization of aromatic compounds. ESI was used for water/methanol extracts because of its efficient ionization of polar compounds. A LTQ-Orbitrap high-resolution mass spectrometer was used for accurate mass measurement and direct determination of their chemical compositions. The lower version of orbitrap used in the current study (Orbitrap Discovery) has limited mass resolving power ($m/\Delta m \sim 30{,}000$ at *m/z* 400) compared to FT-ICR MS or a higher version of orbitrap. However, the biochar extract is much less complex than bio-oils or petroleum oils, with little or no overlapping peaks, and its mass resolving power was sufficient for the current study. For example, the complexity of biochar extract in the current study is less than that of our previous LDI-Orbitrap analysis of bio-oils, which is confirmed to have sufficient mass resolution in comparison to FT-ICR [20].

Toluene extracts of biochar

LDI experiments on toluene extracts of biochar were performed in a similar fashion to the recent LDI−MS analysis of bio-oils [20]. Careful attention was made to avoid any possible aggregation reactions in the laser plume. Specifically, the spotted sample concentration and laser power were minimized to the lowest possible value. Unlike direct biochar analysis, extracts

spotted in low concentration do not produce high-density laser plume and accompanying aggregation reactions. Figure 1 compares LDI−MS spectra of toluene extracts from three biochars produced from fast pyrolysis, slow pyrolysis, and gasification. Marked differences can be found among the three spectra: mostly O4 and O5 compounds in fast pyrolysis (Figure 1A), polycyclic aromatic hydrocarbons (PAHs) in gasification (Figure 1B), and lack of peaks except for a few PAHs in slow pyrolysis (Figure 1C).

The MS spectrum of toluene extracts of fast pyrolysis biochar (Figure 1A) is very similar to that of the fast pyrolysis bio-oils previously reported (Figure 2A in ref 20), specifically the major compounds of *m*/*z* 270 ($C_{16}H_{14}O_4$), 284 ($C_{17}H_{16}O_4$), 298 ($C_{18}H_{18}O_4$), 328 ($C_{19}H_{20}O_5$), and 342 ($C_{20}H_{22}O_5$). The MS/MS spectra of a few major compounds are consistent with those of bio-oil compounds, further confirming their structural similarity (Supplemental Figure 2) [20]. It is not surprising to find bio-oil-like components in fast pyrolysis biochar. The fast pyrolysis biochar is a side product of bio-oil production in the fast pyrolysis process. Specifically, the pyrolysis reactor used in the current study is designed to filter out char materials by having pyrolysis vapors pass through the Cyclone [23]. Some bio-oil vapors might not have escaped from the char particles and left behind as condensate.

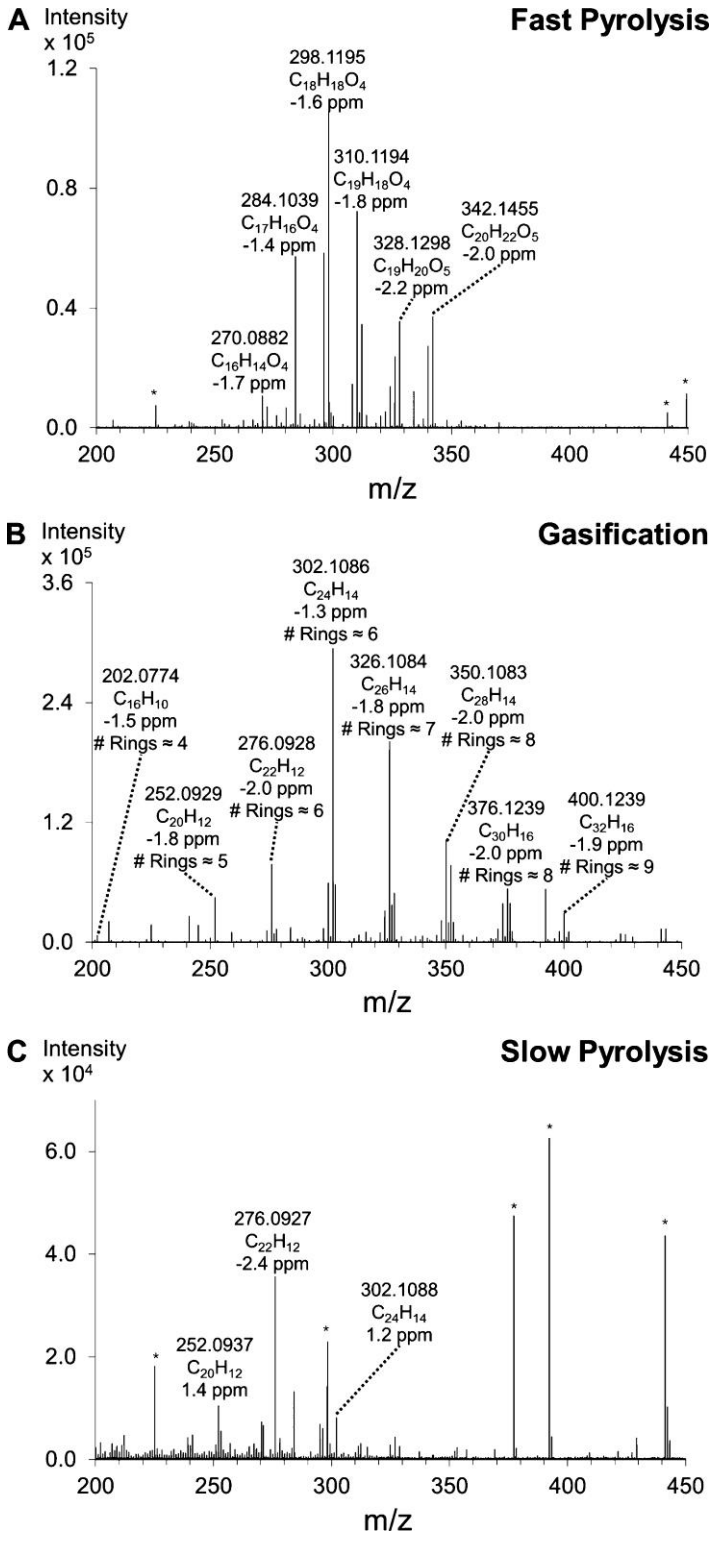

Figure 1. (+) LDI–MS spectra for toluene extracts of biochar from **(A)** fast pyrolysis, **(B)** gasification, and **(C)** slow pyrolysis. The number of rings is estimated for the polycyclic aromatic hydrocarbons in Figure 1B. (*) Contamination.

There are a few differences between the MS spectrum for biochar extracts and previous bio-oil data. The previous LDI–MS spectrum of bio-oils was composed of two distinguished groups of peaks: lignin dimers at *m*/*z* 250–400 and lignin trimers at *m*/*z* 400–550 [20]. Lignin trimer compounds are roughly about ~15% of dimers in the previous bio-oil spectrum, but they are present in very low abundance in biochar extracts with roughly 1% (Figure 1A). One possible explanation is that the lignin dimers and trimers are mostly produced from secondary reactions between monomers. If we assume the pyrolyzates are mostly monomeric initially and oligomerized through reaction with each other, the oligomerization reaction would be much less favored in biochar-entrapped molecules because of the competition with absorption to the char surface. Dimerization may still happen, but the reaction probability for trimerization would be very low.

Another major difference between bio-oil and biochar extract is the fact that the most abundant peak in the previous bio-oil spectrum, *m*/*z* 272 ($C_{16}H_{16}O_4$), is very low in Figure 1A (~7% of the base peak). We attribute this to the difference between the biomass materials: loblolly pine (previous study) versus switchgrass (current study). We have previously noted the structural uniqueness of *m*/*z* 272 in its MS/MS spectrum compared to others. This ion at *m*/*z* 272 has been found in pyrolysis–field ionization and pyrolysis–molecular beam mass spectrometric studies by several research groups, particularly for hardwood biomass materials [24-28]. Its abundance might be related to the biomass materials, presumably hardwood. A further study is needed to understand the structural nature of this particular compound.

LDI–MS spectra of toluene extracts of biochar materials produced from gasification and slow pyrolysis (panels B and C of Figure 1) give some insights about the associated thermochemical processes. First of all, unlike fast pyrolysis, oxygen compounds do not exist in

both spectra, suggesting that the feed of oxygen fuels in gasification or long reaction time in slow pyrolysis could successfully remove most of the oxygen compounds in biomass materials and convert them into CO or CO_2. Previous NMR and FTIR studies suggest that there still are some oxygen-containing functional groups on these biochars, but they must be from solid biochar materials and not from small molecules adsorbed on the surface [10]. Toluene extracts of gasification biochar (Figure 1B) are all PAHs with various ring sizes. It is consistent with a molecular beam mass spectrometry study on the syngas derived from gasification of corn stover [28]. They found up to five-ring PAHs, with one or two aromatic ring compounds most abundant (cf. toluene, phenol, styrene, and naphthalene). Very large PAHs with the number of rings of 6–8 are most dominant in our study, and small ring compounds are absent. This is mostly because LDI–MS analysis was performed in intermediate vacuum (~75 mTorr) and volatile molecular compounds are all vaporized before the analysis. The removal of these compounds is important in the gasification process, and their detection adsorbed on the biochar might indicate their efficient removal in the current thermochemical process. Slow pyrolysis shown in Figure 1C, on the other hand, has almost no peaks other than a few PAHs, suggesting that complete reactions occur in the slow pyrolysis process.

Photoionization at atmospheric pressure, APPI, was also used for the analysis of three biochar extracts. APPI allows for the direct analysis of liquid samples with photoionization using vacuum UV photons (10/10.2 eV). One critical limitation in APPI of the biochar extracts is that the spectra are dominated by contaminations from various sources. APPI is subject to contamination in general because it has the ability to ionize most organic compounds, but it was especially significant in biochar extracts because of plasticizers accrued in the extraction procedure, despite the use of Nalgene tubes to minimize contamination. Despite the significant

contaminations, we could confirm the existence of major compounds in panels A and B of Figure 1, ensuring LDI–MS results (see Supplemental Figure 3).

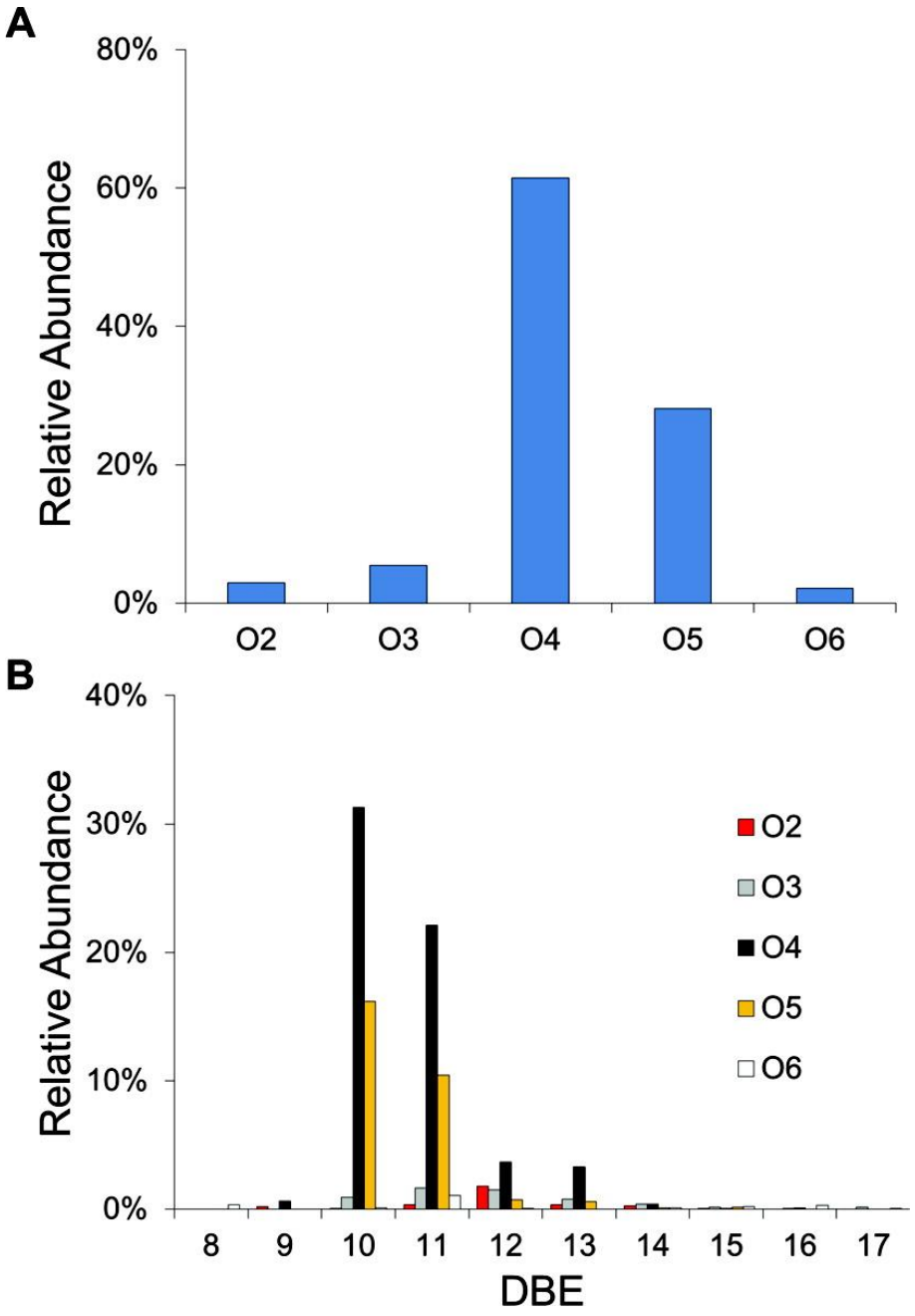

Figure 2. Chemical composition analysis of the (+) LDI–MS spectrum of toluene extracts of fast pyrolysis char shown in Figure 1A: **(A)** heteroatom class distribution and **(B)** DBE distribution for each heteroatom class.

Chemical composition analysis was performed for the LDI–MS spectrum of toluene extracts of fast pyrolysis biochar (Figure 1A) and reliably identified 32 chemical compositions. Heteroatom class distribution shown in Figure 2A is very similar to that of bio-oils (cf. Figure 4A in 20), except for much less abundant O6 compounds, which is attributed to the lack of lignin trimers in biochar extracts. In bio-oils, O6 compounds represent most of the lignin trimers (DBE of 14–17), while the lignin trimer compounds are almost negligible in the DBE distribution of biochar extracts shown in Figure 2B.

Water/Methanol extracts of biochar

To study polar compounds in biochar, a 50:50 mixture of water and methanol was used as an extraction solvent and the extracts were subjected to high-resolution mass spectrometry using ESI. Mass spectral acquisition in positive-ion mode suffered from contaminations, particularly from K and Na metal ions present in high abundance in switchgrass, which significantly suppressed ion signals. Therefore, we focused on negative-ion mode, where alkaline metal ions and plasticizers are all suppressed. We could not obtain meaningful mass spectra for biochar extracts from slow pyrolysis and gasification, suggesting that there are almost no polar compounds adsorbed on biochars (for slow pyrolysis) or inefficient deprotonation because of high Na/K contents (for gasification). For fast pyrolysis biochar, however, we could obtain a nice clean spectrum, as shown in Figure 3. The spectrum is dominated by low-molecular-weight components in the *m*/*z* range of 100–200 and mostly composed of O2–O5 compounds, which is similar to our recent study on fast pyrolysis bio-oils in (−) ESI [21]. Some of the major compounds are also present in the previous study, such as *m*/*z* 131 and 181, but some are different, such as *m*/*z* 117, 137, and 151.

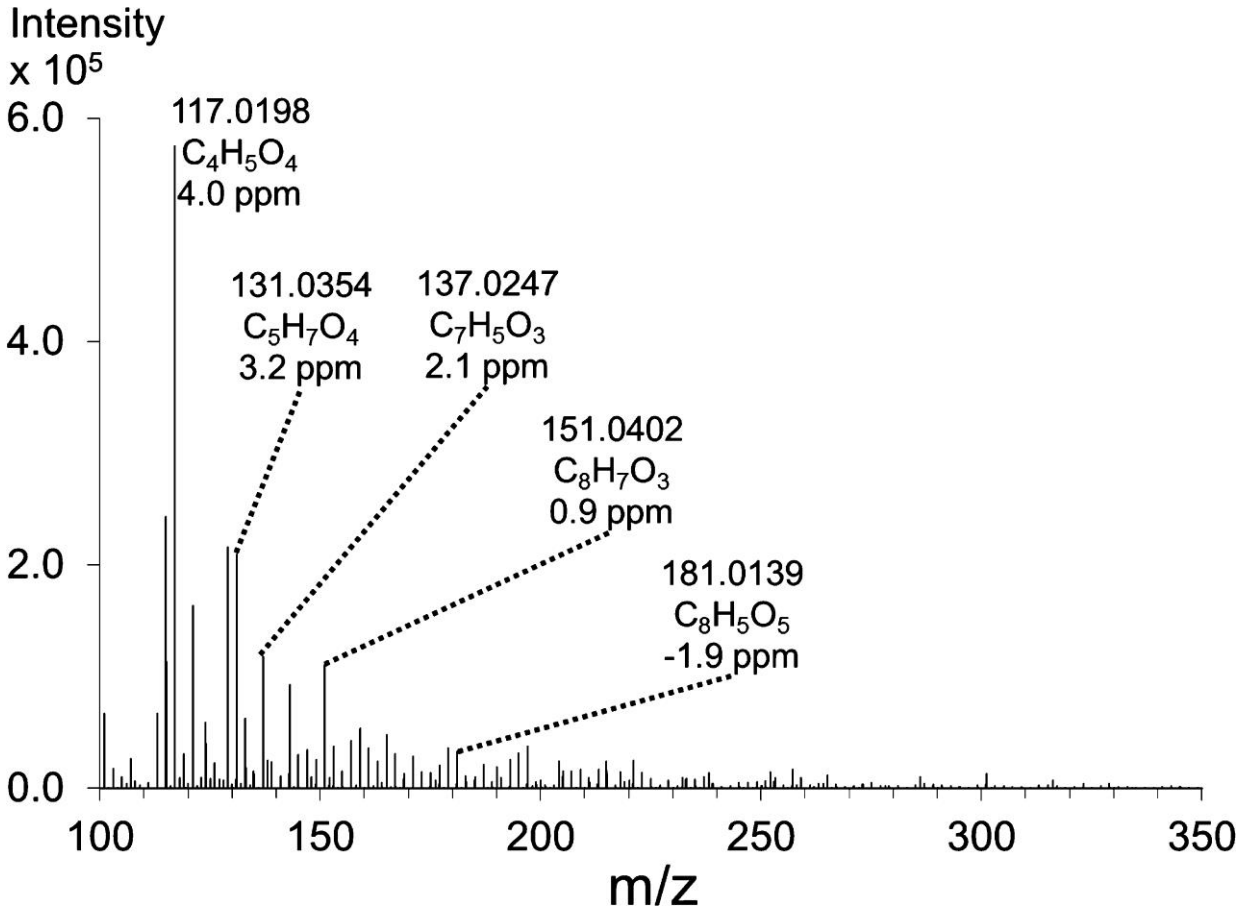

Figure 3. (−) ESI–MS spectrum of the water/methanol extract from fast pyrolysis char.

A few differences should be noted in understanding the ESI–MS spectra in negative-ion mode (Figure 3) compared to LDI–MS spectra in positive-ion mode (Figure 1). First, aromatic ring compounds are efficiently ionized in LDI through multiphoton absorption by aromatic rings [29]. In contrast, polar compounds with deprotonatable hydrogen are ionized in (−) ESI. Second, LDI produces molecular radical ions ($M^{+\bullet}$) with the same chemical composition as the original compounds, whereas the (−) ESI produces deprotonated ions ($[M - H]^-$) with one less hydrogen than its original molecule [30]. All ions in Figure 1 are even mass ions, and those in Figure 3 are odd mass ions, following the nitrogen rule. Third, LDI is operating at moderate vacuum conditions (~80 mTorr), while ESI is in atmospheric pressure. ESI–MS can effectively ionize volatile compounds, such as those at *m*/*z* 100–200 in Figure 3, which are not observed in LDI–MS.

Chemical composition analysis was performed for the spectrum shown in Figure 3, and 25 chemical compositions were confidently assigned. Figure 4A shows the relative abundance of each heteroatom class compound. The O4 compounds are most dominant, which is similar to LDI–MS analysis in Figure 2A. However, the DBE distribution of each heteroatom class shown in Figure 4B is completely different from that of LDI–MS (Figure 2B). Most of all, the aliphatic compounds (DBE < 4) are most abundant, followed by single-ring aromatic compounds with DBE of 4–7, while those in LDI–MS are mostly double-ring aromatic compounds with DBE of 9–13.

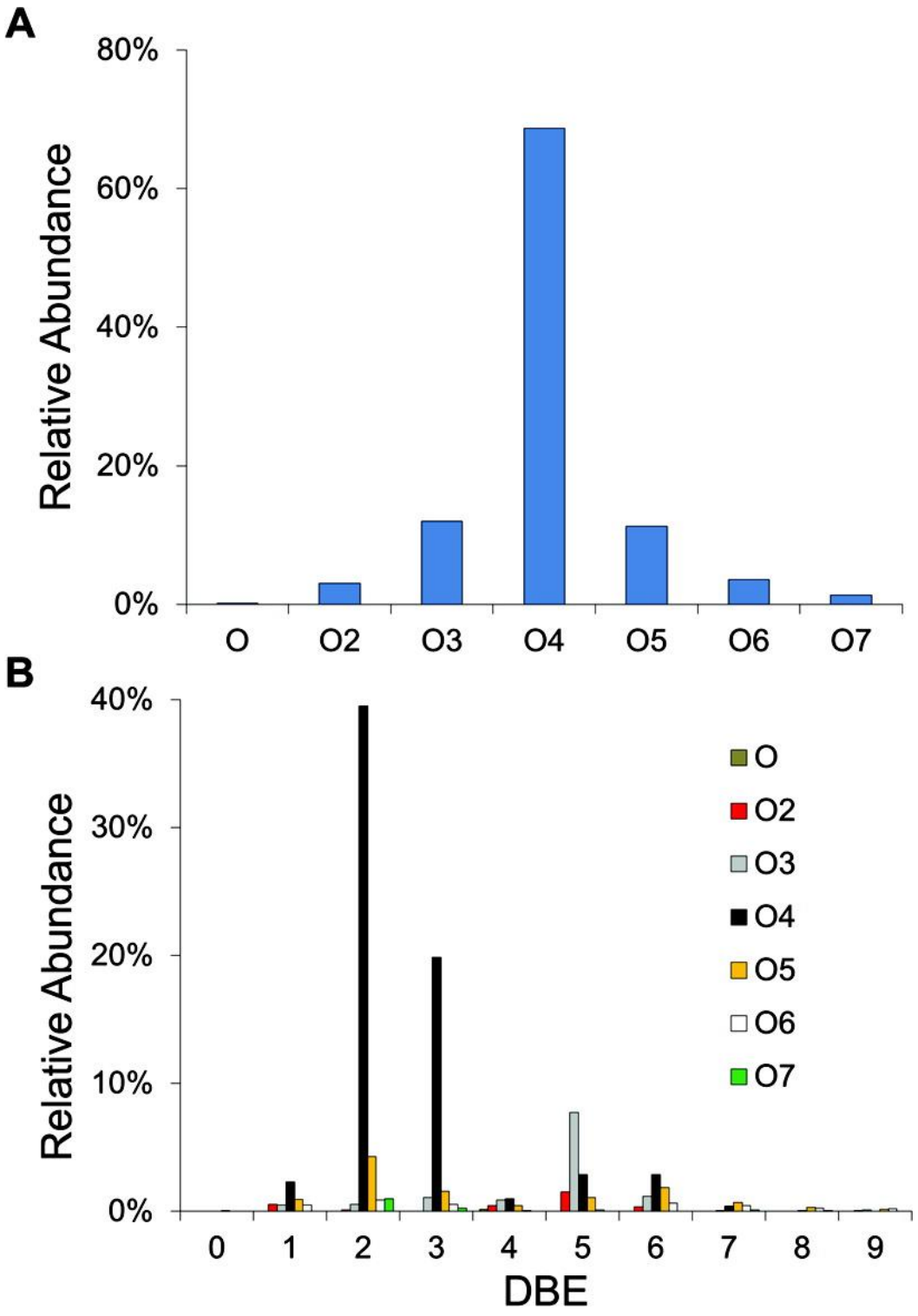

Figure 4. Chemical composition analysis of the (−) ESI–MS spectrum of water/methanol extracts of fast pyrolysis char shown in Figure 3: (A) heteroatom class distribution and (B) DBE distribution for each heteroatom class.

The O4 and O5 aliphatic compounds are extensively examined in our recent study of bio-oils in (−) ESI [21]. In short, they are mostly pyrolysis products of cellulose and hemicellulose. We call these polyhydroxylcyclic hydrocarbons "sugaric compounds" in the previous paper opposed to "phenolic compounds" from lignin pyrolysis. Levoglucosan, a well-known cellulose pyrolysis product, is present in Figure 3 at *m*/*z* 161 (deprotonated $C_6H_{10}O_5$; DBE = 2) but in much less amount than other major compounds. However, the relative ion abundances in (−) ESI are easily affected by pH or organic modifiers, and a further study is needed for the quantitative understanding [21]. The contour maps for the number of carbon versus DBE of O4 and O5 compounds are shown in Figure 5, and the phenolic (DBE ≥ 4) and carbohydrate-derived (DBE < 4) compounds are clearly distinguished on these plots. The O5 DBE of 2 compound with six carbons corresponds to levoglucosan ($C_6H_{10}O_5$), and the O4 DBE of 2 compound with five carbons corresponds to anhydropentose (either anhydroxylpyranose or anhydroarabinofuranose). However, other carbohydrate-derived compounds were not previously reported in any GC–MS or LC–MS studies of bio-oils. Overall, polar compounds from fast pyrolysis biochar are also similar to those of bio-oils [21]. Minor differences are suspected to have come from the difference in biomass.

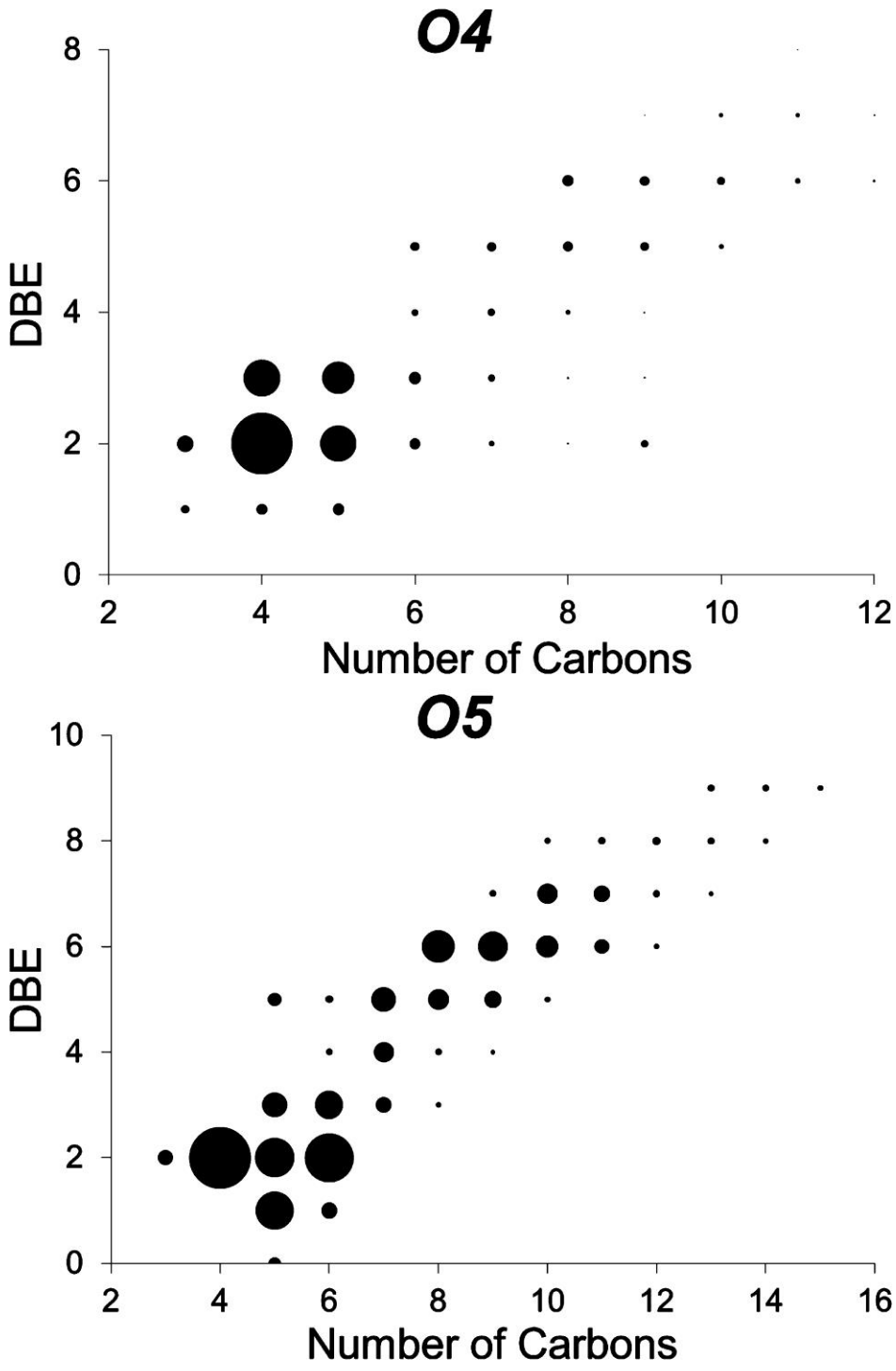

Figure 5. Contour maps of the number of carbons versus DBE for O_4 and O_5 compounds in the (−) ESI–MS spectrum of water/methanol extracts of fast pyrolysis biochar shown in Figure 3. The size of circles represents the intensity of corresponding ions.

Conclusion

High-resolution mass spectrometry was successfully adapted for molecular characterization of the organic compounds entrapped in biochar during pyrolysis and gasification of switchgrass. Molecular components extracted from fast pyrolysis biochar are consistent with previously studied bio-oil compounds and further confirmed in Figure 6 by the van Krevelen diagram [20,21]. In van Krevelen diagrams, elemental H/C and O/C ratios are calculated and plotted against each other (H/C versus O/C ratios). Molecules with similar chemical properties populate certain areas (shaded gray in Figure 6), which allows for visualization of relative changes in chemical composition resulting from thermochemical processes [18,31,32]. Furthermore, compounds can be assigned a modified aromaticity index (AI) to further classify formulas as non-aromatic ($AI < 0.5$), aromatic ($AI > 0.5$), and condensed aromatic ($AI \geq 0.67$) [18,33]. Water/methanol extracts from fast pyrolysis char (green circles) are dominated by non-aromatic, carbohydrate-derived products from holocellulose, with some minor phenolic compounds falling within the lignin group. Toluene extracts of fast pyrolysis char (blue circles) are centered around O/C and H/C ratios of 0.25 and 1.0, respectively, which are aromatic phenolic products from lignin pyrolysis ($AI > 0.5$). In contrast, the toluene extract of gasification biochar (red circles) is mostly along the *y* axis ($O/C = 0$), falling in the category of "coal, char, and soot". Collectively, Figure 6 suggests some of the bio-oil components are condensed on the surface of biochar during the char-filtering process. These molecules were not observed in gasification or slow pyrolysis biochar; instead, condensed aromatic hydrocarbons ($AI \geq 0.67$) were observed, particularly in high abundance for gasification biochar (red circles).

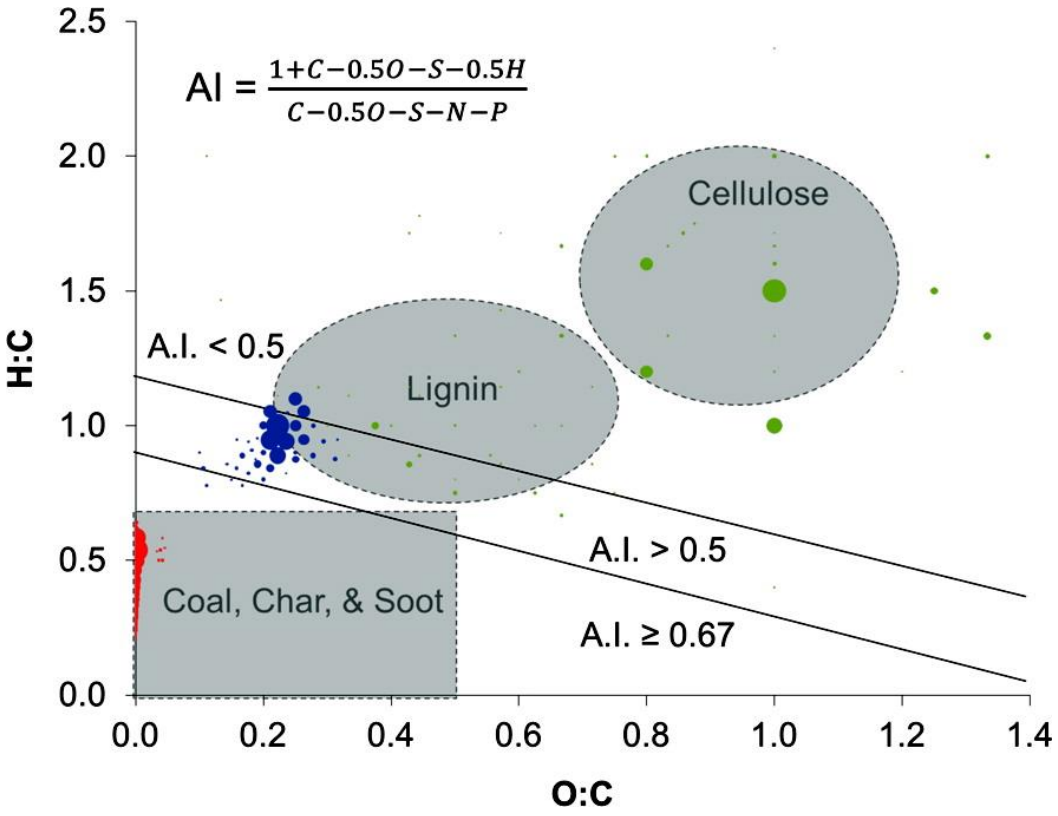

Figure 6. van Krevelen diagram of elemental H/C versus O/C ratios for pyrolysis extracts in water/methanol (green) and toluene (blue), as well as gasification extracts in toluene (red). The modified AI classifies formulas as non-aromatic (AI < 0.5), aromatic (AI > 0.5), and condensed aromatic (AI ≥ 0.67, adapted from Podgorski et al. [18]). The gray shading represents areas populated by compounds of similar chemical properties (adapted from Kim et al. [32]).

A molecular understanding of organic matter in biochar is often missing in typical biochar analysis. Some NMR or FTIR studies were performed, but most studies are done without separation from the char materials and indistinguishable from the functional groups of char itself. The previous VOC study using headspace GC–MS was limited only to very small organic molecules [13]. DAPPI–FT-ICR has been successful in directly analyzing biochar materials; however, it has not been adapted to investigate the difference between thermochemical processes [18]. In the current study, we found that significant differences are present depending upon the thermochemical processes. A further study would be needed for a quantitative assay of the

detected organic compounds and their chemical toxicity in agricultural field applications. For example, heavy rains might wash off carbohydrate-derived compounds from fast pyrolysis biochar, and the toxicity of entrapped organic molecules to plants or soil microbial systems may need to be evaluated. The petroleomic analysis adapted in the current study is useful in characterizing organic matter in biochar that are otherwise difficult to analyze in GC–MS, such as nonvolatile molecular compounds, thermally unstable compounds, or those not present in the electron impact–mass spectrometry (EI–MS) database.

Acknowledgments

This work was supported by a grant from ConocoPhillips. The authors thank Robert C. Brown, Center for Sustainable Environmental Technology at Iowa State University, and his group members for biochar samples and valuable discussions. The authors are also grateful to David Stranz, Sierra Analytics, for kindly providing an evaluator version of Composer software for this study. Erica A. Smith and D. Paul Cole acknowledge partial support from Graduate Assistance in Areas of National Need (GAANN) fellowship from the U.S. Department of Education.

References

[1] Laird, D.A.; Fleming, P.; Davis, D.D.; Horton, R.; Wang, B.; Karlen, D.L. *Geoderma* **2010**, 158, 443– 449.

[2] Laird, D.A. *Agron. J.* **2008**, 100, 178–181.

[3] Steinbeiss, S.; Gleixner, G.; Antonietti, M. *Soil Biol. Biochem.* **2009**, 41, 1301–1310.

[4] Rogovska, N.; Laird, D.; Cruse, R.; Fleming, P.; Parkin, T.; Meek, D. *Soil Sci. Soc. Am. J.* **2011**, 75, 871–879.

[5] Yu, X.-Y.; Ying, G.-G.; Kookana, R.S. *Chemosphere* **2009**, 76, 665–671.

[6] Yang, Y.; Sheng, G.; Huang, M. *Sci. Total Environ*. **2006**, 354, 170–178.

[7] Wen, B.; Li, R.-J.; Zhang, S.; Shan, X.-Q.; Fang, J.; Xiao, K.; Khan, S. U. *Environ. Pollut*. **2009**, 157, 968–974.

[8] Özçimen, D.; Ersoy-Meriçboyu, A. *Renewable Energy* **2010**, 35, 1319–1324.

[9] Sohi, S.P.; Krull, E.; Lopez-Capel, E.; Bol, R. *Adv*. *Agron*. **2010**, 105, 47–82.

[10] Brewer, C.E.; Schmidt-Rohr, K.; Satrio, J.A.; Brown, R.C. *Environ*. *Prog*. *Sustainable Energy* **2009**, 28, 386–396.

[11] Brewer, C.E.; Unger, R.; Schmidt-Rohr, K.; Brown, R.C. *Bioenergy Res*. **2011**, 4, 312–323.

[12] Lee, J.W.; Kidder, M.; Evans, B.R.; Paik, S.; Buchanan, A.C., III; Garten, C.T.; Brown, R.C. *Environ*. *Sci*. *Technol*. **2010**, 44, 7970–7974.

[13] Spokas, K.A.; Novak, J.M.; Stewart, C.E.; Cantrell, K.B.; Uchimiya, M.; DuSaire, M.G.; Ro, K.S. *Chemosphere* **2011**, 85, 869–882.

[14] Warnock, D.; Lehmann, J.; Kuyper, T.; Rillig, M. *Plant Soil* **2007**, 300, 9–20.

[15] Marshall, A.G.; Rodgers, R.P. *Acc*. *Chem*. *Res*. **2003**, 37, 53–59.

[16] Hughey, C.A.; Rodgers, R.P.; Marshall, A.G.; Qian, K.; Robbins, W.K. *Org*. *Geochem*. **2002**, 33, 743–759.

[17] Hughey, C.A.; Rodgers, R.P.; Marshall, A.G.; Walters, C.C.; Qian, K.; Mankiewicz, P. *Org*. *Geochem*. **2004**, 35, 863–880.

[18] Podgorski, D.C.; Hamdan, R.; McKenna, A.M.; Nyadong, L.; Rodgers, R.P.; Marshall, A.G.; Cooper, W.T. *Anal*. *Chem*. **2012**, 84, 1281–1287.

[19] Hockaday, W.C.; Grannas, A.M.; Kim, S.; Hatcher, P.G. *Org*. *Geochem*. **2006**, 37, 501–510.

[20] Smith, E.A.; Lee, Y.J. *Energy Fuels* **2010**, 24, 5190–5198.

[21] Smith, E.A.; Park, S.; Klein, A.T.; Lee, Y.J. *Energy Fuels* **2012**, 26, 3796–3802.

[22] Kroto, H.W.; Heath, J.R.; O'Brien, S.C.; Curl, R.F.; Smalley, R.E. *Nature* **1985**, 318, 162–163.

[23] Fan, M.; Marshall, W.; Daugaard, D.; Brown, R.C. *Bioresour*. *Technol*. **2004**, 93, 103–107.

[24] Evans, R.J.; Milne, T.A.; Soltys, M.N. *J*. *Anal*. *Appl*. *Pyrolysis* **1986**, 9, 207–236.

[25] Evans, R.J.; Milne, T.A. *Energy Fuels* **1987**, 1, 311–319.

[26] Hempfling, R.; Schulten, H.R. *Org*. *Geochem*. **1990**, 15, 131–145.

[27] Fang, X.; Xu, Y.; Yin, H.; Zhu, X.; Guo, Q. *Energy Fuels* **2009**, 23, 1775–1777.

[28] Bayerbach, R.; Nguyen, V.D.; Schurr, U.; Meier, D. *J*. *Anal*. *Appl*. *Pyrolysis* **2006**, 77, 95–101.

[29] Carpenter, D.L.; Deutch, S.P.; French, R.J. *Energy Fuels* **2007**, 21, 3036–3043.

[30] Amundson, L.M.; Eismin, R.J.; Reece, J.N.; Fu, M.; Habicht, S.C.; Mossman, A.B.; Shea, R.C.; Kenttämaa, H.I. *Energy Fuels* **2011**, 25, 3212–3222.

[31] Preston, C.M.; Schmidt, M.W.I. *Biogeosciences* **2006**, 3, 397–420.

[32] Kim, S.; Kramer, R.W.; Hatcher, P.G. *Anal*. *Chem*. **2003**, 75, 5336–5344.

[33] Dittmar, T.; Koch, B.P. *Mar*. *Chem*. **2006**, 102, 208–217.

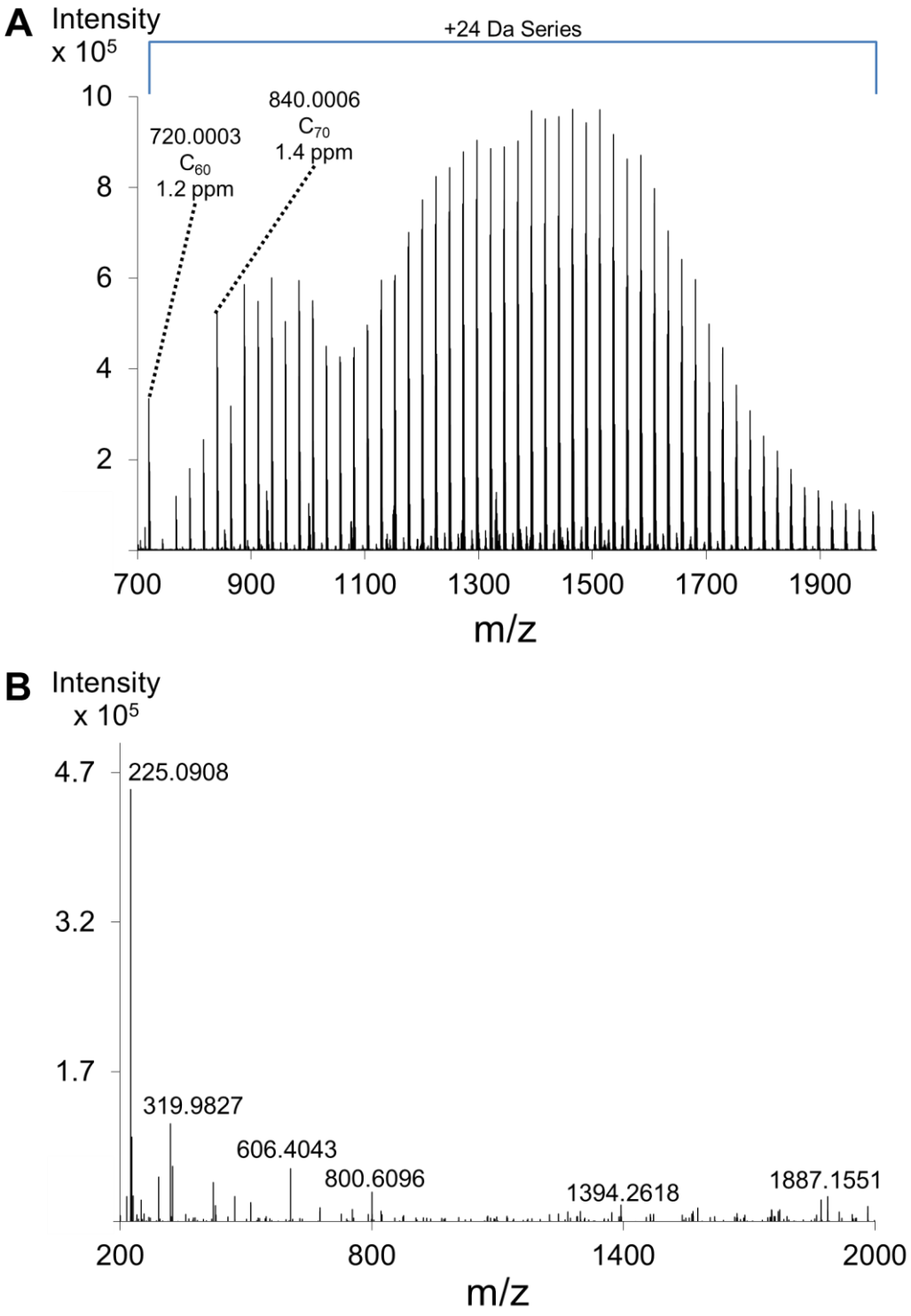

Supplemental Figure 1. (+) LDI-MS spectra obtained by direct analysis of **(A)** intact biochar produced from fast pyrolysis of switchgrass and **(B)** double sided tape.

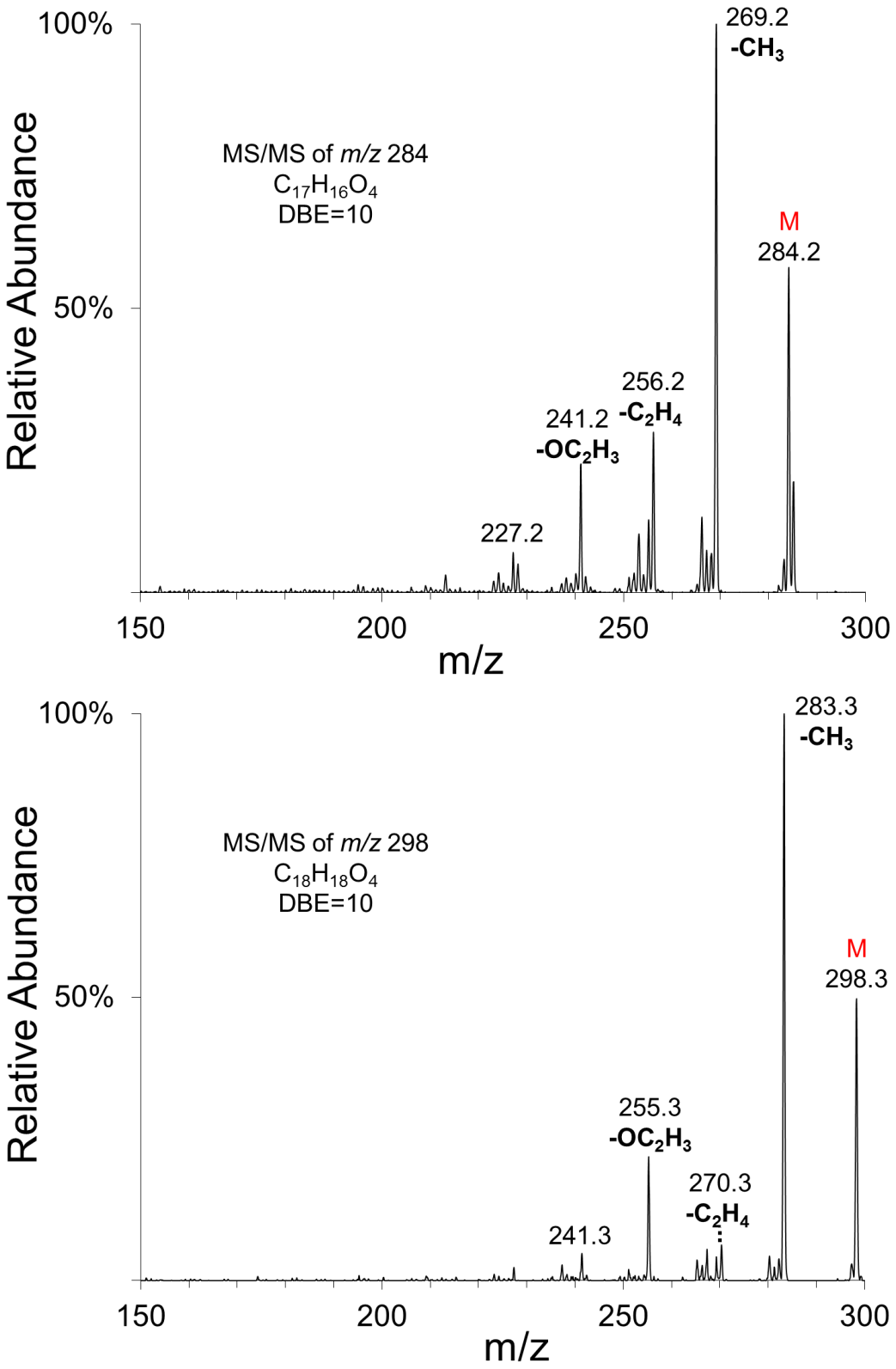

Supplemental Figure 2. MS/MS spectra of *m/z* 284 and 298, representing two O_4 compounds with DBEs of 10.

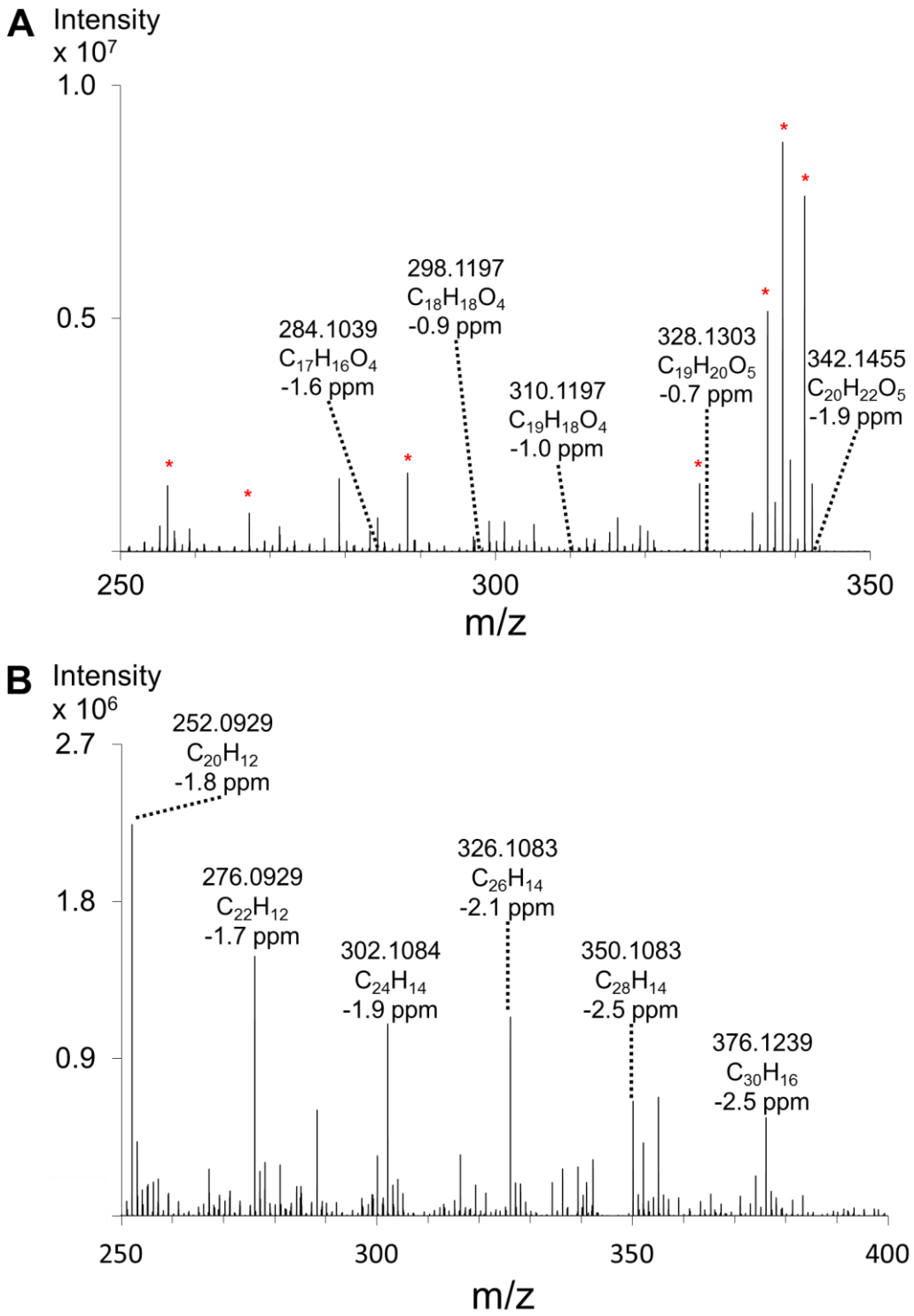

Supplemental Figure 3. (+) APPI-MS spectra confirming the presence of compounds extracted from chars produced by **(A)** fast pyrolysis and **(B)** gasification. Radical and protonated ions further complicate the spectra. (*) Contaminations mostly due to plastizers.

CHAPTER III
MOLECULAR CHARACTERIZATION OF NITROGEN-CONTAINING SPECIES IN SWITCHGRASS BIO-OILS AT VARIOUS HARVEST TIMES

A paper published in *Fuel*

Fuel **2013**, 111, 718–726.

D. Paul Cole, Erica A. Smith, Dustin Dalluge, Danielle M. Wilson,
Emily A. Heaton, Robert C. Brown, and Young Jin Lee

Abstract

Nitrogen-containing species in bio-oils obtained from fast pyrolysis of switchgrass were studied using high resolution mass spectrometry at various harvest times throughout the year. Almost three hundred chemical compositions of nitrogen species were determined through efficient ionization and accurate mass information. N_2 is the most abundant heteroatom class, followed by NO, N_2O, NO_2, and N_1 compounds. Nitrogen species, especially N_2 compounds, dominate the bio-oil spectra in early summer, but decrease significantly in later harvest times. From the contour plots of double bond equivalent versus carbon number and tandem mass spectrometric analysis, the major structural motif for N_1 and NO class compounds are assigned as pyridine and that of N_2 class compounds as imidazole. The dramatic decrease of N_2 class compounds in delayed harvest bio-oils is well correlated with the decomposition of proteins, represented by imidazole as a pyrolysis product of histidine, as the senescence of the perennial plant proceeds. Some of the heterocyclic aromatic compounds are also found in gas chromatography–mass spectrometry, further supporting our analysis.

Introduction

Thermochemical conversion of biomass to biofuel offers a promising biorenewable energy alternative in transportation fuels. In particular, bio-oils produced from fast pyrolysis of lignocellulosic biomass could be used for transportation needs after upstream refining [1]. Fast pyrolysis involves the rapid heating of biomass at temperatures near 500 °C without oxygen to produce biochar, syngas (CO and H_2), and bio-oil [2,3]. Bio-oil is a liquid fraction that contains an aqueous phase and an oily, water-insoluble phase. The physical properties of bio-oil resemble that of petroleum crude oils. However, their chemical compositions are quite different (bio-oil contains up to 50 wt% of oxygen and petroleum crude is almost completely oxygen free) mostly due to the difference in the processes involved; i.e., petroleum crudes are believed to be produced at moderate temperatures but through a very long process under high pressure [4].

Current bio-oil characterization is mostly focused on bulk property measurements such as pH, water content, ash content, viscosity, and elemental composition (CHNO analysis) [5,6]. Fourier transform infrared (FTIR) spectroscopy, nuclear magnetic resonance (NMR), and gas chromatography–mass spectrometry (GC–MS) are commonly utilized analytical methods to provide molecular details of bio-oils [7,8]. However, FTIR and NMR are unable to differentiate individual molecules and only provide average functional group information in the mixture. GC–MS is able to characterize individual molecules after GC separation, but identification is limited to volatile compounds present in the database.

High resolution mass spectrometry (HRMS) combined with soft ionization is a powerful tool for complex mixture analysis and is utilized for direct chemical composition analysis of thousands of molecular compounds in crude oils [9]. We have adapted this approach and successfully demonstrated its application for bio-oil analysis [10,11]. Over 800 chemical

compositions were characterized in red oak bio-oil using negative electrospray ionization (ESI) Fourier transform ion cyclotron resonance mass spectrometer (FT-ICR MS) [11]. In our previous studies, we have not detected any nitrogen-containing compounds, mostly because of the low nitrogen content in the biomass feedstock.

Switchgrass (*Panicum virgatum* L.) is a perennial, warm-season grass native to the midwestern U.S. that begins growth in early May, peaks in July, and senesces in the fall. Switchgrass has been described as a "model" biomass crop for bioenergy purposes [12]. Unlike woody biomass feedstock that typically has very low nitrogen content, switchgrass harvested prior to senescence has relatively high nitrogen content that could adversely affect its thermochemical conversion into biofuel due to its pollution effects and catalyst poisoning [13,14]. A recent study by Wilson et al. shows a promising result that late harvested switchgrass leads to low nitrogen content in both biomass feedstock and bio-oil products [5]. Yet, nitrogen still remains even in the latest harvest sample (0.1–0.2 wt% in April harvest bio-oil), which should be removed in the subsequent upgrading process. Unknown molecular characteristics of these nitrogen species could be a hurdle in designing appropriate chemical processes in the upgrading process.

HRMS analysis of nitrogen-containing compounds is routinely reported in petroleum oils [15,16]. There have been a few studies reporting nitrogen compounds in bio-oils [17,18]; however, there is no such study that investigates the structural details at a molecular level. In the current study, we have taken a systematic approach to study the molecular details of nitrogen species in switchgrass bio-oils. First, we compared several ionization methods for the analysis of nitrogen compounds in bio-oils. Second, we have performed a petroleomic analysis of HRMS data, particularly contour plots of double bond equivalent (DBE) versus carbon number, to infer

their structural motifs. Third, we performed tandem mass spectrometry (MS/MS) of a few target compounds to obtain structural details from their fragmentation patterns. In parallel, GC–MS analysis was performed to confirm the structural motifs of nitrogen species. Last, we applied this approach for the analysis of bio-oils from various harvest times to infer their molecular changes through a complete growth cycle.

Experimental Section

Materials

Switchgrass biomass and resultant bio-oils are essentially the same as previously reported [5]. Briefly, switchgrass trials were established in Boone County, IA, USA (41°55′N, 93°44′W) in spring 2008. Biomass was harvested from replicated plots (n = 4) at five different time points during the 2010 growing season (21 June, 20 July, 30 August, and 8 November in 2010, and 4 April in 2011), then dried to a constant weight, ground and sieved using the screen size of 200–700 μm. Bio-oil was produced in a free fall reactor at 550 °C by fast pyrolysis [5,19]. The bio-oils undergo a complex recovery system that fractionates the samples in order to reduce water content and acidity. In the present study, we used samples recovered from the third stage fraction (SF3). This fraction represents electrostatically precipitated aerosol droplets and typically contains the highest nitrogen content according to elemental analysis [5,19].

GC–MS analysis

The June bio-oil sample was used for GC–MS analysis because of its high nitrogen content. After dilution in methanol to 20% (by weight), 1 μL of sample was injected into a

Varian (Walnut Creek, CA, USA) 320-MS system coupled with a 450-GC. The 320-MS is a triple quadrupole mass spectrometer operated in electron ionization (EI) mode and scanned for *m*/*z* range of 35–650. The GC column was ZB-1701 (60 m × 250 μm, 0.25 μm film thickness; Phenomenex, Torrance, CA, USA) with 1 μL sample injection (275 °C) at a split ratio of 1:30. The temperature programming of the GC oven started at 35 °C for 3 min followed by a ramp of 3 °C min^{-1} to a final temperature of 280 °C, where it is held for 4 min.

The analysis of GC–MS data was performed using AMDIS software (NIST, v2.69) for automatic deconvolution and database search. The NIST08 EI-MS spectral library was used with a minimum match score of 750.

High resolution mass spectrometry

One representative bio-oil sample from each different harvest time was dissolved in methanol to 1 mg mL^{-1} to minimize chemical change during storage and stored in Nalgene bottles at 4 °C until analysis. Stock solutions were diluted to a final concentration of 0.1 mg mL^{-1} in 50:50 (v/v) methanol and water for electrospray ionization or 85:15 (v/v) methanol and toluene (Fisher Scientific, Fair Lawn, NJ, USA) for atmospheric pressure photoionization (APPI). A 50:50 (v/v) methanol and water solvent system was also used for APPI, but without much difference except lower ion counts and fewer low-mass ions (data not shown). Pyridine-d_5 was purchased from C/D/N Isotopes (Pointe-Claire, Quebec, Canada) and added as an internal standard to a final concentration of 1 μM for semi-quantification of nitrogen-containing species.

A majority of HRMS data acquisition was made using a linear ion trap-orbitrap mass spectrometer (LTQ-Orbitrap Discovery; Thermo Scientific, San Jose, CA, USA). The orbitrap

MS data was acquired at the mass resolving power of 30,000 at *m*/*z* 400 (transient of 0.4 s). A 5 kV source voltage was used for positive-ion ESI and −4.5 kV for negative-ion ESI. A vacuum ultraviolet (UV) lamp (PhotoMate, 10.0/10.2 eV; Syagen, Tustin, CA, USA) was used for APPI. For MS/MS analysis, isolation and fragmentation were performed using the linear ion trap of the instrument and mass spectral data acquisition was made using the orbitrap. Collision energies of 35–50% and precursor isolation width of ±1.0 Da were used for MS/MS. FT-ICR (7T Solarix, Bruker, Billerica, MA, USA) was also used for some of the initial experiments with positive ESI at 4.5 kV and with a time-of-flight of 0.4 and 0.6 ms and at the mass resolving power of 280,000 at *m*/*z* 400 (transient of 0.9 s).

Data analysis

Orbitrap MS data was exported to a text file using QualBrowser (Thermo Scientific) for all the peaks with their relative intensities above 1%, which is well above six times the baseline noise. The text file was imported to Composer (Sierra Analytics, Modesto, CA, USA) for calibration, chemical composition assignment, and visualization. Five-point internal calibration was performed by Composer using the exact masses of known peaks (e.g., pyridine-d_5 at *m*/*z* 85.0807 and levoglucosan at *m*/*z* 185.0420). The possible number of each element in chemical composition analysis was limited to 30 carbons, 60 hydrogens, 15 oxygens, and 5 nitrogens. Chemical compositions were assigned within a mass tolerance of 3 ppm in positive ion mode and 5 ppm in negative ion mode. Dopant peaks in APPI, mostly toluene and its oxidation products, are not included in the chemical composition analysis.

Results and Discussion

Evaluation of ionization methods for nitrogen speciation

The first step of this research was to find the most appropriate ionization method for the analysis of nitrogen-containing compounds in bio-oils. Fig. 1 compares the high resolution orbitrap mass spectra obtained with three atmospheric pressure ionization methods (positive ESI, negative ESI, and positive APPI) for switchgrass bio-oil. Bio-oil produced from the June harvest was used for this comparison because of its highest nitrogen content (1.24 wt% in biomass and 0.5 wt% in bio-oil) [5]. High mass resolving power and high mass accuracy of the orbitrap mass analyzer allowed separation of hundreds of bio-oil components and allowed for direct assignment of chemical compositions. Chemical compositions were assigned with less than 3 ppm mass error for positive ion mode and 5 ppm mass error for negative ion mode.

The three spectra in Figure 1 show quite different mass spectral patterns. The positive ESI spectrum is dominated by nitrogen-containing compounds and the other two are dominated by oxygen-containing compounds. All three orbitrap spectra are dominated by low-mass ions with most ions below *m*/*z* 200. It is known orbitrap data is biased for low-mass ions when low skimmer cone voltage is used to minimize in-source fragmentation [11]. Ionization efficiencies in atmospheric pressure ionization are greatly affected by molecular characteristics. Positive ESI produces mostly proton adducts or cation adducts, i.e., $[M + H]^+$ or $[M + Na]^+$; negative ESI produces mostly deprotonated compounds, i.e., $[M - H]^-$; and APPI produces either radical ions or protonated ions, i.e., $M^{+\cdot}$ or $[M + H]^+$. As a result, positive ESI over-represents those molecules with high proton affinity and negative ESI enhances ion signals for acidic compounds. Although APPI ionizes molecules rather globally, it is known to have high sensitivity for polyaromatic hydrocarbons [20]. The APPI spectrum is most complex due to the presence of

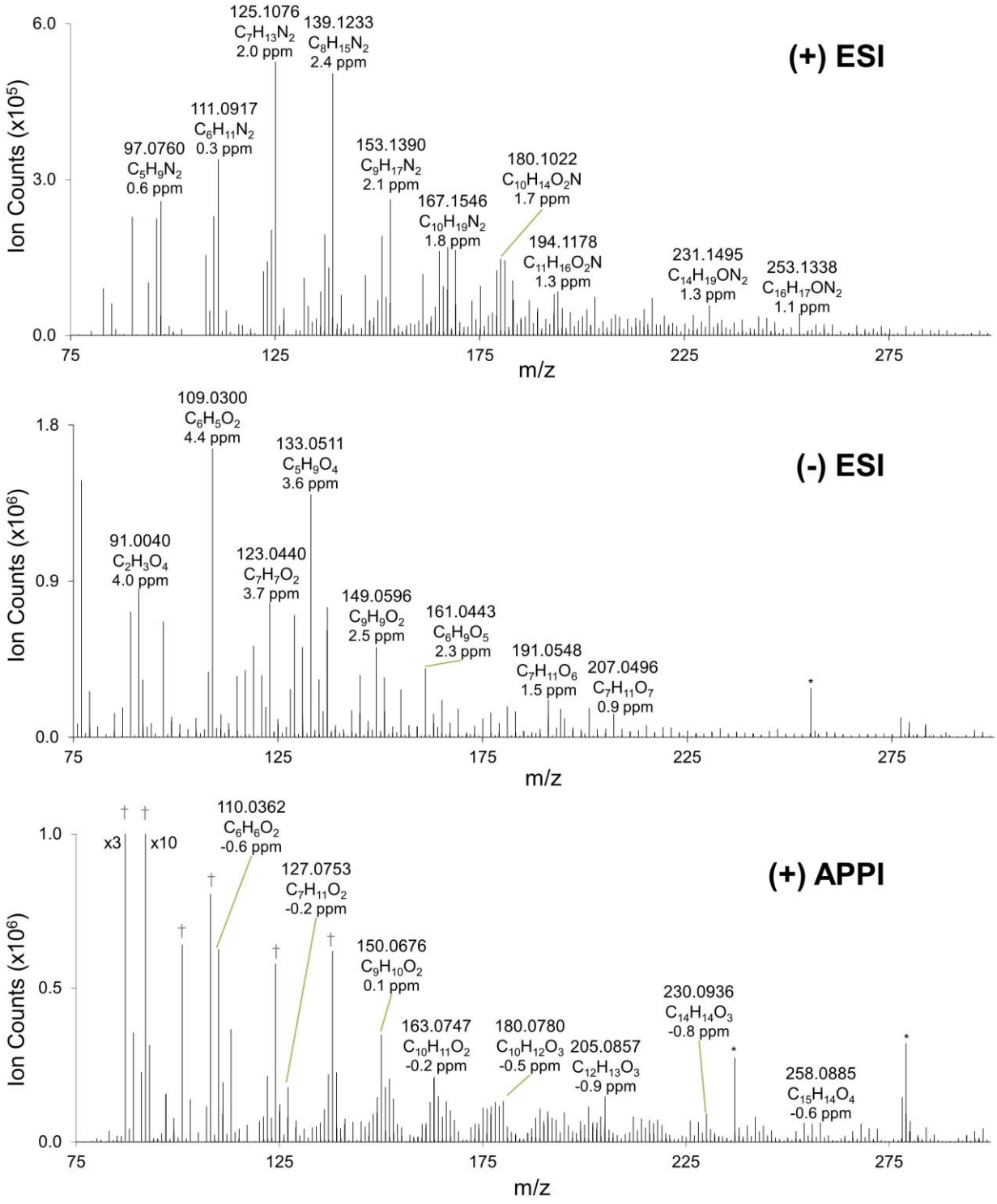

Figure 1. Orbitrap MS spectra of June harvest switchgrass bio-oil using positive ESI, negative ESI, and positive APPI. Chemical compositions are shown for the major peaks with corresponding mass errors. (*) Contamination; (†) Dopant peak.

both protonated molecules and molecular radical ions totaling 424 peaks above 1% relative intensities compared to 334 in positive ESI and 255 in negative ESI.

Negative ESI of red oak bio-oils has been extensively studied in our previous work [11], in which we determined over eight hundred chemical compositions derived from the pyrolysis of cellulose/hemicellulose and lignin. Specifically, low DBE and high oxygen compounds are assigned as pyrolysis products of cellulose/hemicellulose and high DBE oxygen compounds are assigned as pyrolysis products of lignin. The negative ESI mass spectrum obtained from switchgrass (Figure 1) is similar to that of the red oak bio-oil [11]. Some differences are observed between red oak and switchgrass. The major peaks in red oak bio-oils are also found in switchgrass, such as *m*/*z* 131.0354 ($C_5H_7O_4$) and 161.0459 ($C_6H_9O_5$), which were assigned as anhydropentose and levoglucosan, respectively; these are well known cellulose pyrolysis products. Major peaks in switchgrass bio-oils are mostly low oxygen aromatic compounds, i.e., $C_6H_5O_2$ (DBE = 4; e.g., benzenediol or furanylethanone), $C_7H_7O_2$ (DBE = 4; e.g., guaiacol), and $C_9H_9O_2$ (DBE = 5; e.g., vinylguaiacol), or high oxygen compounds with DBE of 1, i.e., $C_2H_3O_4$ and $C_5H_9O_4$. The difference seems to arise mostly from feedstock. For example, red oak has lignin with high syringol ($Ph(–OH)(–OCH_3)_2$) content, thus leading to higher oxygen aromatic compound production, while switchgrass has lignin with high guaiacol ($Ph(–OH)(–OCH_3)$) content, which leads to lower oxygen aromatic compounds [21].

Chemical composition analysis was performed for all three data sets in Figure 1. Figure 2 compares heteroatom class distributions of nitrogen species in (+) ESI and (+) APPI data. There are no detectable nitrogen compounds in (−) ESI data. It should be noted that most compounds in (+) APPI are oxygen-only compounds and not shown in the figure. In total, 95% of the total ion count is nitrogen-containing molecular species in (+) ESI and only 24% in (+)

APPI. In terms of the number of species, (+) ESI identified 263 nitrogen-containing compounds in total of 303 assigned (and nine unassigned) chemical compositions and (+) APPI identified 147 nitrogen-containing compounds out of 397 total assigned (and 13 unassigned) compositions. Not only absolute ion abundance, but also relative ion abundance shows a significant difference between (+) APPI and (+) ESI. Specifically, the relative ion abundance of N_1 and N_2 compounds was much lower in (+) APPI. The nitrogen-containing heteroatom classes detected in GC–MS (N_1, N_2, NO, NO_2, N_2O_2; Table 1) are all detected in relatively high ion abundance by ESI (Figure 2), whereas N_1 class is barely detected by APPI. We concluded (+) ESI is best suited to ionize nitrogen-containing compounds in bio-oils, particularly for the low-mass compounds that were the major focus in the current study. However, it should be noted that (+) ESI may not be the best method for other compounds as it may underrepresent them.

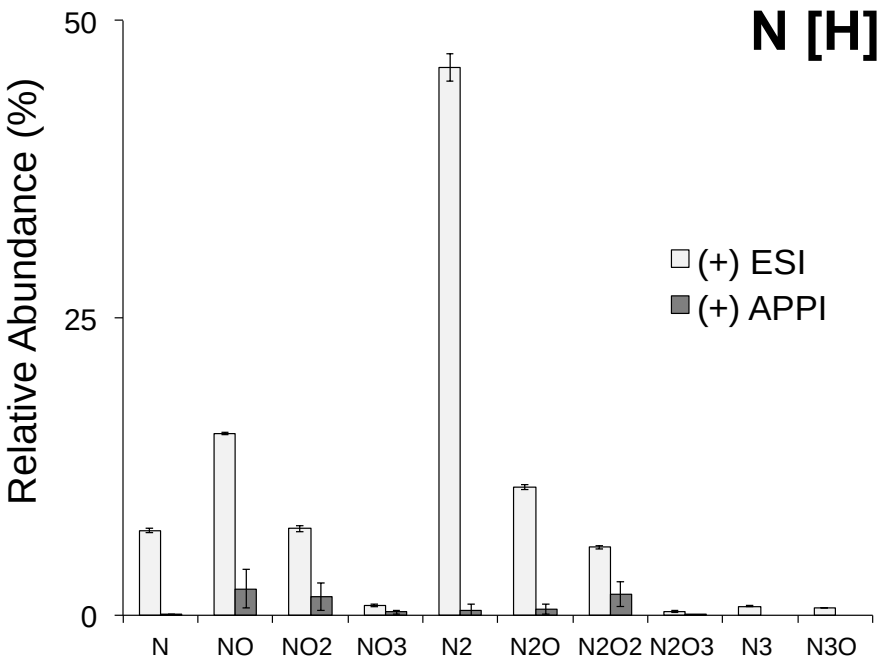

Figure 2. Heteroatom class distribution of nitrogen species for the June harvest bio-oil, comparing (+) ESI and (+) APPI. Error bars are standard deviation from multiple measurements.

Table 1. Nitrogen compounds in June-harvest bio-oils tentatively identified using GC–MS analysis and NIST EI-MS database search.

Retention time, min	Relative Abundance[a]	Composition	Molecular Weight	Assignment	NIST Score
13.9	1.5%	$C_4H_9NO_2$	103	Isobutyl nitrite	831
14.0	4.4%	C_5H_5N	79	Pyridine	879
14.2	2.3%	C_3H_5N	55	Ethyl isocyanide	968
17.2	1.0%	$C_6H_6N_2O_2$	138	4-Imidazoleacrylic acid	999
21.0	3.5%	$C_6H_{11}N$	97	4-Methyl-pentanenitrile	846
22.8	0.7%	$C_5H_6N_2$	94	3-Methylpyridazine	838
43.2	2.2%	C_5H_5NO	95	3-Pyridinol	752

[a] Relative abundance of ion count normalized against that of levoglucosan.

GC–MS analysis was performed for the June harvest bio-oil to confirm the presence of nitrogen-containing species. A total of seven nitrogen compounds were tentatively assigned in GC–MS analysis as summarized in Table 1. They are all top score matches and have a score of 800 or higher, except 3-pyridinol that has a score of 752, and the corresponding peaks are all present in our (+) ESI-orbitrap data. They are representing various classes of nitrogen compounds (N, NO, NO_2, N_2, N_2O_2 class compounds) that cover most of the major nitrogen classes in Figure 2 except N_2O. The overall coverage of nitrogen compounds in GC–MS analysis is very poor compared to (+) ESI-orbitrap with only seven identifications compared to 269. A critical limitation in GC–MS analysis is that most of the bio-oil compounds are not present in the NIST EI-MS database. They are produced through rapid depolymerization of biomass materials under excessive heat and do not necessarily result in stable, well known chemicals. Additionally, many of these compounds are nonvolatile and not amenable for GC–MS analysis. Only about 40

compounds are typically identified in GC–MS analysis while over 800 elemental compositions could be characterized in high resolution mass spectrometric analysis. Some of the nitrogen compounds in Table 1 are also reported by others; e.g., pyridinol by Mullen and Boateng [22].

FT-ICR, a HRMS with much higher mass resolving power, was also used to analyze the June and April harvest sample (Supplemental Figures 1 and 2). The FT-ICR spectra look quite different compared with orbitrap spectra. First of all, orbitrap shows mostly low-mass ions (<*m*/*z* 200) while FT-ICR shows mostly high-mass ions (>*m*/*z* 200). Previously, we could successfully optimize the FT-ICR experimental conditions to obtain similar spectrum with orbitrap in (−) ESI of red-oak bio-oils [11]; however, in (+) ESI of switchgrass bio-oils, we failed to optimize the experimental conditions to obtain similar result. As we previously discussed [11], both the instruments are biased for either low-mass ions (in orbitrap) or high-mass ions (in FT-ICR). The skimmer cone voltage was maintained low in orbitrap to minimize in-source fragmentation; however, it dramatically reduced the transmission efficiency of high-mass ions. In FT-ICR, the time-of-flight (TOF) between ion accumulation cell and ICR analyzer cell affects mass discrimination the most. High-mass ions are discriminated at low TOF and low-mass ions are discriminated at high TOF (see Supplemental Figures 1 and 2). But even with the lowest TOF allowed in our instrument (0.4 ms), low-mass ions are significantly discriminated especially below *m*/*z* 150. Additionally, sodium ion adducts are dominant for oxygenated species in FT-ICR, while they are relatively minor in orbitrap. In spite of these differences, both orbitrap and FT-ICR spectra show high ion abundance of nitrogen species in June harvest sample (Figure 3 and Supplemental Figure 1) and low ion abundance in April harvest sample (Figure 3 and Supplemental Figure 2). While both the instruments are biased for either low-mass or high-mass ions, we will focus on orbitrap data for the rest of the discussion because pyridine-

d_5 standard (*m*/*z* 85) added to correct overall ion signal changes between the samples (see the next section) could not be detected in FT-ICR spectra. It should be noted that the recently developed FT-ICR instrumentation that minimized the TOF effect might overcome the current limitation of low-mass ion bias [23,24].

Harvest time dependence on nitrogen species

Figure 3 shows a comparison of (+) ESI orbitrap spectra of switchgrass bio-oils from five different harvest times. Major peaks are labeled with the corresponding heteroatom classes and only their nominal masses are shown for simplicity. The major peaks in early harvest bio-oils (June, July, and August) are mostly nitrogen species while late harvest bio-oils (November and April) are almost all oxygen species. This is not surprising considering the major growth of switchgrass occurs during the summer months and it has high abundance of proteins during the growing season. In contrast, as plant senescence occurs after the summer months, proteins are decomposed and translocated to roots and rhizomes to be stored for new plant growth in the next spring [25]. Elemental nitrogen concentration of stage fraction 3 (SF3) bio-oils used in the current study shows the same trend (Table 2).

Table 2. Elemental nitrogen concentration (wt%) of stage fraction 3 (SF3) raw bio-oils at each harvest month used in the current study.

Harvest Month	Nitrogen Concentration (wt%)
June	2.24%
July	1.69%
August	0.99%
November	0.40%
April	0.25%

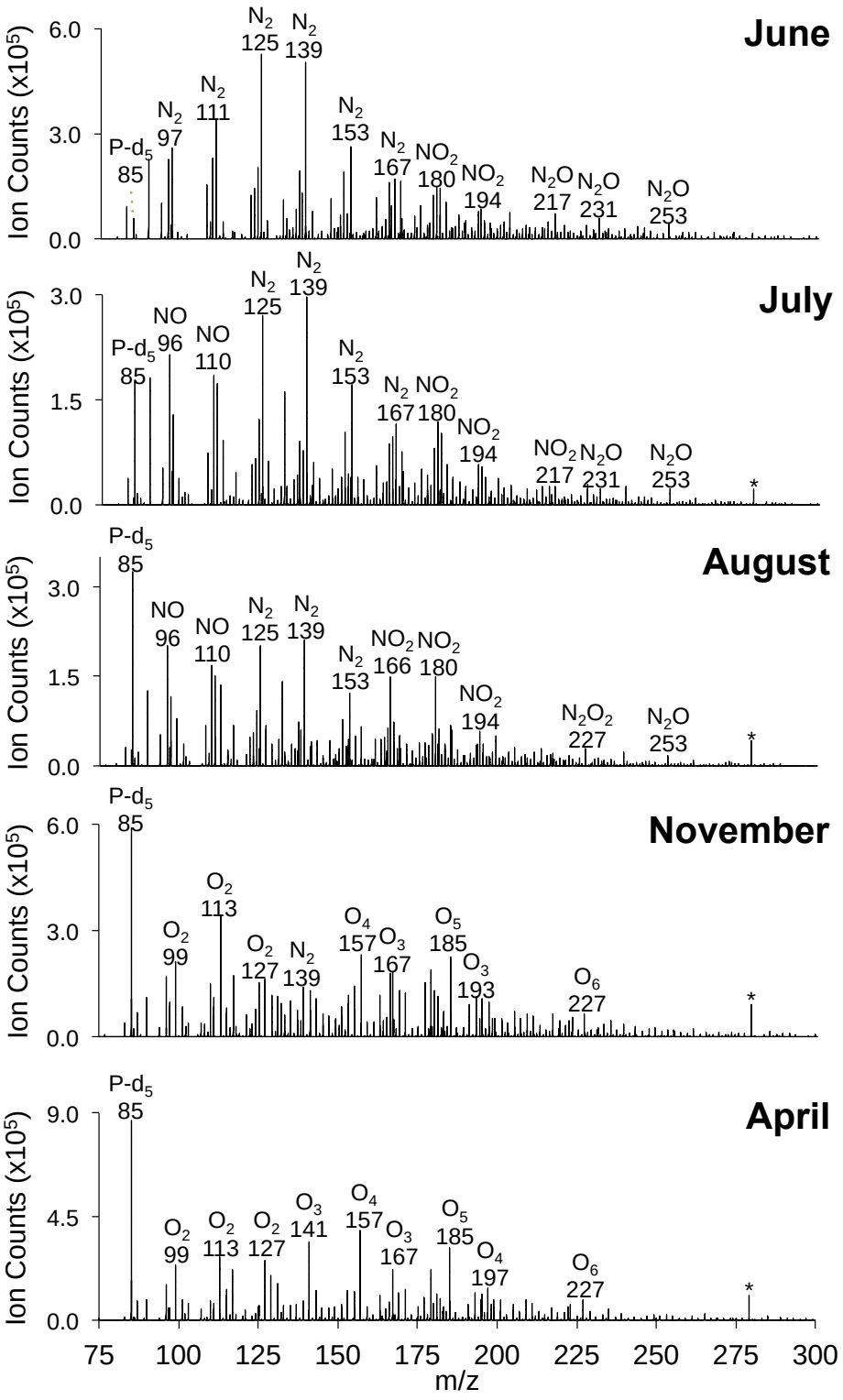

Figure 3. (+) ESI orbitrap spectra of switchgrass bio-oils from various harvest months. Nominal mass values are shown for major peaks along with their heteroatom class. Pyridine-d_5 (*m/z* 85, P-d_5) is added for the semi-quantitative comparison between samples. (*) Contamination.

For semi-quantitative comparison, the same amount of an isotopically labeled standard, pyridine-d_5 (*m*/*z* 85.0807), was added into each of the bio-oil samples as labeled as P-d_5 in Figure 3. While absolute quantification is possible only for pyridine with pyridine-d_5, semi-quantitative comparison of overall nitrogen compounds could be possible between the spectra. Namely, we expect the ion signal of pyridine-d_5 would allow us to correct most effects on ionization efficiency of nitrogen species influenced by factors such as pH or alkaline metal concentration. It should be noted that imidazole, another major structural motif along with pyridine (see the next section), has similar gas phase ion energetics (proton affinity of 930 and 942.8 kJ mol^{-1} and gas phase basicity of 898.1 and 909.2 kJ mol^{-1}, respectively for pyridine and imidazole)[26], and is expected to show similar ionization behavior with that of pyridine. It is very clear that even though the relative spectral pattern is similar between June and July bio-oils, the absolute amount of nitrogen compounds is much higher in the June harvest sample– the ratios of major peaks to pyridine-d_5 are much higher in June. The decrease of nitrogen-containing species further continued in August as evidenced by pyridine-d_5 being the most abundant peak. Several details should be noted concerning Figure 3. First, the ion counts for P-d_5 are gradually increasing with later harvest months because more free protons are available in electrospray droplets as nitrogen species decrease. Second, because of the use of only one standard, we cannot completely account for the difference in ionization efficiencies coming from various chemical functionalities, and this calibration should be only regarded as a correction of overall trend in nitrogen compounds. Last, it is noteworthy that the relative ion abundances of oxygen-only species are similar between November and April bio-oils.

To better understand these bio-oils, chemical composition analysis was performed using Composer (Sierra Analytics). Briefly, chemical compositions were assigned for hundreds of

compounds in each bio-oil sample based on their accurate masses. The heteroatom class distributions were constructed as shown in Figure 4 by combining the relative ion abundances for the same class compounds. For convenience, they were distinguished as three major groups: protonated nitrogen-containing compounds, $[C_cH_hO_oN_n + H]^+$(top), protonated oxygen-only compounds, $[C_cH_hO_o + H]^+$ (middle), and sodiated oxygen-only compounds, $[C_cH_hO_o + Na]^+$ (bottom). The presence of a low amount of sodium in the bio-oils resulted in sodium ion adducts of some multiply oxygenated compounds in ESI, while highly basic nitrogen-containing compounds resulted in only protonated compounds. Sodiated oxygen-only compounds have higher standard deviations, which is attributed to their low ion signals and sodium ions leached out from glass containers during the sample processing. Total of 287 nitrogen species were assigned from the bio-oils in five harvest times.

The nitrogen-containing compounds are clearly distinguished from oxygen-only compounds; the relative nitrogen content is greatest in the summer month samples (June, July, August) while the relative oxygen content is greatest in the after-summer samples (November, April). It should be noted the relative ion abundances in Figure 4 are normalized to the total ions of assigned species in each spectra. If we correct for ionization efficiency by comparing to the signal produced from pyridine-d_5, the overall nitrogen content would decrease even more dramatically at later harvest times.

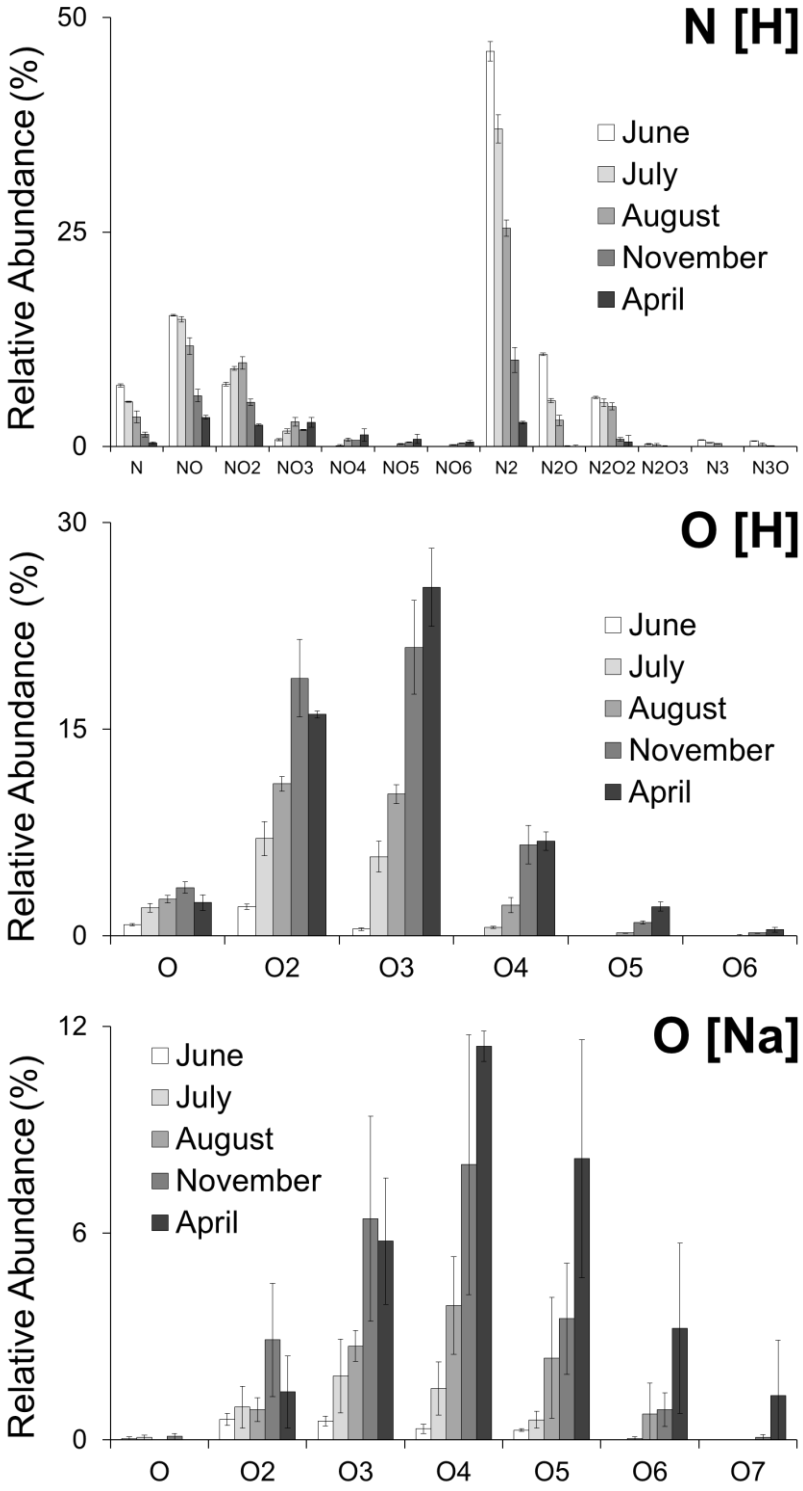

Figure 4. Heteroatom class distributions of (+) ESI orbitrap MS spectra at various harvest months; (top) protonated nitrogen compounds, (middle) protonated oxygen compounds, (bottom) sodiated oxygen compounds. Error bars are standard deviation from multiple measurements.

The dominant heteroatom class in bio-oil is the N_2 class, which accounts for nearly half of the total ion signals in June but decreases down to 10% or lower in the post-summer months. Other abundant nitrogen heteroatom classes are N_1, NO, NO_2, N_2O, and N_2O_2, which all show significant decrease after summer. The oxygen compounds are attributed to have originated from lignocellulosic biomass, as has been observed in red oak bio-oils [11]. Supplemental Figure 3 shows contour maps of protonated O_2 and O_3 compounds plotted against double bond equivalent (DBE) and carbon number for the April bio-oil. The most abundant O2 compound ($C_6H_8O_2$; DBE = 3) has the same chemical composition with cyclotene or methylfurfuryl alcohol, and the most abundant O_3 compound ($C_7H_8O_3$; DBE = 4) has the same chemical composition with methoxycatechol or hydroxymethyl furfural, suggesting good correlation with well-known bio-oil compounds in GC–MS.

It is quite intriguing to note that the relative ion abundances for N_2 and N_2O classes are decreasing significantly even between the summer months, from 46% in June to 25% in August for N_2 class and from 11% in June to 3% in August for N_2O; whereas the relative ion abundance change is minimal for some other nitrogen compounds, such as NO and NO_2. It may suggest there are at least two major nitrogen categories (e.g., photosynthetic and metabolic proteins and/or chlorophyll) in switchgrass that have different growth behaviors with one slowing down even during the summer months (e.g., N_2 and N_2O compounds) and the other collapsing only after summer (e.g., NO and NO_2 compounds). In addition, NOx ($x \geq 3$) compounds, unlike other compounds, are slightly increasing at the later harvest, although the amount is relatively minor. Further study could be performed to confirm this hypothesis through pyrolysis of model proteins.

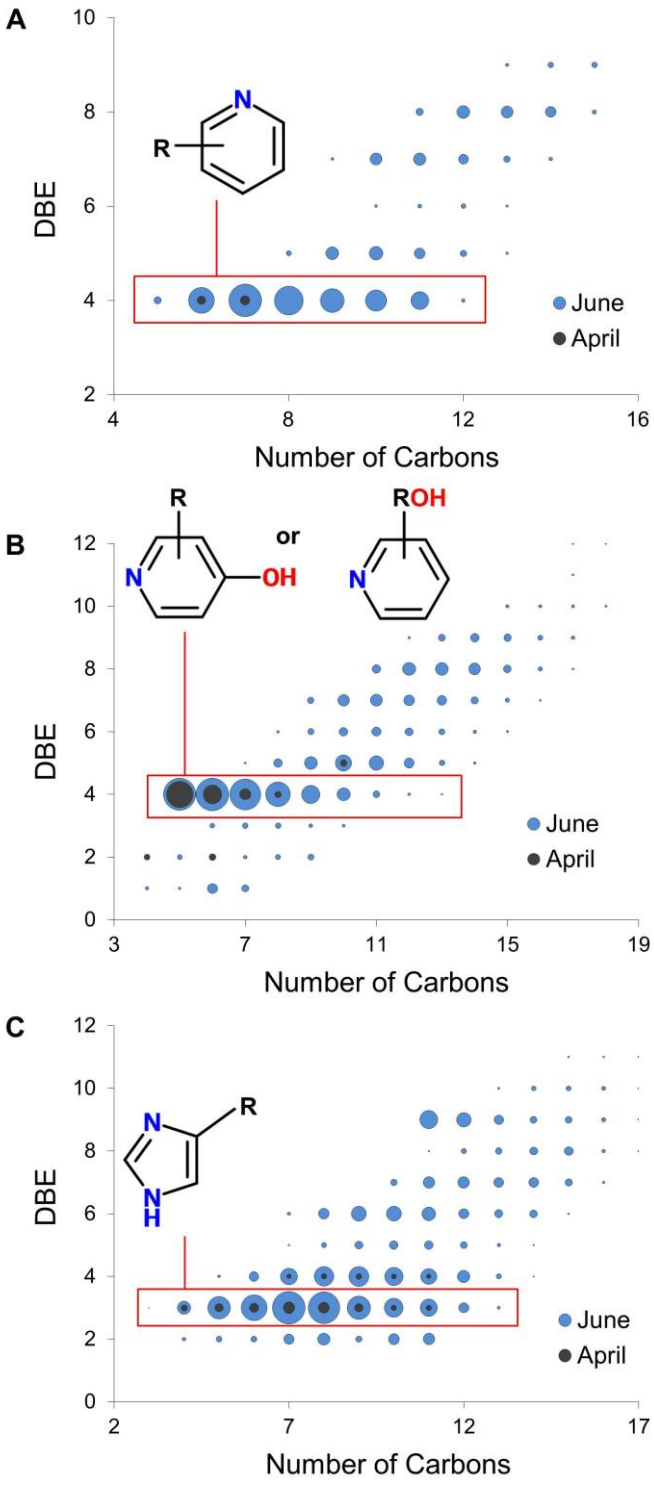

Figure 5. Contour plots of DBE vs. carbon number for N_1, NO, and N_2 compounds in positive ESI-MS spectrum for June and April harvest. Molecular structures are suggested for the boxed compounds. The size of the circles represents the relative % abundance.

Structural understanding of nitrogen compounds

Structural details of nitrogen compounds could be further understood through two-dimensional contour plots of DBE versus carbon numbers for a few nitrogen class compounds (N_1, NO, and N_2; Figure 5). DBE indicates unsaturation of the compounds corresponding to the sum of double bonds and cyclic rings, which is also called ring plus double bonds in EI-MS [27]. For the chemical formulae assigned as $[C_cH_hO_oN_n + H]^+$ in ESI-MS spectra, the DBE can be calculated from the equation, DBE = $c - ½\,h + ½\,n + 1$. The area of each circle in Figure 5 represents the relative ion intensities of the compounds for the corresponding DBE value and carbon number. For example, ethyl pyridine, $C_2H_5–C_5H_4N$, is an N_1 class compound with DBE of 4 and carbon number of 7 and would appear at the position corresponding to the largest circle in Figure 5A.

The DBE of 4 is the most abundant DBE group in the N_1 and NO class compounds as boxed in Figure 5A and B and the core structure is tentatively assigned as pyridine. We cannot avoid the possibility that some of them might have an aniline structure (C_6H_5-NH_2) that also has DBE of 4, but some evidences strongly support pyridine as the most likely structural motif. First, pyridine and pyridinol were detected in GC–MS analysis (Table 1) whereas aniline was not. Second, the least number of carbon is five among the boxed compounds (Figure 5). Third, MS/MS of a few compounds produced a fragment corresponding to the pyridine backbone ($[C_5H_5N + H]^+$, *m/z* 80) (Figure 6A and B; further discussed in detail below). Hence, we presume the boxed compounds in Figure 5A and B have pyridine as a structural motif with alkyl side chains. However, our analysis was based only on chemical formulae and we cannot distinguish structural isomers; i.e., ethyl pyridine cannot be distinguished from dimethyl pyridine. Higher DBE groups in Figure 5A and B (i.e., DBE of 5 or 6) are expected to have

additional double bond(s) in the alkyl side chain and DBE of 7 and 8 could correspond to polyaromatic hydrocarbons, such as quinoline or conjugated compounds of pyridine and benzene.

Unlike the N_1 and NO class compounds, the N_2 class has DBE of 3 as the most abundant DBE group (Figure 5C). The most likely structural motif for the boxed compounds could be either pyrazole or imidazole. We hypothesize that imidazole is the more likely structural motif arising from the pyrolysis of the histidine amino acid residue in protein. The DBE of 4 in Figure 5C might have a six-membered ring as a structural motif (pyrazine, pyrimidine, pyridazine) or five-membered ring (pyrazole, imidazole) with an additional double bond in the alkyl side chain. We presume the latter might be more abundant considering average of two additional carbons compared to DBE of 3, although pyridizine seems to be also present according to GC–MS data (Table 1).

In the April sample (Figure 5, dark circles), the boxed compounds are still present in significant amount while most of the high DBE compounds disappeared. It suggests that the nitrogen source in the biomass responsible for the proposed structural motifs is still present in the later harvest, but in much lower abundance.

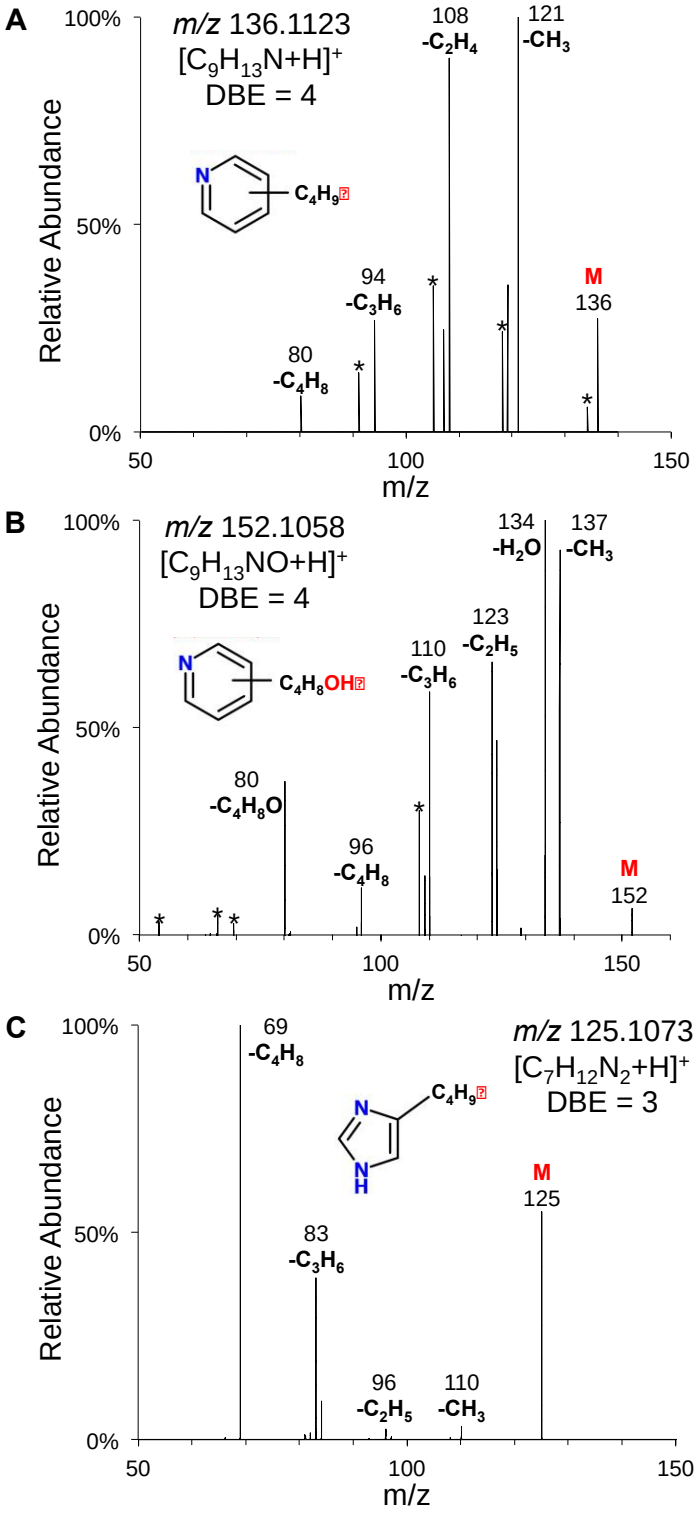

Figure 6. MS/MS spectra of *m/z* (A) 136.1, (B) 152.1, and (C) 125.1 representing N_1, NO, and N_2 compounds, respectively. Asterisk (*) represents fragment ions originating from the imperfect isolation of precursor ions, which have chemical elements not present in the intended precursor.

To further verify the structural details of N_1, NO, and N_2 class compounds hypothesized above, MS/MS was performed for a few selected compounds. For MS/MS, the precursor ion needs to be isolated first among the mixture of compounds inside the mass spectrometer for the subsequent activation and fragmentation. Because of the limited precursor ion isolation window, typically ±1 Da, MS/MS is often formidable for very complex mixtures without chromatographic separation. However, for a few major compounds in Figure 1, it was possible to isolate precursor ions with minimal interference within ±1 Da. Specifically, with our linear ion trap-orbitrap mass spectrometer, we were able to fragment precursor ions inside the ion trap and acquire high resolution tandem mass spectrum in the orbitrap (Figure 6). In this way, chemical compositions of the fragments can be also determined unambiguously. Because of the complexity of the bio-oil samples, precursor ions cannot be completely isolated without any interference (Supplemental Figure 4 for the zoomed-in precursor ions). However, high resolution tandem mass spectrum could differentiate most of fragments coming from the interferences; i.e., the fragment peaks labeled with asterisk in Figure 4 have chemical elements that are not present in the precursor.

In MS/MS of three representative compounds from the N_1, NO, and N_2 class, the lowest fragment mass ions are compatible with the hypothesized structural motifs; pyridine ($[C_5H_5N + H]^+$, *m*/*z* 80) for Figure 6A and B or imidazole ($[C_3H_3N_2 + H]^+$, *m*/*z* 69) for Figure 6C. We also performed MS^3 of these fragment ions (*m*/*z* 80 or *m*/*z* 69) by further isolating and activating inside the ion trap, which resulted in no additional fragmentation suggesting the rigidity of these structural motifs. Other fragments are mostly a series of alkyl losses that further supports our hypothesis that these compounds are alkylated forms of the structural motif. Loss of small alkyl groups comes from direct cleavage (e.g., $–CH_3$), but the loss of large alkyl groups seems to accompany the rearrangement of hydrogen to the pyridine or imidazole rings (e.g.,

$-C_3H_6$ or $-C_4H_8$). The water loss of $[C_9H_{13}NO + H]^+$ in Figure 6B is not likely to happen if the hydroxyl group is directly attached to the pyridine ring; i.e., Ar-OH typically results in OH loss rather than H_2O loss. Hence, the hydroxyl group in $C_9H_{13}NO$ is more likely attached to the alkyl side chain.

Conclusion

Positive electrospray high resolution mass spectrometry was successfully adapted for molecular characterization of nitrogen-containing species in fast pyrolysis switchgrass bio-oils. Positive ESI could efficiently and selectively ionize nitrogen compounds in bio-oils through the protonation of basic sites. Semi-quantitative comparison was made using pyridine-d_5 as an internal standard for bio-oils produced from biomass at various harvest times throughout the year. The decline of nitrogen species with harvest time is consistent with the previous finding for elemental nitrogen content in biomass and bio-oil. The most abundant nitrogen species was the N_2 heteroatom class and the relative amount decreases significantly over harvest time even during the summer months.

Through a contour plot and MS/MS analysis, the major structural motif for the N_2 heteroatom class was attributed to imidazole, produced as a result of the pyrolysis of histidine amino acid residue in proteins. Pyridine is regarded as the major structural motif for N_1 and NO class compounds from the same analysis. We hypothesize that heterocyclic aromatic rings, such as imidazole and pyridine, survive better in harsh pyrolysis conditions. We could identify pyridine and imidazole as nitrogen compounds in GC–MS analysis, further supporting the hypothesis of these compounds serving as structural motifs.

The current research clearly demonstrates the usefulness of HRMS in analyzing complex

bio-oils, particularly by providing molecular details of nitrogen-containing compounds and how they change over the harvest time. Almost three hundred nitrogen-containing species are identified in this approach, which is about forty times greater than the nitrogen species identified in GC–MS analysis. It is noteworthy that the advantages of HRMS arise from its much higher sensitivity and mass resolving power than those of GC–MS and its ability to characterize nonvolatile compounds, thus revealing that the complexity in pyrolysis bio-oils is far greater than previously thought in a simple GC–MS analysis. Our data suggests a few practical recommendations in the use of switchgrass biomass as a feedstock for pyrolysis. First of all, late harvest switchgrass should be used to minimize the nitrogen content in the final bio-oil products. Second, an upgrading process may need to be developed for further removal of nitrogen-containing species that are still left even at late harvest, such as hydrodenitrogenation with catalysts [28,29]. Lastly, pyridine and imidazole, major structural motifs for nitrogen compounds, could serve as excellent model compounds in such upgrading study.

Acknowledgments

This work is supported by a grant from Phillips66. The authors thank Marjorie Rover for the elemental and GC–MS analysis. The authors are also grateful to David Stranz, Sierra Analytics, for providing an evaluator version of Composer software for this study. E.A.S. and D.P.C. acknowledge partial support from Graduate Assistance in Areas of National Need (GAANN) fellowship from the U.S. Department of Education.

References

[1] Alonso, D.M.; Bond, J. Q.; Dumesic, J.A. *Green Chem*. **2010**, 12, 1492–1513.

[2] Czernik, S.; Bridgwater, A.V. *Energy Fuels* **2004**, 18, 590–598.

[3] Mohan, D.; Pittman, C.U.; Steele, P.H. *Energy Fuels* **2006**, 20, 848–889.

[4] Brown, M.T.; Protano, G.; Ulgiati, S. *Ecol*. *Modell*. **2011**, 222, 879–887.

[5] Wilson, D.M.; Dalluge, D.L.; Rover, M.; Heaton, E.A.; Brown, R.C. *Bioenergy Res*. **2013**, 6, 103–113.

[6] Peacocke, G.V.C.; Russel, P.A.; Jenkins, J.D.; Bridgwater, A.V. *Biomass Bioenergy* **1994**, 7, 169–178.

[7] Nayan, N.K.; Kumar, S.; Sing, R.K. *Bioresour*. *Technol*. **2012**, 124, 186–189.

[8] Pan, S.; Pu, Y.; Foston, M.; Ragauskas, A.J. *Bioenerg*. *Res*. **2013**, 6, 24–34.

[9] Marshall, A.G.; Rodgers, R.P. *Acc*. *Chem*. *Res*. **2004**, 37, 53–59.

[10] Smith, E.A.; Lee, Y.J. *Energy Fuels* **2010**, 24, 5190–5198.

[11] Smith, E.A.; Park, S.; Klein, A.T.; Lee, Y.J. *Energy Fuels* **2012**, 26, 3796–3802.

[12] Wright, L.; Turhollow, A. *Biomass Bioenergy* **2010**, 34, 851–868.

[13] Du, Y.; Chen, H.; Chen, R.; Xu, N. *Chem*. *Eng*. *J*. **2006**, 125, 9–14.

[14] Hegedüs, L.; Máthé, T. *Appl*. *Catal*. *A* **2002**, 226, 319–322.

[15] Podgorski, D.C.; McKenna, A.M.; Rodgers, R.P.; Marshall, A.G.; Cooper, W.T. *Anal*. *Chem*. **2012**, 84, 5085–5090.

[16] Qian, K.; Edwards, K.E.; Diehl, J.H.; Green L.A. *Energy Fuels* **2004,** 18, 1784–1791.

[17] Jarvis, J.M.; McKenna, A.M.; Hilten, R.N.; Das, K.C.; Rodgers, R.P.; Marshall, A.G. *Energy Fuels* 2012, 26, 3810–3815.

[18] Mullen, C.A.; Boateng, A.A. *Energy Fuels* **2008**, 22, 2104–2109.

[19] Ellens, C.J.; Brown, R.C. *Bioresour*. *Technol*., 2012, 103, 374–380.

[20] Bos, S.J.; van Leeuwen, S.M.; Karst, U. *Anal*. *Chem*. **2006**, 384, 85–99.

[21] Pandey, K.K. *J. Appl. Polym. Sci.* **1999**, 71, 1969–1975.

[22] Mullen, C.A.; Boateng, A.A. *Bioenergy Res.* **2011**, 4, 303–311.

[23] Kaiser, N.K.; Skulason, G.E.; Weisbrod, C.R.; Wu, S.; Zhang, K.; Prior, D.C. *Rapid Commun. Mass Spectrom.* **2008**, 22, 1955–1964.

[24] Kaiser, N.K.; Quinn, J.P.; Blakney, G.T.; Hendrickson, C.L.; Marshall, A.G. *J. Am. Soc. Mass Spectrom.* **2011**, 22, 1343–1351.

[25] Waramit, N.; Moore, K.J.; Heggenstaller, A.H. *Agron. J.* **2011**, 103, 655–662.

[26] http://www.webbook.nist.gov, accessed April 17, 2013.

[27] McLafferty, F.; Tureček, F. *University Science Books* Mill Valley, CA, **1993.**

[28] Izhar, S.; Uehara, S.; Yoshida, N.; Yamamoto, Y.; Morioka, T.; Nagai, M. *Fuel Process. Technol.* **2012**, 101, 10–15.

[29] Chishti, H.M.; Williams, P.T. *Fuel* **1999**, 78, 1805–1815.

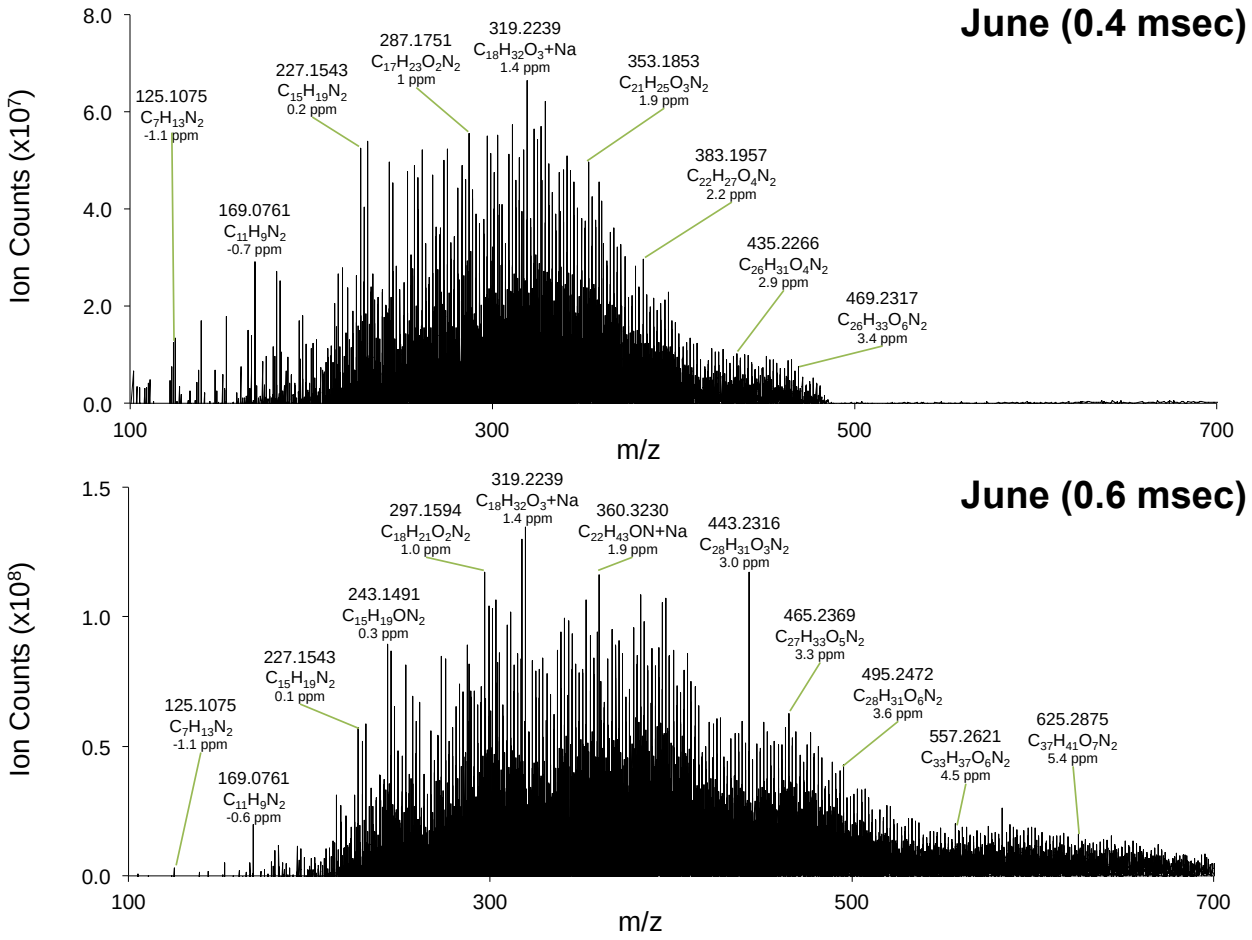

Supplemental Figure 1. (+) ESI FT-ICR spectra of June harvest bio-oils obtained with time-of-flight of 0.4 and 0.6 msec.

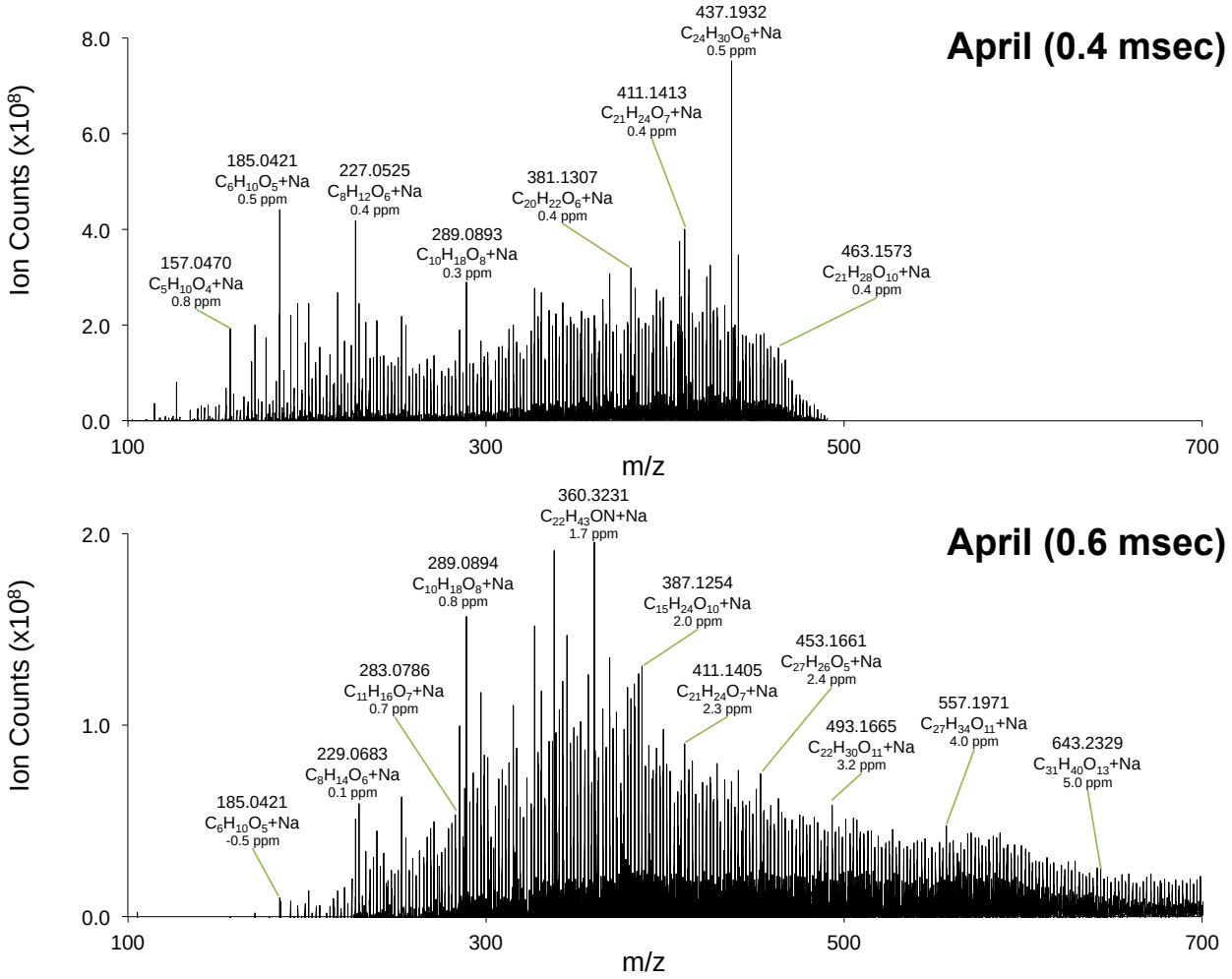

Supplemental Figure 2. (+) ESI FT-ICR spectra of April harvest bio-oils obtained with time-of-flight of 0.4 and 0.6 msec.

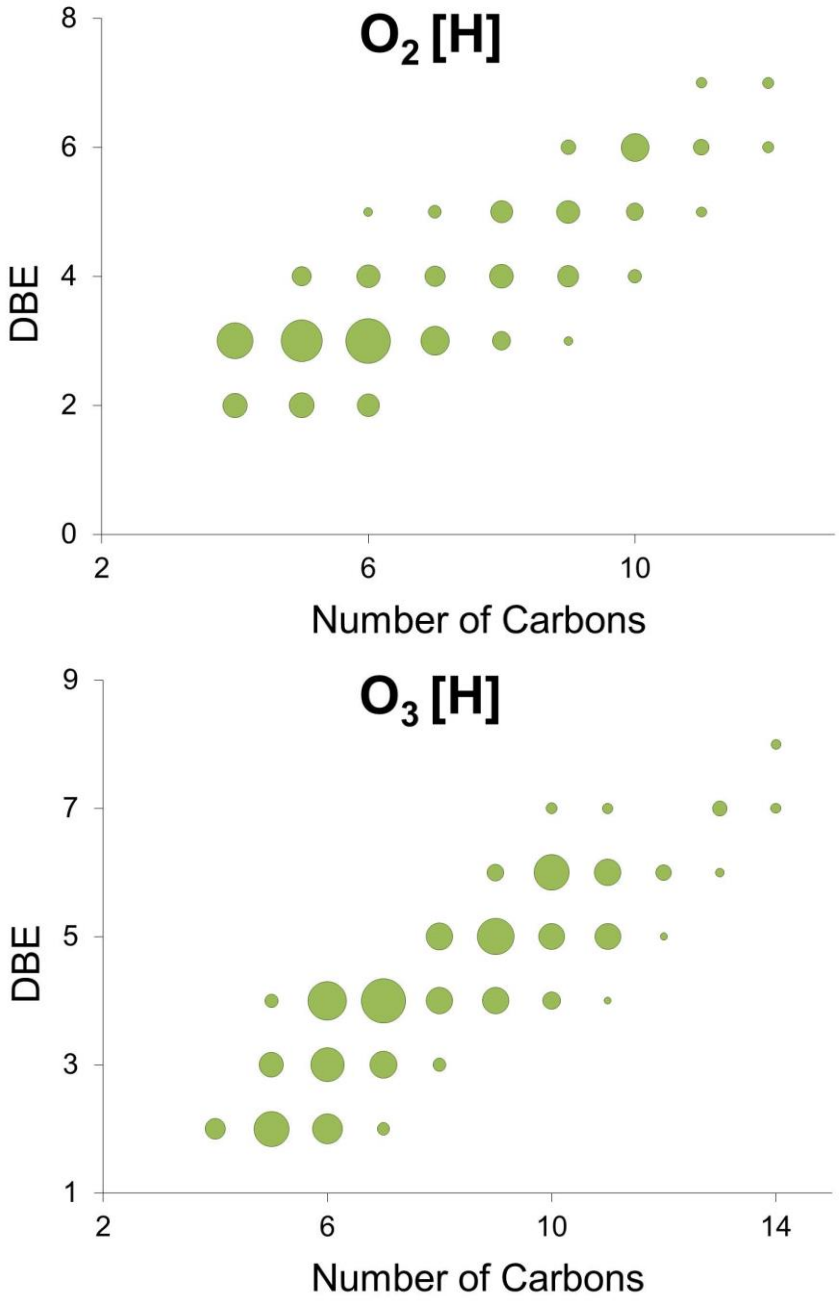

Supplemental Figure 3. Contour plots of DBE vs. carbon number for protonated O_2 and O_3 compounds in (+) ESI-MS spectrum for April harvest. The size of the circles represents the relative % abundance.

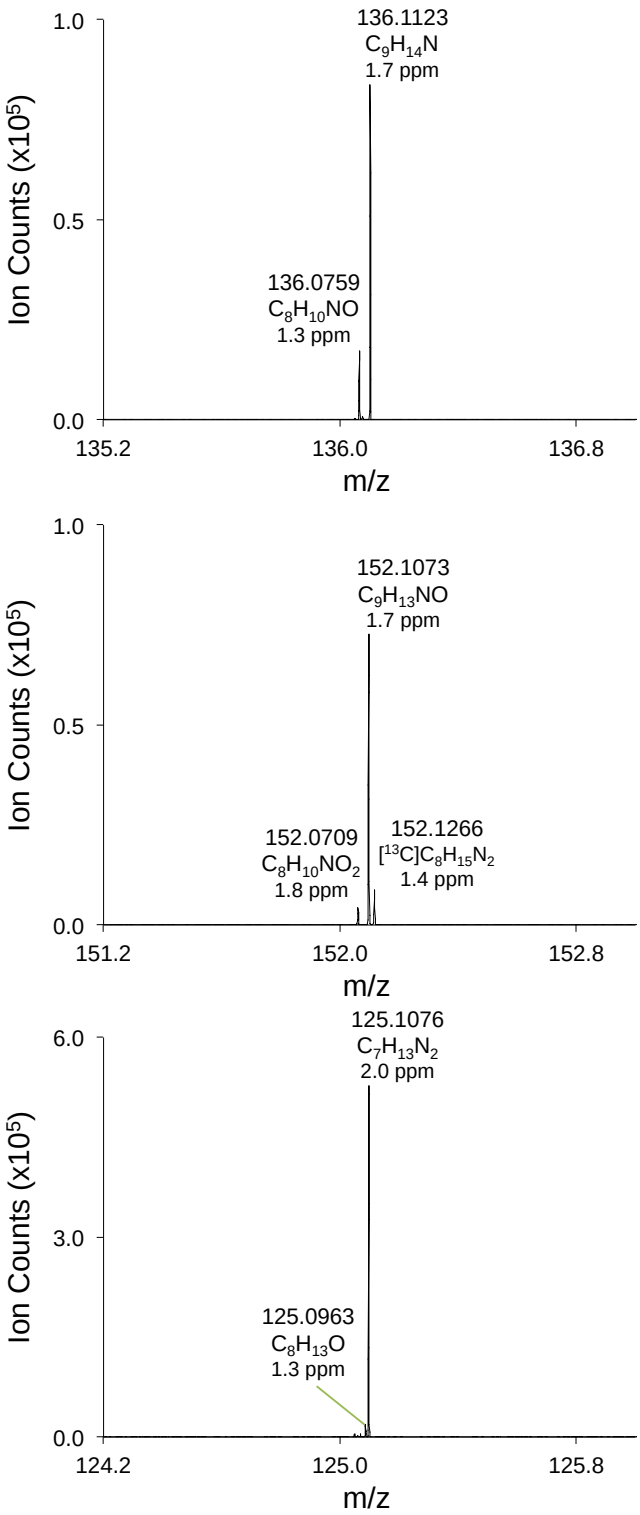

Supplemental Figure 4. Isolated precursor of m/z 136.1, 152.1, and 125.1 used for MS/MS in Figure 6.

CHAPTER IV
EFFECTIVE EVALUATION OF CATALYTIC DEOXYGENATION FOR IN SITU CATALYTIC FAST PYROLYSIS USING GAS CHROMATOGRAPHY-HIGH RESOLUTION MASS SPECTROMETRY

A paper published in *Journal of Analytical and Applied Pyrolysis*

J. Anal. Appl. Pyrolysis **2015**, 112, 129–134.

D. Paul Cole and Young Jin Lee

Abstract

Effective deoxygenation in catalytic fast pyrolysis (CFP) is crucial for bio-oil stabilization and its successful commercialization. Herein, we utilize a new analytical platform that couples gas chromatography (GC) to dopant-assisted atmospheric pressure chemical ionization (dAPCI) time-of-flight mass spectrometry (TOF MS) to evaluate catalytic deoxygenation of cellulose pyrolysis. Soft ionization and accurate mass measurement through dAPCI-TOF MS allows direct chemical composition analysis of GC-separated molecules, regardless of their presence in the database. The analytical approach was successfully demonstrated for its ability to evaluate catalytic efficiency of different catalysts and to monitor the change in CFP reaction products with catalyst-to-biomass load ratio. A total of 142 compounds could be analyzed with this approach compared to 38 compounds in traditional Py-GC-EI-MS analysis.

Introduction

Fast pyrolysis of biomass has shown promise toward producing biofuel for transportation needs [1]. The feedstock is rapidly heated in the absence of oxygen to convert lignocellulosic biomass to a high yielding liquid product called bio-oil. Bio-oil is chemically distinct from crude oils due to its high oxygen content. Because of its incompatibility with the existing infrastructure, upgrading is necessary prior to processing with conventional petroleum oil refinery [2,3]. Particularly important is an efficient deoxygenation or hydrodeoxygenation process with minimal carbon loss. It is shown that complete deoxygenation can be achieved through catalytic upgrading; however, bio-crude yield is often reduced as more oxygen is removed. This is because the deoxygenation is typically accomplished by CO or CO_2 removal through decarbonylation or decarboxylation [2,4]. Coke formation within the catalysts pore is another source of significant carbon loss [2,5]. Therefore, catalytic upgrading should be developed to maximize carbon yield and minimize oxygen content.

Catalytic fast pyrolysis (CFP), either *in situ* within the pyrolysis reactor or *ex situ* immediately after pyrolysis, upgrades bio-oil vapor before quenching as liquid products and minimizes secondary reactions or bio-oil aging compared to the liquid product upgrading [6]. *Ex situ* CFP has several advantages over *in situ* CFP. It can independently control catalytic reaction conditions and generally has less coke formation. Furthermore, *in situ* CFP is not currently applicable to a commercial scale reactor due to the need of frequent exchange and/or regeneration of catalysts. However, because of its simplicity and minimal modification to existing reactors, *in situ* CFP is commonly used for lab scale demonstrations and studying catalytic reactions. The production of fully deoxygenated aromatic compounds, e.g., benzene, toluene, and xylenes (BTX), was demonstrated via *in situ* CFP [7]. CFP conversion of biomass

has been extensively studied with zeolite catalysts [8-12]. For example, Foster et al. studied optimum silica-to-alumina ratio for ZSM-5 catalyst to maximize aromatic yield and minimize char formation [12].

Characterization of CFP products is crucial to understand the catalytic reactions and develop efficient deoxygenation processes. Gas chromatography–mass spectrometry (GC–MS) is most commonly used to characterize CFP products because of its high-resolution separation capability and large mass spectral database. Micropyrolyzer is often attached to GC–MS and a small quantity of biomass material is loaded after premixing with catalysts for *in situ* CFP product analysis [13]. Electron ionization (EI) is typically employed to ionize molecules for MS analysis. EI is non-selective and highly energetic, and produces significant fragmentations that can be used to search the database for identification. However, it is not as useful for those compounds that are absent in the database or have no molecular ion peak due to significant fragmentation, which is often the case for many bio-oil compounds.

Various soft ionization techniques have been developed to minimize fragmentations, such as chemical ionization (CI), field ionization (FI), vacuum UV photoionization (VUV PI) with or without infrared laser desorption (IR LD), and laser-ablation resonance-enhanced multiphoton ionization (LA-REMPI) [14-19]. Atmospheric pressure chemical ionization (APCI), originally developed for GC–MS several decades ago, has been recently re-introduced after successful commercialization for LC–MS instrumentation [20-23]. It has an additional advantage of utilizing high-resolution mass spectrometers developed for LC–MS in GC–MS applications [24]. However, APCI still produces significant fragmentations for volatile small molecules, which limits its application for bio-oil analysis with GC-APCI-MS. Dopant-assisted APCI (dAPCI) has been developed and utilized for LC–MS to reduce fragmentations and increase ionization

efficiency [25-26], but has not been demonstrated for GC–MS.

Here, we developed dAPCI for GC–MS with ammonia as a dopant gas and applied to *in situ* CFP product analysis. In particular, a high-resolution time-of-flight mass spectrometer (TOF MS) is utilized for mass spectral data acquisition to directly determine the chemical compositions of CFP products. Cellulose was used in this study with ZSM-5 and zeolite Y (ZY) catalysts. Catalytic deoxygenation efficiency in the *in situ* CFP of cellulose pyrolysis was successfully evaluated with the new GC-dAPCI-TOF MS approach.

Materials and Methods

Materials

Sigmacell Cellulose Type 20 (20 μm particle size) and zeolite Y catalyst (Si/Al = 3; BET surface area of 948 $m^2 g^{-1}$) were purchased from Sigma–Aldrich (St. Louis, MO, USA). The ZSM-5 catalyst (Si/Al = 23; BET surface area of 425 $m^2 g^{-1}$) was obtained from Alfa Aesar (Ward Hill, MA, USA). Both catalysts were calcined in ambient air at 550 °C for 6 h inside an oven to convert from ammonium to proton form prior to use.

Pyrolysis – GC–MS-TOF MS experiments

Pyrolysis studies were carried out using a drop-tube microfurnace pyrolyzer (Frontier Laboratories 3030S Micropyrolyzer, Fukushima, Japan) installed onto an Agilent 7890A gas chromatograph (Palo Alto, CA, USA). The GC is coupled with an Agilent 6200 time-of-flight mass spectrometer through an Agilent G3212 APCI interface. The GC separation was performed using a fused silica DB-1701 column (30 m × 0.25 mm i.d. × 0.25 μm). The oven temperature was programmed at an initial temperature of 35 °C for 5 min, ramped at 4 °C min^{-1} to a final

temperature of 260 °C, and held for 5 min. Ultrahigh purity helium gas was used as a carrier gas with a flow rate of 100 mL min^{-1} through the pyrolyzer. The gas flow was split 100:1 at the GC inlet resulting in a column flow rate of 1 mL min^{-1}. High purity ammonia gas (500 ppm in He; Praxair, Dansbury, CT, USA) was introduced into the APCI chamber at a flow rate of 1 mL min^{-1} through a zero-dead volume tee that was installed in the GC oven. The pyrolyzer inlet, GC inlet, and GC/APCI transfer tube interfaces were set to 280 °C. APCI was operated at a corona discharge of 1 kV and the MS inlet was heated to 325 °C with a drying gas flow of 5 L min^{-1}. TOF MS has a scan speed faster than 1 ms per microscan for a mass range of *m*/*z* 60–1000, but averaged and saved every second.

Catalyst effectiveness during CFP was studied at different catalyst-to-cellulose load ratios (0:1, 1:1, 5:1, 10:1 by weight). A total of 500 μg of premixed cellulose and catalyst mixture were exactly weighed into sample cups prior to dropping into the microfurnace set at a pyrolysis temperature of 500 °C. For semi-quantitative analysis, extracted ion chromatograms (EIC) were generated in MassHunter Qualitative Data Analysis software (Agilent) based on the exact mass of each compound of interest, and integrated over the corresponding EIC peaks at the given retention time. Integrated EIC peak area values were exported to Excel and normalized on a per 100 μg cellulose basis. All the chemical compositions assigned in Supplemental Table 1 are not present in a blank measurement and have signals greater than 0.1% relative abundance of the base peak, which is more than 6 times the base line noise.

For comparison, pyrolysis–GC-EI-MS analysis was performed for cellulose and a 1:1 mixture of ZSM-5:cellulose using Agilent 5975C MSD operated in EI mode with scanning *m*/*z* range of 35–650. All other conditions are exactly the same including pyrolysis conditions and GC column and programing. AMDIS software (NIST, v2.71, Build 134.27) was

used for analysis of Py–GC-EI-MS data for automatic deconvolution and database search. The NIST EI–MS spectral library (v2.0 g, 2011) was used with a minimum match score of 750.

Results and Discussion

Dopant-assisted APCI for GC-TOF MS

We have developed dopant-assisted APCI for GC–MS. Figure 1 shows the schematic diagram of this instrumentation and illustrates the dAPCI region. A micropyrolyzer is directly attached to a GC for pyrolysis-GC-MS (Py-GC-MS) analysis. Time-of-flight mass spectrometer is used for mass spectrometric measurements, which is essential due to its high mass resolution (R = 12,500 at m/z 600). Unlike typical GC–MS, where electron ionization (EI) is used for fragmentation and database search, we softly ionize the molecules with dAPCI and directly determine the chemical compositions of molecules from the accurate mass information.

For dAPCI, pre-heated ammonia gas (500 ppm in helium) is fed through a tee inside the GC oven, flowing outside the GC column, and introduced to APCI interface as a sheath gas (inset diagram of Figure 1). APCI corona discharge region is dominated by ammonia gas, predominantly ionizing ammonia to form ammonium cation, which then ionizes analyte molecules via protonation or ammonium adduct formation. Because analytes are indirectly ionized, as in CI, it is much softer than APCI without dopant gas. Furthermore, any extra internal energy during protonation or ammonium adduct formation (e.g., proton affinity difference between analytes and ammonia in case of protonation) is rapidly cooled down through millions of collisions with atmospheric molecules before they are injected into the mass spectrometer; thus, dAPCI produces almost no fragmentation. In typical CI occurring inside vacuum, there is not sufficient collisional cooling and extra internal energy leads to significant fragmentations.

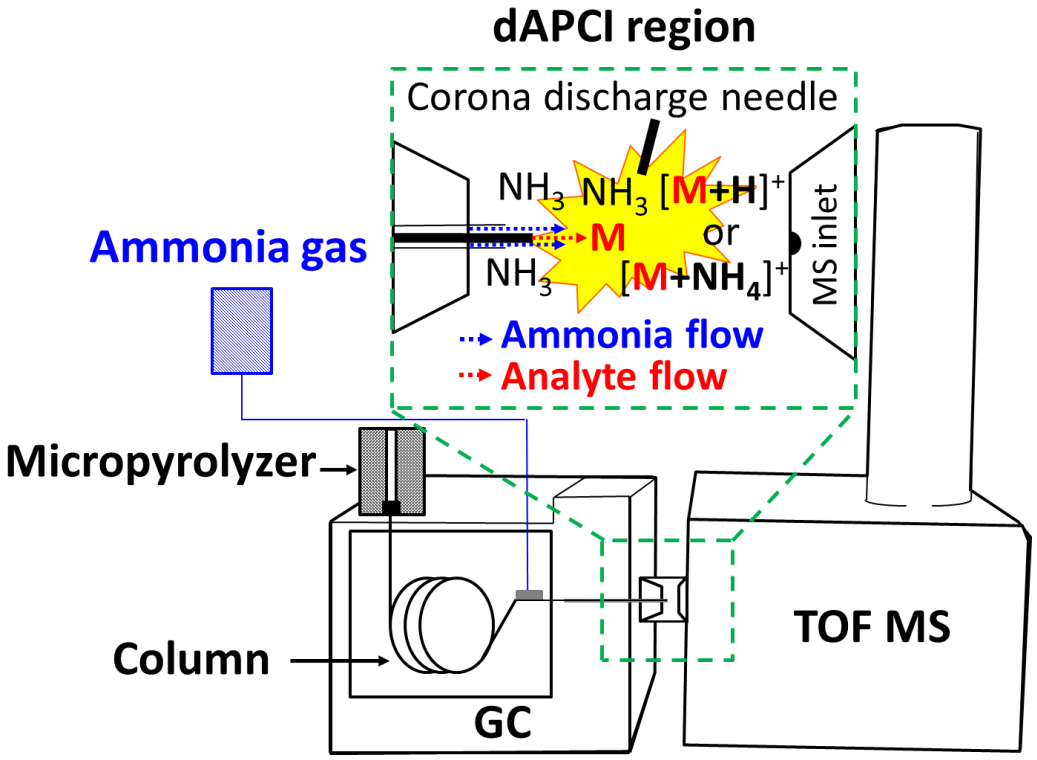

Figure 1. A schematic diagram of the Py-GC-dAPCI-TOF MS system used in the study. The inset figure shows the details of the dopant-assisted atmospheric pressure chemical ionization region.

Figure 2 shows levoglucosan mass spectra with and without ammonia dopant gas. Without dopant, levoglucosan is detected as a protonated ion with significant fragmentation of one or two water loss(es). However, with ammonia, there is almost no fragmentation and levoglucosan is detected as an ammonium adduct with 20 times signal improvement. It is in contrast to EI where levoglucosan or other carbohydrate molecules are completely broken apart and no molecular ion can be observed. Overall, wide classes of compounds are ionized by dAPCI with no or minimal fragmentations; multi-oxygenated compounds (e.g., furans and anhydrosugars) are mostly ionized as an ammonium adduct, phenolic compounds produced in

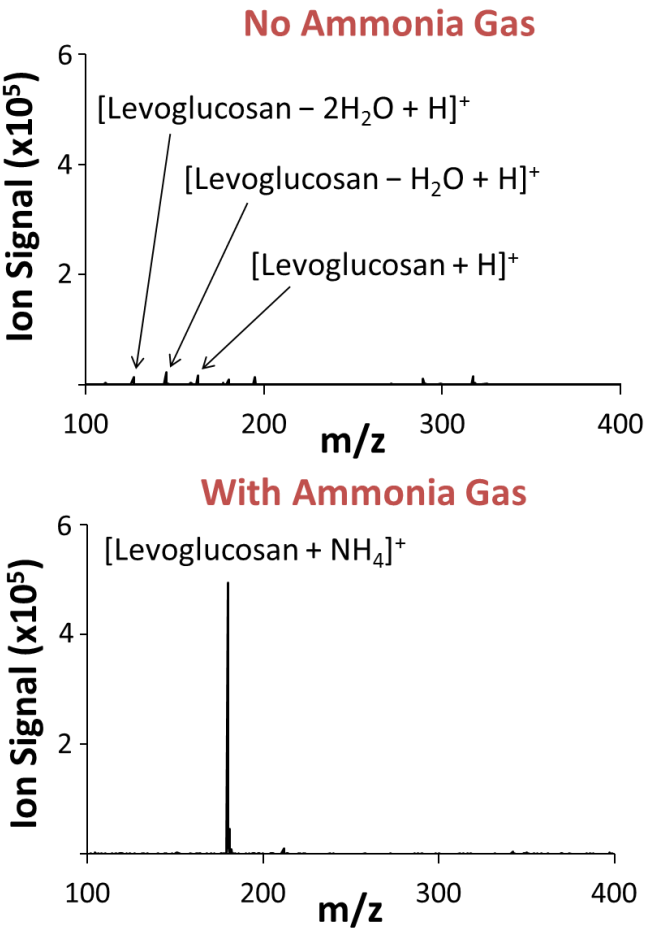

Figure 2. APCI-TOF MS analysis of levoglucosan standard with and without ammonia dopant gas. (*) Represents ammonium and methanol adducts of levoglucosan formed with background gas.

lignin pyrolysis are mostly ionized as a protonated form, and aromatic hydrocarbons are ionized as a radical ion form.

Our newly developed dAPCI method is especially useful when connected to a TOF MS and applied to complex unknown analysis such as in Py-GC-MS. Many of the compounds in Py-GC-MS are not in the database (see next section and Supplemental Table 1) and the information available through conventional GC-EI-MS is very limited. On the other hand, TOF MS combined with dAPCI can softly ionize the compounds with no or minimal fragmentation and

directly determine their chemical compositions. The dAPCI-TOF MS also provides excellent sensitivity (detection limit of ten femtomole level) and dynamic range of up to five orders of magnitude. Lack of structural information and unavailability of database search are the current limitations but the chemical compositions of the pyrolysis or upgraded products provide sufficient information for the purpose of catalytic deoxygenation monitoring, as demonstrated here.

Our ability to directly determine all the chemical compositions leads to the realization that many of the compounds in Supplemental Table 1 are actually structural isomers. For example, we observed five structural isomers of $C_6H_{10}O_5$ and nineteen structural isomers of $C_6H_8O_4$. This is in contrast to only two known structural isomers in Py-GC-EI-MS analysis for both the chemical compositions. For $C_6H_{10}O_5$, 1,6-anhydro-β-D-glucopyranose (levoglucosan) and 1,6-anhydro-β- D-glucofuranose are reported [32]. For $C_6H_8O_4$, 1,5-anhydro-4-deoxy-D-glycerohex-1-en-3-ulose and 1,4;3,6-dianhydro-α-D-glucopyranose (DAGP) are previously reported [31]. It is not surprising many more structural isomers are present than previously reported. When a glycosidic bond is cleaved in cellulose chain, several different structural isomers are possible depending upon where and how the broken bond is re-arranged to form stable compounds. Levoglucosan is most stable and produced in high yield, thus known for a long time, but thermodynamics allows some other structural isomers at high temperature of 500 °C. Although many of them have not been fully characterized due to their low abundances, we could at least confirm their presence after GC separation followed by high-resolution mass spectrometric analysis. In case of $C_6H_8O_4$, many more structural isomers would be possible depending on where water loss occurs in several structural isomers of $C_6H_{10}O_5$, among which we found a total of nineteen isomers.

Py-GC-dAPCI-TOF MS analysis for *in situ* catalytic fast pyrolysis

Py-GC-dAPCI-TOF MS analysis was performed for cellulose pyrolysis with and without catalysts. Figure 3 shows base peak chromatograms (BPCs) for fast pyrolysis of cellulose and catalyst-cellulose mixtures at 5:1 ratio with ZY and ZSM-5. Major peaks are labeled with their corresponding heteroatom classes. Characterization and identification of cellulose pyrolysis products is previously reported, but only for major compounds [27-31]. The most abundant compound in cellulose pyrolysis is levoglucosan ($C_6H_{10}O_5$) having a retention time of 44.4 min, followed by glycolaldehyde ($C_2H_4O_2$) at 5.5 min and 5-hydroxymethylfurfural ($C_6H_6O_3$) at 34.6 min. The overall chromatogram pattern and ion abundances are relatively in good agreement with other reported data [32,33], except that very low mass compounds are missing such as formic acid. Formic acid has *m*/*z* 64 as an ammonium adduct, which is close to the low mass cutoff of the current instrumentation, *m*/*z* 60, and significant mass discrimination is expected. Additionally, very volatile compounds seem to have low efficiency with the current instrumentation.

In situ CFP with zeolite catalysts (Figure 3B and C) show distinct differences compared to the control (Figure 3A). With ZY catalyst (Figure 3B), ion signals for highly oxygenated compounds are decreased (note *y*-scale is ten times different between Figure 3A and B) and converted to various low oxygen compounds, making the chromatogram very complex. In case of ZSM-5 (Figure 3C), highly oxygenated compounds are mostly gone and O_1 and fully deoxygenated hydrocarbon compounds (HC) dominate the chromatogram. This is in good agreement with the previous report that ZSM-5 is very efficient in deoxygenation [12]. This effect is most noticeable through the presence of highly abundant aromatic hydrocarbons (e.g., those peaks at the retention time of 26.9, 30.7, 46.1, and 49.0 min for naphthalene,

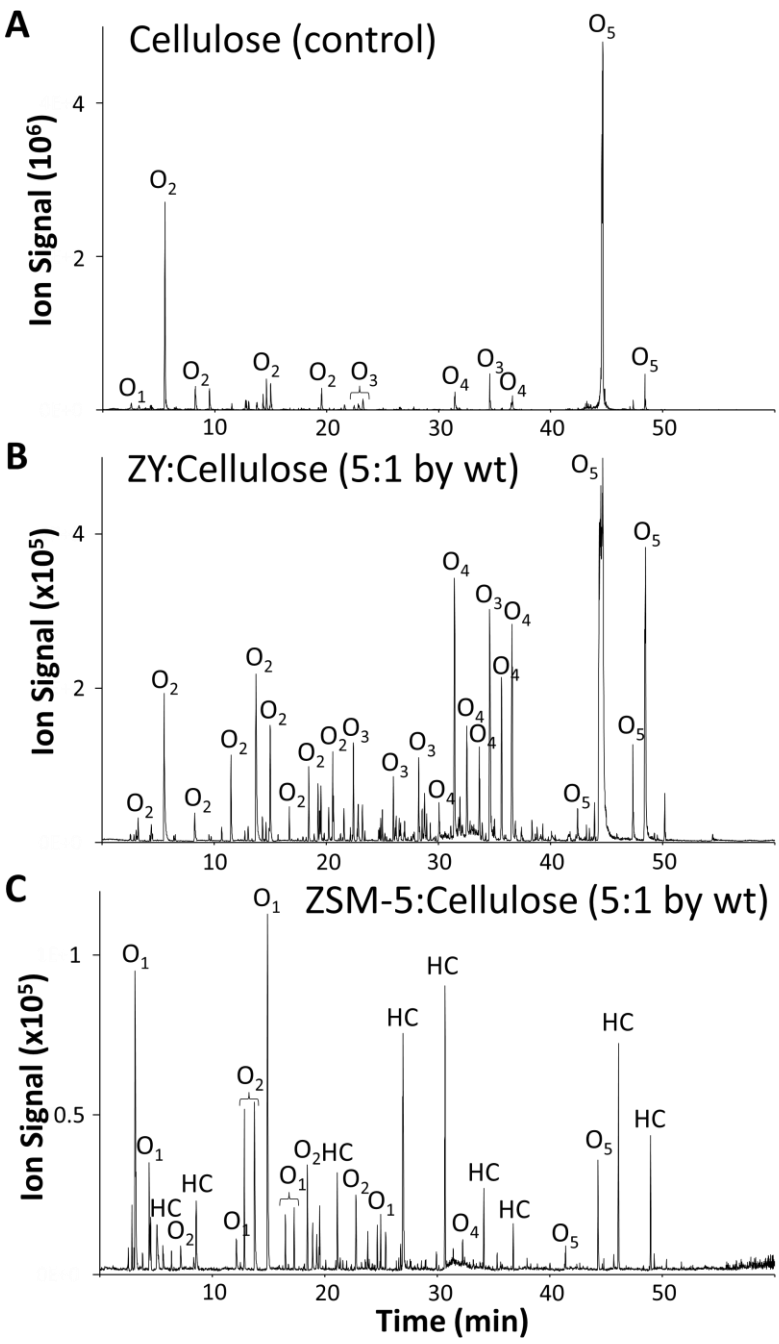

Figure 3. Base peak chromatograms (BPCs) of cellulose pyrolysis (A) without catalyst, and (B) ZY and (C) ZSM-5 catalysts. Heteroatom classes are labeled for major peaks.

methylnaphthalene, anthracene, and methylanthracene, respectively), and the decrease in levoglucosan ion intensity by one hundred times. The difference between ZSM-5 and ZY can be attributed to zeolite pore structure and acidity. ZSM-5 has smaller pores and greater acidity (straight 10 member-ring, 5.4 Å) compared to ZY (circular 12 member-rings, 7.4 Å) [34]. Aho et al. showed high zeolite acidity increased reactivity and generated more water and aromatic hydrocarbons [35]. It should be noted that many of these CFP products are not in the EI−MS NIST database, especially those of low oxygen intermediates, and could not be identified (Table S1), whereas we could determine the chemical compositions of all the peaks, thus, monitoring the change in the number of oxygens of each molecule.

Supplemental Table 1 lists all the chemical compositions of cellulose pyrolysis products obtained using Py-GC-dAPCI-TOF MS. The *in situ* CFP is most complex for 1:1 mixture of ZSM-5:cellulose and also listed in the table. They are compared with the corresponding Py-GC-EI-MS data. In cellulose pyrolysis, a total of 82 chemical compositions are determined in Py-GC-dAPCI-TOF MS, in contrast to only 12 that are identified in Py-GC-EI-MS analysis with minimum score of 750 in the NIST database search. Some assignments are ambiguous as the NIST search gives similar scores for several top matching compounds. Twelve additional compounds with lower matching score could be tentatively assigned, labeled as '*', based on the previous reports for their retention times and molecule masses [32]. In case of *in situ* CFP of 1:1 mixture of ZSM-5:cellulose, a total of 137 chemical compositions could be determined in Py-GC-dAPCI-TOF MS whereas only 24 compounds are identified in Py-GC-EI-MS based on NIST search only, and 31 including additional identifications comparing with the literature. Combined altogether without and with catalyst, 142 chemical compositions were determined in Py-GC-dAPCI-TOF MS, compared to only 38 compounds in in-parallel Py-GC-EI-MS analysis that

includes both NIST database search result and tentative assignments based on the literature. It should be noted that about thirty and fifty peaks could be seen in chromatograms of Py-GC-EI-MS of cellulose pyrolysis without and with catalyst, respectively (see Figure 4); however, many of the EI-MS spectra did not match with the NIST database nor literature data.

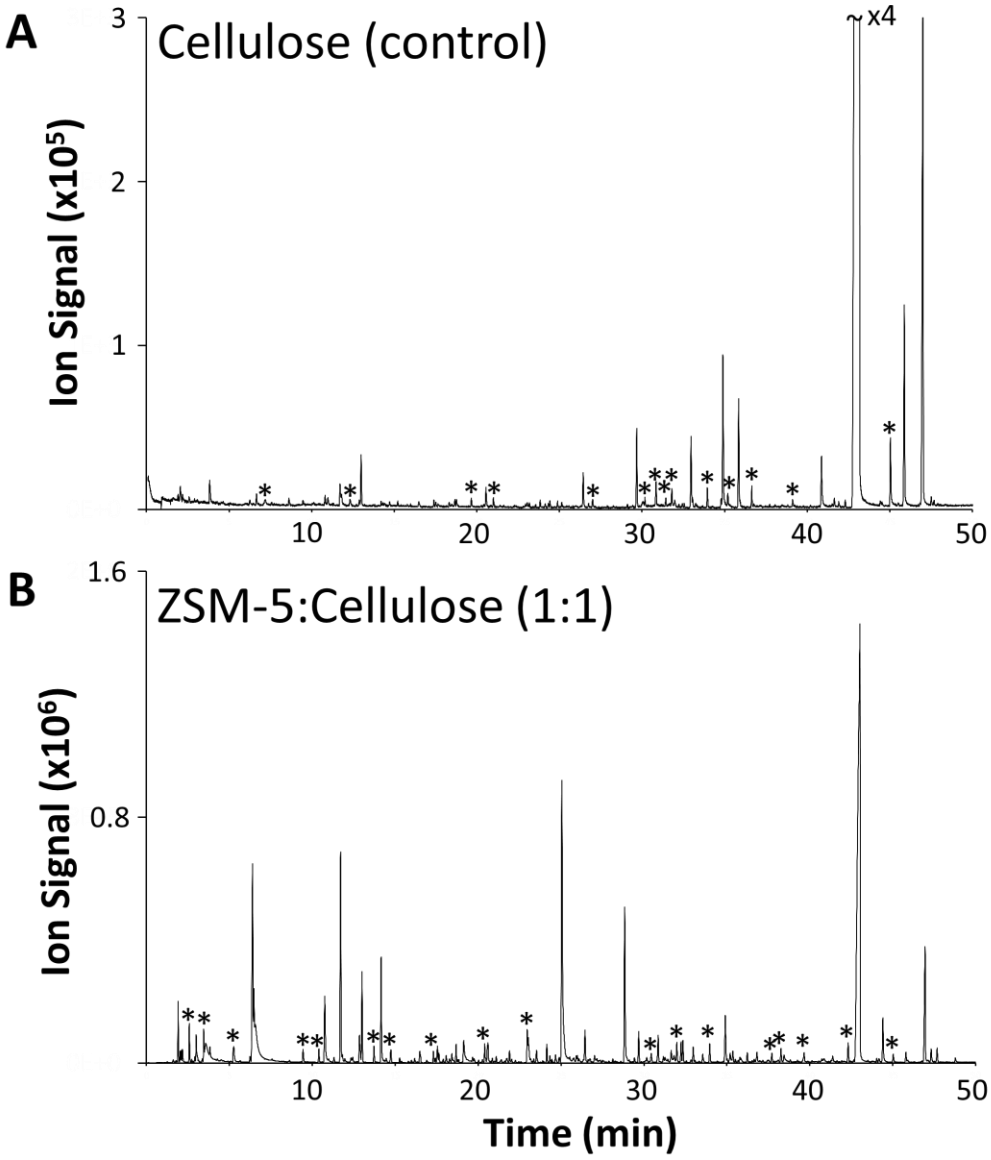

Figure 4. Py-GC-EI-MS base peak chromatograms (BPCs) of cellulose pyrolysis **(A)** without catalyst and **(B)** ZSM-5 catalyst (1:1). (*) Compounds not identified in NIST database search with a minimum score of 750.

Semi-quantitative analysis of CFP products with catalyst-to-cellulose load ratio

We have *qualitatively* demonstrated above how the current instrumentation can be utilized for the monitoring of *in situ* CFP process, especially in comparison of different catalysts. To better understand and optimize the CFP process, however, it is necessary to perform *quantitative* analysis of CFP products. In the current study, *semi-quantitative* analysis was performed by monitoring the relative yields of selected CFP products at catalyst-to-cellulose load ratios of 0, 1, 5, and 10 with ZSM-5. This approach does not allow us to quantitatively compare different molecules because of the difference in ionization efficiencies, but allow us to monitor the quantitative change of each molecule as catalyst load ratio changes.

Figure 5A shows the relative yields of major cellulose pyrolysis products whose yields decrease as the amount of catalyst load increases. For three most abundant ions (levoglucosan, anhydroglucofuranose, and glycolaldehyde), their yields decrease rapidly as catalyst is added. Their yields are less than 50% of the original amount by adding equal weight amount of catalyst and less than 4% and 1% at catalyst load ratio of 5 and 10, respectively. Three other compounds, 1,4;3,6-dianhydro-α-D-glucopyranose (DAGP), $C_6H_8O_4$ at retention time of 36.6 min (a structural isomer of DAGP), and 5-hydroxymethylfurfural (HMF), decrease a little slow with the equal amount of catalyst, 55–70% of the original amount, but eventually disappear at higher catalyst load ratio. It may suggest that apparent deoxygenation of these compounds is relatively slower initially because they are also catalytically being produced from levoglucosan or anhydroglucofuranose through one or two water loss(es).

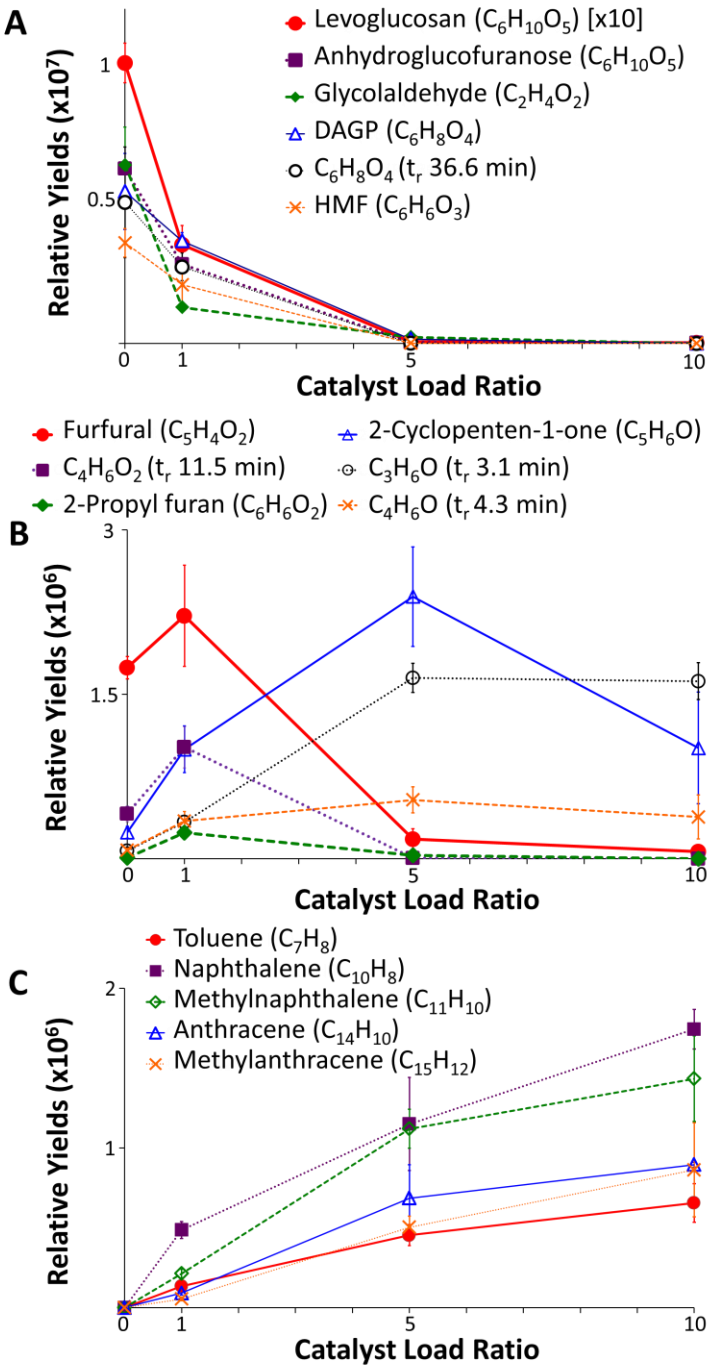

Figure 5. Relative yields of cellulose pyrolysis products as catalyst load ratio increased by weight. **(A)** Most abundant compounds in control, **(B)** partially deoxygenated compounds, and **(C)** fully deoxygenated compounds. Relative yields were calculated by integrating the area of each extracted ion chromatogram and normalizing to correspond to CFP of 100 µg cellulose. Error bars are standard deviation obtained from three replicates. Abbreviations: DAGP, 1,4;3,6-dianhydro-α-D-glucopyranose; HMF, 5-hydroxymethylfurfural.

Deoxygenation behavior of major low oxygen compounds is shown in Figure 5B as the change in catalyst load ratio. Their yields increase by adding catalyst, but are eventually disappearing with high amount of catalyst except for C_3H_6O at retention time of 3.1 min and C_4H_6O at 4.3 min whose amounts are not decreasing any further at the catalyst load ratio of 10 compared to those at 5. These low oxygen compounds are most likely produced as partial deoxygenation/cracking of high oxygen compounds as CFP proceeds. Some of them might be further converted to fully deoxygenated compounds via CFP and some others might escape the reactor without further reaction. Those eventually disappearing at high catalyst load ratio would be the intermediate compounds of full CFP process.

A similar trend was observed by Mukarakate et al. in their monitoring of the deactivation of ZSM-5 during *ex situ* CFP of biomass pyrolysis using a molecular beam mass spectrometer (MBMS) [36]. As they passed more pyrolysis vapors through catalytic bed, the amount of fully deoxygenated compounds is decreased, dominated by partially deoxygenated compounds, and eventually dominated by unreacted compounds at high biomass-to-catalyst ratio (or low catalytic load ratio). In their data, intermediate compounds are most abundant when catalytic load ratio is 0.5 to 2, somewhat similar to ours. An important advantage of our approach is that we can trace the trend of individual molecular compounds as the catalyst load ratio changes. Additionally, we can directly determine the chemical compositions of each compound. Their spectrum for intermediate compounds in *ex situ* CFP of cellulose (Figure S1 of Mukarakate et al. [36]) is extracted from a series of MBMS spectra through principal component analysis and most abundant molecular peaks include *m*/*z* 82, 96, and 110. By comparing with our data and considering EI−MS produces molecular radical ions ($M^{+\bullet}$), these compounds correspond to C_5H_6O (2-cyclopenten-1-one), $C_5H_4O_2$ (furfural), and $C_6H_6O_2$ (2-propyl furan) shown in Figure

5B, suggesting good correlation between our and Mukarakate's data despite the differences in instrumentation and experimental conditions.

Completely deoxygenated hydrocarbon compounds, such as the five aromatic hydrocarbons shown in Figure 5C, follow the opposite trend with major cellulose pyrolysis products shown in Figure 5A. None of these compounds (or other hydrocarbons) were observed without catalyst. Aromatic hydrocarbons are produced from cracking, dehydration, deoxygenation, and reformation reactions, most notably Diels-Alder reactions, as noted elsewhere [7]. All hydrocarbons steadily increase in abundance at higher catalyst load. Even at the highest catalyst load ratio of 10, their amounts are increased by 58–78% from those at the load ratio of 5. The high yield of polyaromatic hydrocarbons (PAHs), e.g., naphthalene or anthracene, suggests significant coke formation occurs in catalytic fast pyrolysis, which is currently a well-known obstacle in CFP without hydrogen addition. Effective hydrogen to carbon ratio, $(H/C)_{eff}$, is suggested as an important parameter in catalytic fast pyrolysis, defined as $(H - 2O)/C$ with H, C, and O as the moles of hydrogen, carbon, and oxygen, respectively [37]. Cellulose has $(H/C)_{eff}$ of zero, meaning complete dehydration will lead to complete coke or char formation. In fact, the low deoxygenation efficiency at low catalyst load is a result of catalyst deactivation by coke formation [36].

Conclusion

A critical bottleneck in studying CFP process is the fact that many CFP products cannot be characterized due to significant fragmentations in EI-MS and/or their absence in the database. We developed a new Py-GC-MS approach using dopant-assisted APCI and high-resolution TOF MS analysis. This approach was utilized to efficiently ionize CFP products without or with

minimal fragmentations and directly determine their chemical compositions. A total of 142 chemical compositions were identified with this approach for the CFP of cellulose whereas only 38 of them could be identified by in-parallel Py-GC-EI-MS analysis. The utility of our approach was demonstrated to compare catalytic deoxygenation efficiencies of two different catalysts. Furthermore, semi-quantitative analysis was performed to reveal the changes of relative yields of each CFP product as the catalyst-to-biomass load ratio increase.

The current study is limited to semi-quantitative analysis but quantitative analysis would be necessary for the comprehensive understanding of CFP process. For this purpose, we are currently developing a tandem detection system with flame ionization detector (FID) by splitting the GC capillary outlet between FID and dAPCI-TOF MS. FID signal is proportional to carbon concentration and quantitative in contrast to mass spectrometric ion signals, which have strong dependence on ionization efficiency of each molecule. Once successful, we should be able to obtain both qualitative and quantitative information simultaneously through dAPCI-TOF MS and FID, respectively.

Acknowledgment

DPC is partially supported by NSF EpSCOR seed grant.

References

[1] Bridgwater, A.V. *Biomass Bioenergy* **2012**, 38, 68–94.

[2] DOE, *Conversion Technologies for Advanced Biofuels: Preliminary Roadmap & Workshop Report*, Arlington, VA, **2011**.

[3] Talmadge, M.S.; Baldwin, R.M.; Biddy, M.J.; McCormick, R.L.; Beckham, G.T.; Ferguson, G.A.; Czernik, S.; Magrini-Bair, K.A.; Foust, T.D.; Metelski, P.D.; Hetrick, C.; Nimlos, M.R. *Green Chem*. **2014**, 16, 407–453.

[4] Mettler, M.S.; Paulsen, A.D.; Vlachos, D.G.; Dauenhauer, P.J. *Energy Environ*. *Sci*. **2012**, 5, 7864–7898.

[5] Ibanez, M.; Valle, B.; Bilbao, J.; Gayubo, A.G.; Castano, P. *Catal*. *Today* **2012**, 195, 106–113.

[6] Ruddy, D.A.; Schaidle, J.A.; Ferrell, J.R.; Wang, J.; Moens, L.; Hensley, J.E. *Green Chem*. **2014**, 16, 454–490.

[7] Cheng, Y.-T.; Huber, G.W. *Green Chem*. **2012**, 14, 3114–3125.

[8] Fanchiang, W.-L.; Lin, Y.-C. *Appl*. *Catal*. *A-Gen*. **2012**, 419, 102–110.

[9] Gunawardena, D.A.; Fernando, S.D. *Chem*. *Eng*. *Technol*. **2011**, 34, 173–178.

[10] Liu, W.; Hu, C.; Yang, Y.; Tong, D.; Li, G.; Zhu, L. *Energy Convers*. *Manage*. **2010**, 51, 1025–1032.

[11] Valle, B.; Gayubo, A.G.; Alonso, A.; Aguayo, A.T.; Bilbao, J. *Appl*. *Catal*. *B-Environ*. 2010, 100, 318–327.

[12] Foster, A.J.; Jae, J.; Cheng, Y.-T.; Huber, G.W.; Lobo, R.F. *Appl*. *Catal*. *A-Gen*. **2012**, 423, 154–161.

[13] Thangalazhy-Gopakumar, S.; Adhikari, S.; Chattanathan, S.A.; Gupta, R.B. *Bioresour*. *Technol*. **2012**, 118, 150–157.

[14] Čajka, T.; Hajšlová, J.; Kazda, R.; Poustka, J. *J*. *Sep*. *Sci*. **2005**, 28, 601–611.

[15] Hejazi, L.; Ebrahimi, D.; Hibbert, D.B.; Guilhaus, M. *Rapid Commun*. *Mass Spectrom*. **2009**, 23, 2181–2189.

[16] Li, J.; Cai, J.; Yuan, T.; Guo, H.; Qi, F. *Rapid Commun*. *Mass Spectrom*. **2009**, 23, 1269–1274.

[17] Pan, Y.; Zhang, T.; Hong, X.; Zhang, Y.; Sheng, L.; Qi, F. *Rapid Commun. Mass Spectrom.* **2008**, 22, 1619–1623.

[18] Pan, Y.; Zhang, L.; Zhang, T.; Guo, H.; Hong, X.; Qi, F. *J. Mass Spectrom.* **2008**, 43, 1701–1710.

[19] Mukarakate, C.; Scheer, A.M.; Robichaud, D.J.; Jarvis, M.W.; David, D.E.; Ellison, G.B.; Nimlos, M.R.; Davis, M.F. *Rev. Sci. Instrum.* **2011**, 82, 0331004.

[20] Carrasco-Pancorbo, A.; Nevedomskaya, E.; Arthen-Engeland, T.; Zey, T.; Zurek, G.; Baessmann, C.; Deelder, A.M.; Mayboroda, O.A. *Anal. Chem.* **2009**, 81, 10071–10079.

[21] Bristow, T.; Harrison, M.; Sims, M. *Rapid Commun. Mass Spectrom.* **2010**, 24, 1673–1681.

[22] Garcia-Villalba, R.; Pacchiarotta, T.; Carrasco-Pancorbo, A.; Segura-Carretero, A.; Fernandez-Gutierrez, A.; Deelder, A.M.; Mayboroda, O.A. *J. Chromatogr. A* **2011**, 1218, 959–971.

[23] Desmazieres, B.; Buchmann, W.; Terrier, P.; Tortajada, J. *Anal. Chem.* **2008**, 80, 783–792.

[24] Arthen-Engeland, T.; Dunsbach, R. *LC GC Eur.* **2008**, 21, 34–35.

[25] Song, L.; Cho, D.S.; Bhandari, D.; Gibson, S.C.; McNally, M.E.; Hoffman, R.M.; Cook, K.D. *Int. J. Mass Spectrom.* **2011**, 303, 173–180.

[26] Amad, M.A.; Sioud, S. *Rapid Commun. Mass Spectrom.* **2012**, 26, 2517–2525.

[27] Banyasz, J.L.; Li, S.; Lyons-Hart, J.; Shafer, K.H. *Fuel* **2001**, 80, 1757–1763.

[28] Brown, A.L.; Dayton, D.C.; Daily, J.W. *Energy Fuels* **2001**, 15, 1286–1294.

[29] Huang, J.; Liu, C.; Wei, S. *Acta Chim. Sinica* **2009**, 67, 2081–2086.

[30] Lanza, R.; Nogare, D.D.; Canu, P. *Ind. Eng. Chem. Res.* **2009**, 48, 1391–1399.

[31] Mettler, M.S.; Mushrif, S.H.; Paulsen, A.D.; Javadekar, A.D.; Vlachos, D.G.; Dauenhauer, P.J. *Energy Environ. Sci.* **2012**, 5, 5414–5424.

[32] Patwardhan, P.R.; Satrio, J.A.; Brown, R.C.; Shanks, B.H. *J. Anal. Appl. Pyrolysis* **2009**, 86, 323–330.

[33] Mettler, M.S.; Paulsen, A.D.; Vlachos, D.G.; Dauenhauer, P.J. *Green Chem.* **2012**, 14, 1284–1288.

[34] Aho, A.; Kumar, N.; Eränen, K.; Salmi, T.; Hupa, M.; Murzin, D.Y. *Fuel* **2008**, 87, 2493–2501.

[35] Aho, A.; Kaldstrom, M.; Fardim, P.; Kumar, N.; Eranen, K.; Salmi, T.; Holmbon, B.; Hupa, M.; Murzin, D.Y. *Cellul. Chem. Technol.* **2010**, 44, 89–95.

[36] Mukarakate, C.; Zhang, X.; Stanton, A.R.; Robichaud, D.J.; Ciesielski, P.N.; Malhotra, K.; Donohoe, B.S.; Gjersing, E.; Evans, R.J.; Heroux, D.S.; Richards, R.; Iisa, K.; Nimlos, M.R. *Green Chem.* **2014**, 16, 1444–1461.

[37] Chen, N.Y.; Degnan, T.F.; Koenig, L.R. *Chemtech.* **1986**, 16, 506–511.

Supplemental Table 1. Cellulose pyrolysis products observed with and without catalyst (ZSM-5; 1:1 by wt) by Py-GC-APCI-TOF MS and Py-GC-EI-MS. Identifications for Py-GC-EI-MS data are based on the spectral library search against NIST database with a minimum NIST score of 750. Acronyms: ADGH, 1,5-anhydro-4-deoxy-D-glycero-hex-1-en-3-ulose; DAGP, 1,4;3,6-dianhydro-α-D-glucopyranose; HMF, 5-hydroxymethylfurfural

*Compounds with matching score less than 750, but tentatively assigned based on cross-reference to previous literature by retention time and molecular ion mass [a,b].

†Anhydrohexose compounds with score greater than 750 but with exactly same EI-MS spectral pattern to each other and cannot distinguish structural isomers.

		PyGC-APCI-TOF MS							PyGC-EI-MS		
No.	t_r (min)	m/z experimental	Formula	Adduct	m/z theoretical	Error (ppm)	Control	1:1	Assignment	Control	1:1
1	2.48	62.0602	C2 H4 O	NH4	62.0600	3.2		Y			
2	2.81	68.0261	C4 H4 O		68.0262	1.5		Y	Furan*	Y	Y
3	3.01	74.0606	C3 H4 O	NH4	74.0600	7.4	Y	Y			
4	3.14	76.0762	C3 H6 O	NH4	76.0757	6.6	Y	Y			
5	3.19	90.0549	C3 H4 O2	NH4	90.0550	0.8	Y	Y	Methylglyoxal*	Y	
6	3.76	82.0415	C5 H6 O		82.0413	2.9		Y	2-Methyl furan*	Y	Y
7	4.33	88.0754	C4 H6 O	NH4	88.0757	3.6		Y			
8	4.45	104.0697	C4 H6 O2	NH4	104.0706	9.1	Y	Y			
9	5.51	78.0554	C2 H4 O2	NH4	78.0550	5.7	Y	Y	Glycolaldehyde*	Y	Y
10	6.40	88.0757	C4 H6 O	NH4	88.0757	0.2	Y	Y			
11	6.55	88.0757	C4 H6 O	NH4	88.0757	0.2	Y	Y			
12	6.98	116.0695	C5 H6 O2	NH4	116.0706	9.5		Y			
13	7.11	78.0554	C2 H4 O2	NH4	78.0550	5.7		Y	Acetic acid*	Y	
14	7.65	118.0852	C5 H8 O2	NH4	118.0863	9.4		Y			
15	8.23	92.0702	C3 H6 O2	NH4	92.0706	4.6	Y	Y	Acetol*	Y	Y
16	8.60	92.0617	C7 H8		92.0621	4.6		Y	Toluene		Y
17	9.55	106.0489	C3 H4 O3	NH4	106.0499	9.4	Y	Y			
18	9.66	100.0752	C5 H6 O	NH4	100.0757	5.4		Y			
19	9.73	104.0701	C4 H6 O2	NH4	104.0706	5.2		Y			
20	10.68	100.0752	C5 H6 O	NH4	100.0757	5.4	Y	Y	2-Methylfuran*	Y	

21	11.50	104.0701	C4 H6 O2	NH4	104.0706	5.2	Y	Y					
22	12.12	102.0542	C4 H4 O2	NH4	102.0550	7.8		Y					
23	12.38	80.0710	C2 H6 O2	NH4	80.0706	4.9	Y						
24	12.73	120.0645	C4 H6 O3	NH4	120.0655	8.1	Y	Y					
25	12.82	108.0196	C6 H4 O2		108.0206	8.9		Y					
26	12.85	106.0768	C8 H10		106.0777	8.4		Y	p-Xylene			Y	
27	13.03	102.0542	C4 H4 O2	NH4	102.0550	7.8	Y	Y					
28	13.37	98.0354	C5 H6 O2		98.0362	8.1		Y					
29	13.77	102.0542	C4 H4 O2	NH4	102.0550	7.8	Y	Y					
30	14.00	120.0645	C4 H6 O3	NH4	120.0655	8.1	Y						
31	14.32	104.0701	C4 H6 O2	NH4	104.0706	5.2	Y	Y					
32	14.45	116.0695	C5 H6 O2	NH4	116.0706	9.5		Y					
33	14.63	120.0645	C4 H6 O3	NH4	120.0655	8.1	Y	Y					
34	14.88	100.0752	C5 H6 O	NH4	100.0757	5.4	Y	Y					
35	15.00	114.0540	C5 H4 O2	NH4	114.0550	8.9	Y	Y	Furfural		Y	Y	
36	15.70	128.0694	C6 H6 O2	NH4	128.0706	9.2		Y	2-propyl Furan*			Y	
37	16.49	112.0747	C6 H6 O	NH4	112.0757	8.5		Y					
38	16.69	116.0697	C5 H6 O2	NH4	116.0706	7.4	Y	Y	2-Furanmethanol*		Y	Y	
39	16.92	116.0697	C5 H6 O2	NH4	116.0706	7.4	Y	Y	3-Furanmethanol*		Y		
40	17.27	114.0902	C6 H8 O	NH4	114.0913	9.7		Y					
41	17.45	118.0855	C5 H8 O2	NH4	118.0863	6.9	Y	Y					
42	17.94	128.0694	C6 H6 O2	NH4	128.0706	9.2		Y					
43	18.19	116.0695	C5 H6 O2	NH4	116.0706	9.5		Y					
44	18.29	128.0694	C6 H6 O2	NH4	128.0706	9.2		Y					
45	18.45	114.0540	C5 H4 O2	NH4	114.0550	8.9	Y	Y	4-Cyclopentene-1,3-dione			Y	
46	18.90	114.0903	C6 H8 O	NH4	114.0913	8.8		Y					
47	19.24	99.0433	C5 H6 O2	H	99.0441	7.7		Y	2(3H)-Furanone, dihydro-3-methylene-			Y	
48	19.29	120.0645	C4 H6 O3	NH4	120.0655	8.1	Y	Y					
49	19.44	108.0644	C3 H6 O3	NH4	108.0655	9.7	Y	Y					
50	19.52	116.0695	C5 H6 O2	NH4	116.0706	9.1	Y	Y					
51	19.70	116.0695	C5 H6 O2	NH4	116.0706	9.1		Y	2-Cyclopenten-1-one, 2-hydroxy-			Y	
52	19.82	127.0381	C6 H6 O3	H	127.0390	7.2		Y					

53	20.11	102.0542	C4 H4 O2	NH4	102.0550	7.8	Y					
54	20.22	116.0697	C5 H6 O2	NH4	116.0706	7.4	Y	Y				
55	20.45	111.0431	C6 H6 O2	H	111.0441	8.9		Y				
56	20.57	111.0431	C6 H6 O2	H	111.0441	8.9	Y	Y	2-Furancarboxaldehyde, 5-methyl-	Y	Y	
57	20.64	132.0644	C5 H6 O3	NH4	132.0655	8.2	Y	Y				
58	21.07	97.0640	C6 H8 O	H	97.0648	8.3		Y				
59	21.12	116.0611	C9 H8		116.0621	8.3		Y	Indene		Y	
60	21.27	104.0701	C4 H6 O2	NH4	104.0706	5.2	Y	Y				
61	21.45	128.0694	C6 H6 O2	NH4	128.0706	9.2		Y				
62	21.57	102.0543	C4 H4 O2	NH4	102.0550	6.8	Y	Y	2(5H)-Furanone*	Y	Y	
63	21.92	111.0431	C6 H6 O2	H	111.0441	8.9		Y				
64	22.14	116.0697	C5 H6 O2	NH4	116.0706	7.4	Y	Y				
65	22.32	146.0799	C6 H8 O3	NH4	146.0812	8.6	Y	Y				
66	22.44	132.0645	C5 H6 O3	NH4	132.0655	7.5	Y	Y				
67	22.74	114.0540	C5 H4 O2	NH4	114.0550	8.9	Y	Y				
68	22.84	108.0646	C3 H6 O3	NH4	108.0655	7.9	Y	Y				
69	23.22	113.0225	C5 H4 O3	H	113.0233	7.5	Y	Y				
70	23.44	144.0644	C6 H6 O3	NH4	144.0655	7.7		Y				
71	24.11	128.0694	C6 H6 O2	NH4	128.0706	9.2		Y				
72	24.21	128.0694	C6 H6 O2	NH4	128.0706	9.2		Y				
73	24.74	104.0698	C4 H6 O2	NH4	104.0706	8.1	Y	Y				
74	24.86	162.0756	C6 H8 O4	NH4	162.0761	3.0		Y				
75	25.01	129.0533	C6 H8 O3	H	129.0546	9.8	Y	Y				
76	25.19	162.0756	C6 H8 O4	NH4	162.0761	3.0		Y				
77	25.22	132.0645	C5 H6 O3	NH4	132.0655	7.5	Y	Y				
78	25.34	162.0756	C6 H8 O4	NH4	162.0761	3.0		Y				
79	25.68	146.0799	C6 H8 O3	NH4	146.0812	8.6	Y	Y	1,6:2,3-Dianhydro-4-deoxy-β-D-ribo-hexopyranose	Y		
80	25.99	144.0644	C6 H6 O3	NH4	144.0655	7.7	Y	Y				
81	26.14	144.0644	C6 H6 O3	NH4	144.0655	7.7		Y				
82	26.22	162.0756	C6 H8 O4	NH4	162.0761	3.0		Y				
83	26.26	146.0799	C6 H8 O3	NH4	146.0812	8.6	Y					
84	26.49	127.0379	C6 H6 O3	H	127.0390	8.7	Y	Y				

85	26.54	111.0431	C6 H6 O2	H	111.0441	8.9		Y				
86	26.64	120.0643	C4 H6 O3	NH4	120.0655	9.7	Y	Y				
87	26.65	134.0799	C5 H8 O3	NH4	134.0812	9.7	Y	Y				
88	26.72	148.0595	C5 H6 O4	NH4	148.0604	6.2	Y	Y				
89	26.92	128.0609	C10 H8		128.0621	9.2		Y	Naphthalene		Y	
90	26.94	142.0487	C6 H4 O3	NH4	142.0499	8.1	Y					
91	27.01	162.0756	C6 H8 O4	NH4	162.0761	3.0		Y				
92	27.16	144.0641	C6 H6 O3	NH4	144.0655	9.8		Y				
93	27.27	116.0697	C5 H6 O2	NH4	116.0706	7.4	Y	Y				
94	27.56	127.0378	C6 H6 O3	H	127.0390	9.5		Y				
95	27.61	128.0694	C6 H6 O2	NH4	128.0706	9.2		Y				
96	27.74	134.0799	C5 H8 O3	NH4	134.0812	9.7	Y	Y				
97	27.86	116.0697	C5 H6 O2	NH4	116.0706	7.4		Y				
98	28.24	144.0646	C6 H6 O3	NH4	144.0655	6.3	Y	Y	Levoglucosenone	Y	Y	
99	28.33	132.0645	C5 H6 O3	NH4	132.0655	7.5		Y				
100	28.56	150.0754	C5 H8 O4	NH4	150.0761	4.4	Y	Y				
101	28.66	134.0802	C5 H8 O3	NH4	134.0812	7.7	Y	Y				
102	28.78	150.0754	C5 H8 O4	NH4	150.0761	4.4	Y	Y				
103	28.96	143.0330	C6 H6 O4	H	143.0339	6.5	Y	Y				
104	29.28	162.0772	C6 H8 O4	NH4	162.0761	6.9		Y				
105	29.64	144.0646	C6 H6 O3	NH4	144.0655	6.3	Y	Y				
106	30.09	162.0756	C6 H8 O4	NH4	162.0761	3.0	Y	Y				
107	30.59	162.0756	C6 H8 O4	NH4	162.0761	3.0	Y	Y				
108	30.69	142.0769	C11 H10		142.0777	5.3		Y	Methylnaphthalene		Y	
109	31.13	162.0756	C6 H8 O4	NH4	162.0761	3.0	Y	Y	ADGH*	Y		
110	31.43	162.0756	C6 H8 O4	NH4	162.0761	3.0	Y	Y	DAGP	Y	Y	
111	31.66	132.0645	C5 H6 O3	NH4	132.0655	7.5	Y	Y				
112	31.81	162.0756	C6 H8 O4	NH4	162.0761	3.0	Y	Y				
113	31.94	162.0756	C6 H8 O4	NH4	162.0761	3.0	Y	Y				
114	32.56	162.0756	C6 H8 O4	NH4	162.0761	3.0	Y	Y				
115	33.68	162.0756	C6 H8 O4	NH4	162.0761	3.0	Y	Y				
116	33.93	162.0756	C6 H8 O4	NH4	162.0761	3.0	Y	Y				
117	34.15	156.0926	C12 H12		156.0926	0.1		Y	Dimethylnaphthalene		Y	

118	34.60	144.0655	C6 H6 O3	NH4	144.0655	0.0	Y	Y	HMF	Y	Y	
119	34.71	162.0756	C6 H8 O4	NH4	162.0761	3.0	Y	Y				
120	34.91	134.0802	C5 H8 O3	NH4	134.0812	7.7	Y	Y				
121	35.00	144.0649	C6 H6 O3	NH4	144.0655	4.2	Y	Y				
122	35.33	154.0766	C12 H10		154.0777	6.9		Y	Naphthalene, 2-ethenyl-		Y	
123	35.65	162.0756	C6 H8 O4	NH4	162.0761	3.0	Y	Y	Anhydrohexose†	Y		
124	36.61	162.0756	C6 H8 O4	NH4	162.0761	3.0	Y	Y	Anhydrohexose†	Y	Y	
125	36.88	180.0868	C6 H10 O5	NH4	180.0866	1.3	Y	Y				
126	37.43	150.0754	C5 H8 O4	NH4	150.0761	4.4	Y	Y				
127	38.21	149.0587	C9 H8 O2	H	149.0597	6.6		Y				
128	38.36	162.0756	C6 H8 O4	NH4	162.0761	3.0		Y				
129	38.83	178.0710	C6 H8 O5	NH4	178.0710	0.0	Y	Y				
130	39.31	204.0883	C8 H10 O5	NH4	204.0866	8.4		Y				
131	42.43	180.0870	C6 H10 O5	NH4	180.0866	2.5	Y	Y	3,4-Anhydrohexopyranose	Y	Y	
132	43.22	208.0834	C7 H10 O6	NH4	208.0816	8.6		Y				
133	43.48	208.0834	C7 H10 O6	NH4	208.0816	8.6		Y				
134	44.38	180.0870	C6 H10 O5	NH4	180.0866	2.5	Y	Y	Levoglucosan	Y	Y	
135	46.12	179.0849	C14 H10	H	179.0855	3.2		Y	Anthracene		Y	
136	47.07	222.0991	C8 H12 O6	NH4	222.0972	8.7	Y	Y				
137	47.44	180.0870	C6 H10 O5	NH4	180.0866	2.5	Y	Y	Anhydrogalactopyranose	Y	Y	
138	48.59	180.0870	C6 H10 O5	NH4	180.0866	2.5	Y	Y	Anhydroglucofuranose	Y	Y	
139	48.97	193.1017	C15 H12	H	193.1012	2.3		Y	9-Methylanthrancene		Y	
140	49.27	210.0780	C10 H8 O4	NH4	210.0761	9.3		Y				
141	49.29	193.1017	C15 H12	H	193.1012	2.3		Y	2-Methylanthrancene		Y	
142	50.39	204.0941	C16 H12		204.0934	3.5		Y	Naphthalene, 2-phenyl-		Y	

[a] P.R. Patwardhan, J.A. Satrio, R.C. Brown and B.H. Shanks, *Journal of Analytical and Applied Pyrolysis*, 86, (2009) 323.

[b] M.S. Mettler, S.H. Mushrif, A.D. Paulsen, A.D. Javadekar, D.G. Vlachos and P.J. Dauenhauer, *Energy & Environmental Science*, 5, (2012) 5414.

CHAPTER V

REAL-TIME MONITORING OF MOLECULAR PRODUCTS FROM THIN-FILM PYROLYSIS OF GLUCOSE-BASED CARBOHYDRATES USING HIGH RESOLUTION MASS SPECTROMETRY

A manuscript to be submitted to *Energy & Environmental Science*

D. Paul Cole, Erica A. Dalluge, Carolyn Hutchinson, and Young Jin Lee

Abstract

Fast pyrolysis of biomass offers a promising strategy for converting lignocellulosic material into an energy-dense liquid product that can be upgraded using existing infrastructure to produce biofuels and/or other useful chemicals. Increasing the quality of bio-oil prior to downstream refinement is vital for economic viability, and despite decades of research, only rudimentary knowledge has been gained towards unraveling the complex network of reactions. A substantial bottleneck has been the lack of instrumentation that can provide time-resolved information for chemical kinetics and reaction mechanisms. In this work, we developed micropyrolysis coupled with soft ionization high resolution mass spectrometry to monitor fast pyrolysis products in real-time with sub-second temporal resolution. Critical developments included removal of mass transport effects and perform time calibration. Thin-film pyrolysis technique was used to study glucose and glucose-based carbohydrates under isothermal, kinetically-limited conditions. Our strategy utilizes product evolution profiles and semi-quantitative data for molecular level insights. The current study provides a strong foundation in an effort to improve fundamental understanding and develop detailed mechanisms for pyrolysis chemistry.

Introduction

Production of renewable and sustainable energy for the transportation sector remains a critical challenge due to the limited supply of petroleum. A promising strategy is biomass pyrolysis to generate a transportable carbon-based liquid product [1]. The liquid product, called bio-oil due to its physical resemblance of petroleum crude oil, is condensed vapor produced in highest yield via fast pyrolysis, which thermally degrades lignocellulosic material in the absence of oxygen at high temperatures (~500 °C) and short hot vapor residence times (~1 s) [1-4]. Bio-oil differs chemically from petroleum oils due to high oxygen content (up to 50% by wt.) arising from the chemical composition of biomass that causes stability, corrosion, viscosity, and other issues [3,4]. Thus, bio-oils require further upgrading and refining through various means (cf. hydrotreating and catalytic vapor cracking) to produce fuel and chemicals, which form prohibitive barriers due to additional pressure requirements, catalytic deactivation, and cost [5-8].

The thermochemical conversion of biomass generates products in all three phases (i.e., biochar, bio-oil, and syngas) that contain hundreds of unique molecular species formed through a network of elementary reactions [5]. Previous work by our group characterized volatile and non-volatile molecular species in bio-oil fractions or adsorbed on biochar using high resolution mass spectrometry (HRMS) [9-12]. However, the evolution of pyrolysis species in the condensed-phase prior to forming these end-products is a daunting task, and studies have produced mixed results and simplistic models because of the complexity of the system [13-19]. Initial models and kinetics for cellulose pyrolysis were lumped, condition-specific as represented by the Broido-Shafizadeh model that categorized pyrolysis products by phase (solid, liquid, gas, and sometimes "active cellulose"), rather than by molecular species [20]. Detailed understanding of molecular-

level chemistry underlying the pyrolysis process will improve optimization of reactor designs and conditions that will yield higher quality bio-oil and thus provide more efficient and cost-effective upgrading that are crucial for its commercialization [21].

Unraveling the complexity of pyrolysis chemistry for detailed molecular mechanisms and kinetics has been rigorously investigated in the past few years through combining experimental and computational data. Vinu and Broadbelt developed the first mechanistic model for cellulose fast pyrolysis through carefully dissecting the process into individual reaction steps [22]. More recently, Broadbelt and co-workers have improved the predictive power of their previous model by investigating fast pyrolysis of glucose-based carbohydrates and using computational calculations to solve the mechanistic model [23,24]. The foundation for their modeling was built on experimental results and computational calculations from numerous sources [25-40]. For example, Mayes et al. demonstrated the use of density functional theory (DFT) calculations to describe a reaction pathway of glucose conversion to 5-hydroxymethylfurfural (HMF) through a D-fructose intermediate that has a lower activation energy (E_a) compared to those already known [40]. However, the mechanistic models ignore many dynamic parameters that could affect final product distribution such as heating rate, phase transitions, mass transport, aerosol formation/ejection, and nonvolatile species. These models also utilize Arrhenius parameters that are ambiguously deduced from quantum chemical calculations. Furthermore, experimental product yields are obtained using relatively large sample loads that ignore the effects of sample dimensions.

Dauenhauer and co-workers have demonstrated the importance of sample dimensions for isothermal heating and kinetically-limited conditions during fast pyrolysis [41,42]. They developed a thin-film technique which revealed changes in product yields for cellulose pyrolysis

based on sample thickness and temperature. Micrometer-scale thick (3 μm) thin-film and powder pyrolysis of cellulose with similar sample loading weights had significantly different yields for some compounds. Specifically, levoglucosan yield from thin-film cellulose dropped dramatically to 27% (in percent of initial carbon) compared to 48% obtained from powder cellulose. Light oxygenate compounds such as glycolaldehyde, methylglyoxal, and formic acid increased in yield compared to powder form. Their results showed micrometer-scale thin-films accomplish two critical tasks: (1) volatile components can rapidly diffuse (< 1 ms) through any reactive liquid intermediate thereby preventing possible secondary reactions and (2) extreme heating rates, calculated to be greater than 1,000,000 °C min^{-1} for 3 μm thick cellulose thin-film, enable isothermal conditions where molecular kinetics limit product formation rather than heat transfer by conduction and/or convection. Thus, these reaction conditions are vital for understanding pyrolysis kinetics and mechanisms.

Despite the previous efforts to develop a full map of the pyrolysis reaction network, a significant problem arises from the experimental data used to validate computational models. Currently, experimental data utilize thermogravimetric analysis (TGA) and/or micropyrolysis-gas chromatography-flame ionization detector or mass spectrometry (μPy-GC–FID or MS) [13-16,22-27,41-44]. The inherent flaws in these instruments for empirical measurements are necessary to note. TGA operates at much slower heating rates (1-150 °C min^{-1}) compared to fast pyrolysis heating rates (>>1,000 °C min^{-1}), and thus can only predict mass volatilization rates for cellulose [41]. The rapid heating rate involved during fast pyrolysis conditions results in greater ambiguity and complexity of mechanistic and kinetic information. GC–FID and MS are traditionalyl combined to quantify final product yields and identify only those products present in the database or commercially available, respectively. Another concern is electron ionization

(EI) used for GC–MS that causes extensive fragmentation of most carbohydrate molecules without prior derivatization. A recent publication from Kenttämaa and co-workers utilized a soft ionization to investigate primary and secondary products of carbohydrates [45]. They reported a molecular species assigned as $C_8H_{14}O_7$ that had not been described as a pyrolysis product in literature. Traditional MS methods cannot detect compounds larger than levoglucosan (C6 compound), and their discovery of a C8 compound as a potential primary pyrolysis product highlights the need for better detection and instrumentation methods for nonvolatile and intermediate compounds that could influence reaction pathways.

To our knowledge, only a handful of studies in literature could be found utilizing "real-time monitoring" of pyrolysis products [17,46-48]. These studies generally utilized flow tube reactors inserted into the ion source of a molecular beam mass spectrometer (MBMS) or light path of a Fourier transform−infrared (FTIR) spectrometer for detection and measurement of evolved gases. Evans and co-workers performed kinetic analysis using MBMS for real-time detection of primary, secondary, and tertiary pyrolysis products from levoglucosan, HMF, glycolaldehyde, and cellulose [46]. Shafer and co-workers also utilized a flow tube reactor coupled with FTIR to monitor low molecular weight gases during cellulose pyrolysis [17]. The flow tube reactor system closely resembles TGA due to the slow heating rates, and therefore poorly represents conditions found during fast pyrolysis. There is an additional drawback of the heated housing zone for the resistively heated filament that could potentially produce unwanted volatilization or sample denaturing, and thus chemically alter the sample prior to thermochemical degradation [49].

In the current study, we address limitations hindering better understanding of pyrolysis chemistry by utilizing an analytical platform that couples micropyrolysis with rapid-scanning

soft ionization HRMS for real-time monitoring of molecular species. Furthermore, we have improved upon the thin-film pyrolysis technique to significantly reduce mass transport effects. Time evolution plots of molecular products from thin-film pyrolysis of glucose-based carbohydrates could be compared and utilized for understanding their thermal degradation. Our results suggest hydrogen bonding is a necessary consideration for modeling and kinetics and that cyclodextrin may not be a good surrogate for studying cellulose due to observed differences in their real-time data.

Experimental Section

Materials and thin-film preparation

Levoglucosan (1,6-Anhydro-β-glucopyranose, Sigma-Aldrich), glucose (Sigma-Aldrich), cellodextrins (cellobiose from Fluka, cellotetraose from Santa Cruz Biotechnology, and cellotriose and cellopentaose from Carbosynth), α-cyclodextrin (Sigma-Aldrich), and cellulose (Sigmacell Type 20, degree of polymerization of ~209 [50]) were purchased at the highest available purity. The samples were dissolved or suspended in water (Fluka LC-MS ChromaSolv) at a concentration of 1 mg mL^{-1}. Thin-films were prepared by transferring 0.5 µL of solution (0.5 µg sample loading) to a 4 x 8 mm (diameter x height) cylindrical pyrolysis cup. The cups were placed under light vacuum at room temperature for 1 min to remove water which left a thin-film estimated to be ~1 µm thick for cellulose.

An initial concern was mineral contaminations that have been reported to affect fast pyrolysis product distributions at concentrations as low as 6 µmol per gram cellulose (~0.05 wt%), particularly alkaline salts such as NaCl and $CaCl_2$ [26]. Furthermore, sodium can leach from glass at concentrations of 2-10 µM, hence all samples were prepared in Teflon vials [51].

Prior to thin-film preparation, metal contaminants were quantified using inductively coupled plasma optical emission spectroscopy (PerkinElmer Optima 8000) and the results are shown in Table S1. Briefly, all metal contaminations are well below the reported threshold level [26]. Cellulose was observed to have the highest concentrations of metal contaminants, which we reduced even further by washing with water and drying overnight at 35 °C. The washed cellulose was used for all subsequent experiments while all other samples were used as received.

Pyrolyzer–TOF MS experiments

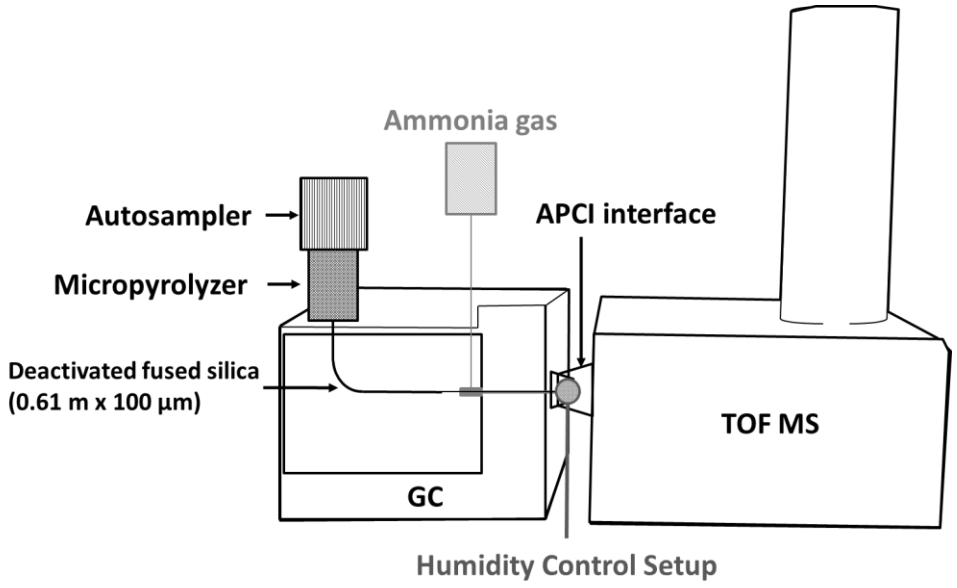

Figure 1. A schematic of the instrument used for real-time monitoring of pyrolysis products. A detailed schematic of the humidity control setup can be found in Fig. S1 of the supplementary information.

Thin-film pyrolysis was studied using a micropyrolyzer–time-of-flight mass spectrometer (µPy-TOF MS) shown in Fig. 1. Pyrolysis cups (deactivated stainless steel) were dropped into a microfurnace pyrolyzer (Frontier Laboratories AS-1020E auto-shot sampler and 3030S micropyrolyzer, Fukushima, Japan) at a preheated furnace temperature ranging from 400-600 °C.

Pyrolysis vapors were carried by ultrahigh purity He at a column flow rate of 1 mL min^{-1} through the shortest possible deactivated fused silica transfer line from the GC inlet (Agilent 7890A, Palo Alto, CA, USA) to the dopant-assisted atmospheric pressure chemical ionization (dAPCI) source. An inlet split ratio of 100:1 is used and the micropyrolyzer interface, GC inlet and oven, and APCI interface operate at 280 °C to prevent condensation. Products were softly ionized by dAPCI and detected using a high resolution Agilent 6200 TOF MS (m/Δm ~7000 at *m/z* 200) that scanned over a mass range of *m/z* 60-1000 at 20 Hz (0.05 s cycle time). APCI is a "soft" ionization technique that we have further modified to improve signal, which is described elsewhere [52]. Briefly, preheated ammonia (500 ppm in He; Praxair, Dansbury, CT, USA) flows into the source chamber at 1 mL min^{-1} as a sheath gas and is then converted to ammonium by corona discharge operating at 1 kV. Ion attachment of ammonium with labile carbohydrate–type compounds prevents fragmentation and increases ionization efficiency (see Fig. 2 of ref. 52). Furthermore, the humidity control setup (Fig. S1) also improves ionization by infusing N_2-bubbled water vapor directly into the source to maintain a constant humidity.

Semi-quantification and data analysis

Isotopically labeled $^{13}C_6$-levoglucosan was purchased from Omicron Biochemicals (>99% ^{13}C atom) for semi-quantification of pyrolysis products. Linear regression analysis for each pyrolysis temperature was performed in triplicate for thin-film loading weights ranging from 0.005-0.1 µg. A linear regression curve example is shown in Fig. S2 for 500 °C. All linear regression slopes had correlation coefficients greater than 0.99. Data analysis used MassHunter Qualitative Data Analysis software (Agilent) for extracted ion chromatograms (EICs) based on the exact mass of $^{13}C_6$-levoglucosan (*m/z* 186.107, $^{13}C_6H_{10}O_5+NH_4^+$) and also for individual ion

peaks of interest. Integrated peak area values were exported into Excel to generate a calibration curve and subsequent linear regression analysis could semi-quantify product yields. Product yields were normalized on a percent of initial carbon basis (%C) for comparison with literature. All samples were pyrolyzed at least in triplicate for each pyrolysis temperature.

Results and Discussion

Mass transport effect and time-zero calibration

For real-time monitoring of molecular products, it is crucial to examine the stepwise events contributing to time-dependent detection within our system. We consider the start time to occur when the pyrolysis cup reaches the bottom of the pre-heated furnace. The heating time of the cup and sample to pyrolysis temperature will require < 0.02 s. Sample heating time (< 5 ms) is ignorable due to thin-film samples [41,42]. Sample pyrolysis time will be dependent on chemical kinetics and affected by the rate determining step. Sample evaporation time should be extremely fast (< 0.001 s), and we assume it can be ignored or at least accounted for using levoglucosan. Another event includes the residence time of the vapors escaping the reactor zone and will be affected by carrier gas flow rate (101 mL min^{-1}) and mass transport effects. Vapor escape time is estimated at ~0.35 s, although we demonstrate below the importance of sample spotting location. The final time contribution arises from dead time in the transfer line and MS. We calculated the dead time of the deactivated fused silica to be ~0.29 s based on the linear velocity and volume. MS dead time is ignored under the assumption that "soft" ionization events will quench products from further reactions. Although it cannot be completely ruled out, eluting analytes undergo millions of soft collisions at atmospheric pressure that will significantly reduce their internal energy and result in ammonium adduction with minimal fragmentation. The total

time without any pyrolysis event sums to ~0.66 s. To account for the total time in our platform and calibrate for sample pyrolysis times, we used thin-film levoglucosan standard that should not undergo pyrolysis but instead rapidly evaporate.

It was first important to reduce mass transport effects that increased vapor escape time and diffusion broadening. The autosampler and micropyrolyzer (Fig. 1) were synchronized with the GC programmed for 1 min isothermal runs per sample cup at 280 °C during continuous acquisition by the TOF MS. This system enabled consistent drop times between sequential cups. Fig. 2 shows the EICs of $^{13}C_6$-levoglucosan thin-film pyrolysis at 500 °C for consecutive cups where the thin-film location of the second cup is changed. The "time lag" caused by mass transport effects could be quantified based on the observed elution time difference (Δt) between the peak maxima. There is a 0.2 s difference between Fig. 2A and 2B and a threefold increase to 0.6 s between Fig. 2A and 2C, the latter of which represents the conventional technique where the sample is located inside the cup. A similar threefold increase is also observed for the full width at half maximum (FWHM) between Fig. 2A and C (~0.2 s to ~0.6 s, respectively), whereas the peak broadening in Fig. 2B is negligible compared to 2A. Elution delay and diffusion broadening are likely caused by turbulence from the carrier gas flow as it circulates around the opening of the pyrolysis cup and hinders the escape of vapor products. Thus, spotting thin-film samples either on the bottom or outside lip of the cup would result in a significant reduction of mass transport artifacts.

Fig. 2 also demonstrates our time-zero (t_0) calibration method for pyrolysis times. As previously described, isotopic levoglucosan is expected to have zero pyrolysis time and desorption time that is at least an order of magnitude faster than our time resolution. Therefore, we assumed the elution of levoglucosan would account for the total time in our system, and

compounds eluting afterwards derived from pyrolysis reaction events. The t_0 for real-time monitoring was then determined by adding the Δt to the peak maximum from levoglucosan thin-film spotted on the first cup. EICs for selected product ions based on exact mass were calibrated for t_0 to produce time evolution profiles for comparison.

Determination of ideal thin-film spotting location

Thin-film samples located inside the cup were ignored since mass transport produces significant time delay and diffusion broadening artifacts that could negatively impact real-time monitoring and kinetic information. Glucose thin-films spotted on the bottom and outside lip of the cup were investigated to determine the effects of the ~0.2 s time delay difference. Fig. 3 shows time evolution profiles (i.e., time-zero calibrated EICs) for $C_6H_{10}O_5$ (red) assigned as levoglucosan and $C_6H_{12}O_6$ (blue) obtained from glucose pyrolysis at 500 °C for comparison of spotting location between the bottom (left panel) and outside lip (right panel) of the cup. It is readily apparent that even a minor increase of residence time can affect product distribution. $C_6H_{12}O_6$, corresponding to glucose or possibly fructose, was detected in high abundance (relative peak intensity in arbitrary units) ranging from 50-100% relative to levoglucosan when spotted on the bottom of the cup. At pyrolysis temperatures exceeding 400 °C, glucose monomer is not expected to survive, and has been described to decompose at temperatures as low as 200 °C [53]. Its detection signifies two possibilities. The first possibility is incomplete pyrolysis due to rapid evaporation of the monomer unit that is then ionized and detected still intact. At room temperature and pressure, glucose is nonvolatile and therefore lacks a vapor pressure. However, Oja and Suuberg were able to measure the vapor pressure of glucose when heated to 133 °C [54]. They also suggest glucose could be permitted to evaporate if sufficiently and rapidly heated to

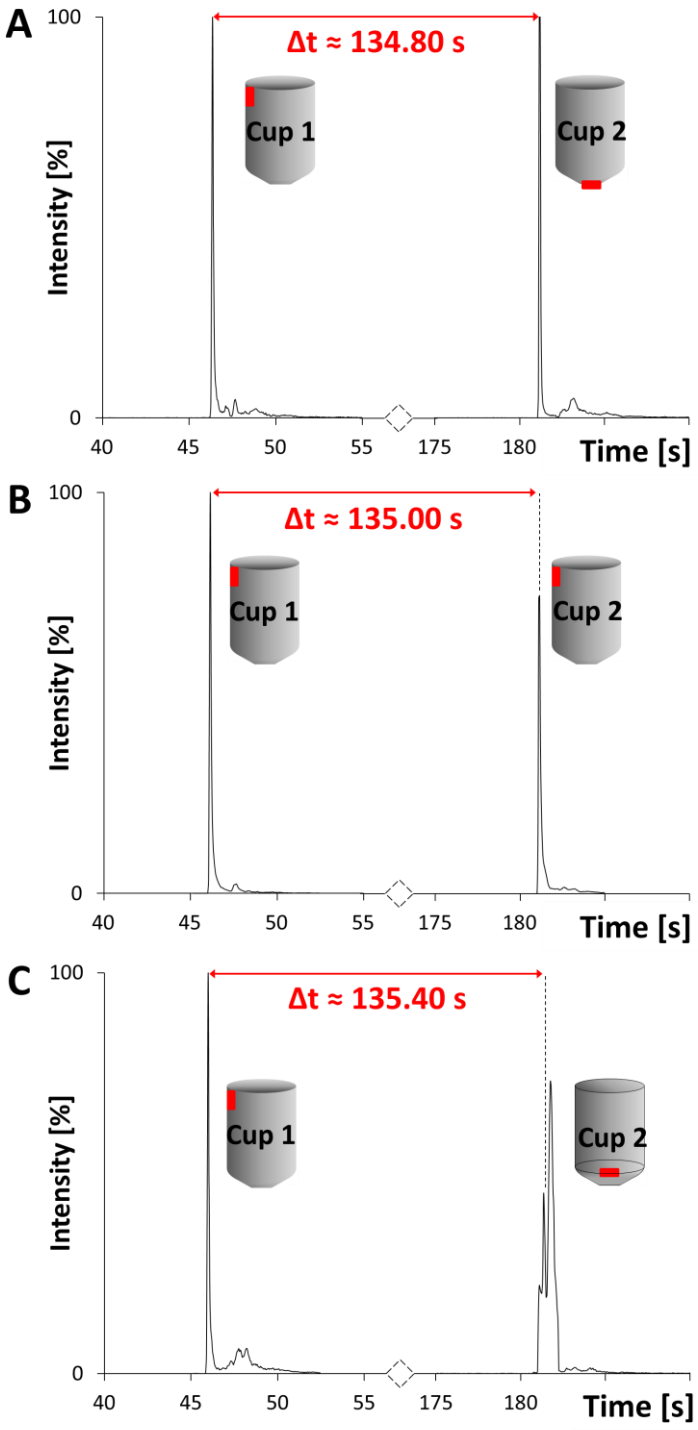

Figure 2. EICs of isotopically labeled $^{13}C_6$-levoglucosan ($^{13}C_6H_{10}O_5$+NH_4^+, *m/z* 186.10) from thin-film pyrolysis at 500 °C showing the elution time difference (Δt) when the spotting location (red mark) is changed for cup 2: **(A)** outside lip → outside bottom, **(B)** outside lip → outside lip, and **(C)** outside lip → inside bottom. The time difference (Δt) is calculated by peak maximum except for **(C)** due to peak broadening and irregularity, which is an average value based on the approximate peak center. Triplicate runs were performed for all time differences.

temperatures within pyrolysis applications.

The second possibility is the detection of the fructose intermediate that has been described as a kinetically favorable initial degradation step (E_a ~36 kcal mol^{-1}) that eventually leads to 5-hydroxymethylfurfural (HMF) production [33,34,40,55]. This so-called "via fructose" pathway is slightly less favorable compared to dehydration reactions to form levoglucosan which is estimated to be 34 kcal mol^{-1} [35]. Our experimental data offers some support for this mechanism. Deeper inspection of the time evolution profiles for levoglucosan and $C_6H_{12}O_6$ shows levoglucosan was detected slightly earlier, whereas HMF ($C_6H_6O_3$, not shown) is slightly after $C_6H_{12}O_6$, which would occur since HMF is produced after multiple dehydration reactions for this reaction pathway.

It should be noted that mass spectrometric detection cannot distinguish structural isomers. Tentative assignments were determined by direct chemical composition assignment using accurate mass information and compared to major products identified in literature. This drawback prevents us from being able to discern $C_6H_{12}O_6$ as glucose or fructose. In fact, the two possibilities may not be mutually exclusive, and the ambiguity served to blur any conclusions concerning pyrolysis data obtained from thin-films spotted on the bottom of the cup. The time evolution profiles obtained from samples spotted on the outside lip were comparable to those from inside the cup but lacked the mass transport artifacts described above. Therefore, all subsequent pyrolysis data was performed by spotting thin-film samples on the top outside lip of the pyrolysis cup to ensure complete pyrolysis, and t_0 calibration for time evolution plots was based on $\Delta t = 135.00 \pm 0.05$ s shown in Fig. 2A.

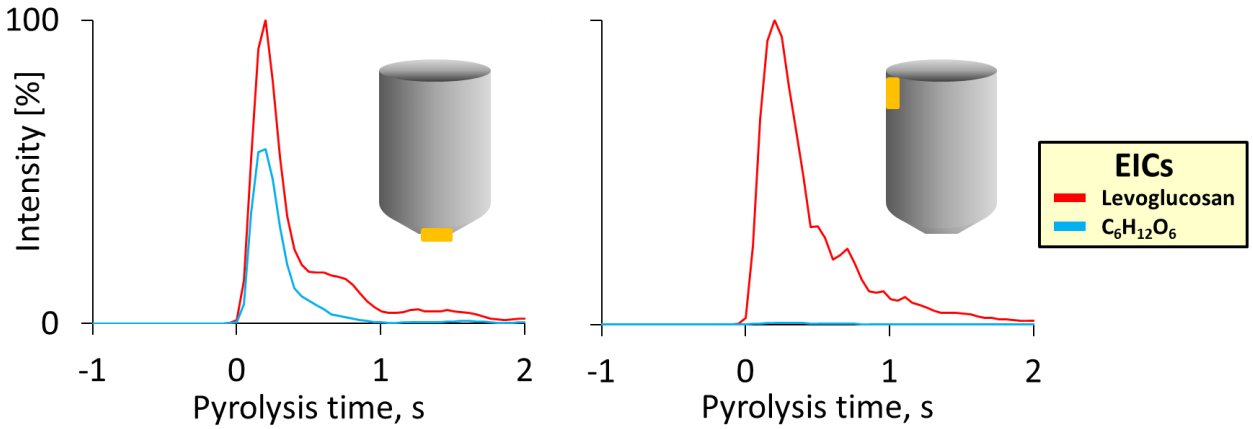

Figure 3. Time evolution profiles of levoglucosan (red) and $C_6H_{12}O_6$ (blue) corresponding to glucose or fructose from thin-film glucose pyrolysis at 500 °C for comparison of sample located outside bottom (left panel) and outside lip (right panel) of the cup. Time calibration for each location used corresponding Δt values from Fig. 2A and B.

Time evolution of molecular products

Glucose-based carbohydrate thin-films were pyrolyzed at 500 °C for real-time monitoring of molecular species based on increasing degree of polymerization (DP). Fig. 4 shows time evolution profiles comparing glucose (DP = 1), cellobiose (DP = 2), cellotriose (DP = 3), cellotetraose (DP = 4), and cellopentaose (DP = 5) for select pyrolysis products. Most profiles are from major products observed in the mass spectra, although a few are well-established products from literature, e.g., HMF, or potential intermediate/metastable products, e.g., $C_8H_{14}O_7$ (molecular weight of 222) recently described as a major product of cellobiose pyrolysis [48].

Several distinct features of the time evolution profiles should be noted for better understanding. First, the dominant product from glucose pyrolysis is $C_3H_6O_3$ (dashed dark green line) that is tentatively assigned as glyceraldehyde (GLA) or thermodynamically stable dihydroxyacetone (DHA), whereas $C_6H_{10}O_5$, assigned as levoglucosan (solid light green line), is most dominant for all other polymer chains having DP > 1. The dominance of levoglucosan from polymeric glucose compared to minimal yields from glucose monomer is in good agreement

with previous thin-film and powder pyrolysis experiments [41]. However, GLA/DHA from glucose pyrolysis is generally not reported for yields obtained using GC–MS/FID. Instead, the dominant molecular species identified and quantified in previous GC–MS are HMF, glycolaldehyde (GA), and methylglyoxal that are weakly abundant within our experimental data for real-time monitoring (see Fig. S3 and S4 for yields of select products by temperature and DP, respectively). The differences observed between final products reported in literature and our real-time data suggest molecular product monitoring in real-time is required to unravel the complexity of pyrolysis chemistry.

A second observation is the increasing shift in pyrolysis time for the detection of levoglucosan by DP. The peak maximum of levoglucosan from glucose is achieved after 0.20 s whereas the time is increasing to 0.40 s for cellopentaose. The relationship of longer pyrolysis times and DP has not been described in literature to the best of our knowledge, but could be observed through real-time monitoring. In previous modeling, computationally calculated activation energies for end-chain initiation and depropagation use the same value of ~51.5 kcal mol^{-1} for maltohexaose, cellobiose, and cellulose, but with frequency factors (A, s^{-1} or M^{-1} s^{-1}) that lumped maltohexaose and cellobiose together [35]. Our real-time monitoring data demonstrated that kinetic values should be “de-lumped” and separated on a per sample basis.

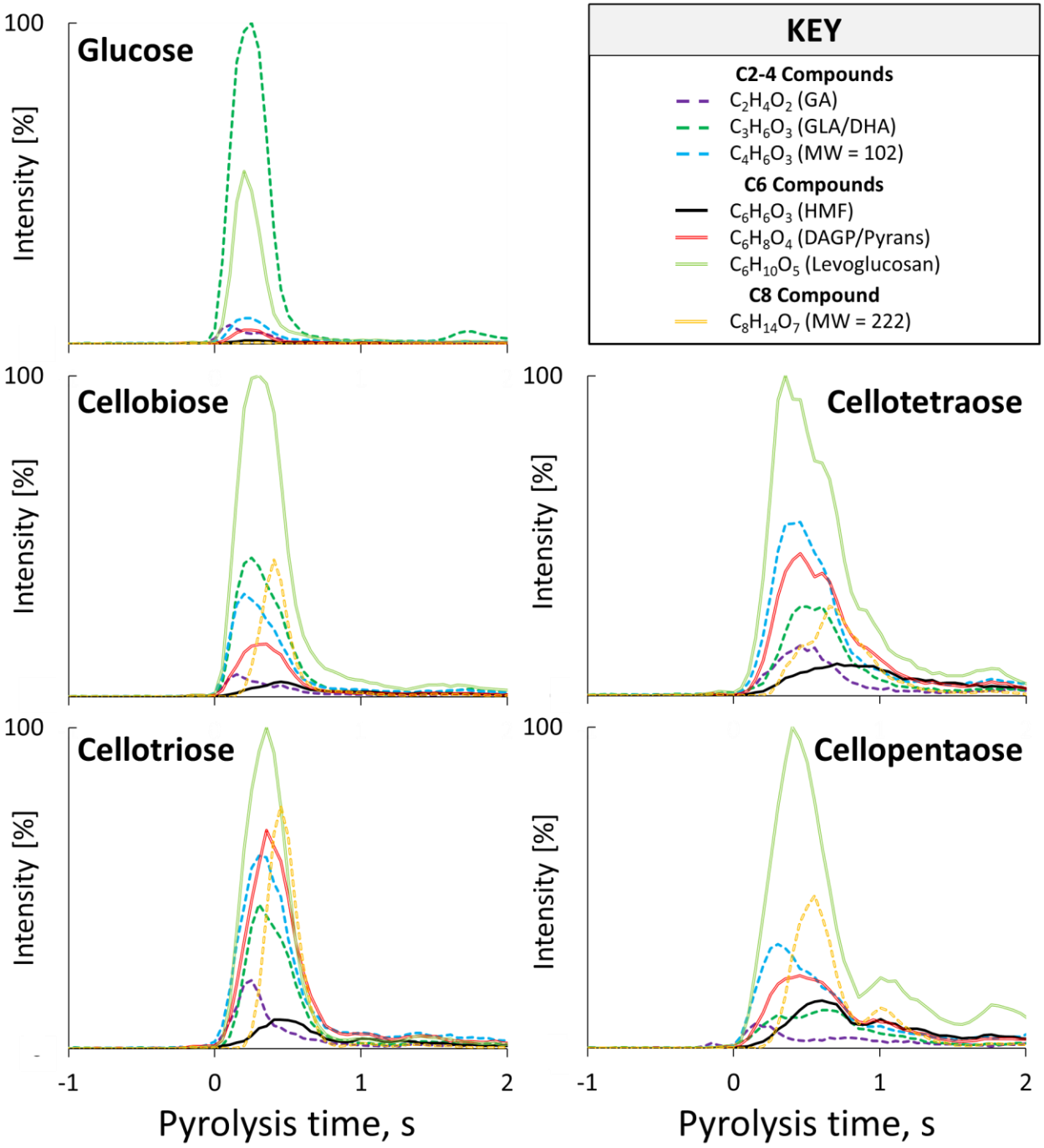

Figure 4. Comparison of time evolution profiles obtained from thin-film pyrolysis at 500 °C for glucose and glucose-based carbohydrates with DP values from 1 to 5. Seven molecular products are shown for their time-dependent detection.

A final feature of merit is the time-dependent detection of $C_8H_{14}O_7$ (molecular weight of 222) that was identified as glucopyranosyl-β-glycolaldehyde by Kenttämaa's group using spectral comparison of its fragmentation pattern with previously published data of the synthetic compound [56]. It should be noted that other large carbohydrate-like nonvolatile compounds were also detected, but are not shown here since $C_8H_{14}O_7$ is the most abundant C_{6+n} compound (i.e., species with a higher carbon number than the monomeric unit). The time evolution profiles of $C_8H_{14}O_7$ shown in Fig. 4 further illustrate the advantages of our analytical platform to detect and monitor these large nonvolatile compounds in real-time. Since the thin-films are well within the isothermal, kinetically limited zone, time-dependent detection should correlate to the chemical kinetics of each molecular species. This C8 compound is detected ~0.15 s after most other peaks. It is reasonable to believe the formation of compounds containing more than six carbons have much higher activation energies caused by ring opening reactions of the reducing end and would explain the time delay in detection.

Fig. 5 shows time evolution profiles comparing glucose, α-cyclodextrin (CD), and cellulose pyrolysis at 500 °C. There are several important observations when comparing these profiles. First, molecular species are detected in high abundance well after 0.5 s for CD and nearly 1 s for cellulose with the greatest peak intensities occurring nearly 1.5 s after pyrolysis, in contrast to glucose at ~0.2 s. This significant time delay likely derives from breakage of hydrogen bonding, which would be much more significant in CD and cellulose than small chain glucose polymers. CD is able to form six interglucose hydrogen bonds [57]. It would be possible to verify the effects of hydrogen bonding by comparing the time evolution of α-, β-, and γ-cyclodextrin, which have increasing hydrogen bond strengths by glucose monomer (α: 6 < β: 7 < γ: 8) and therefore expected to have increasing detection times, respectively. The effects of

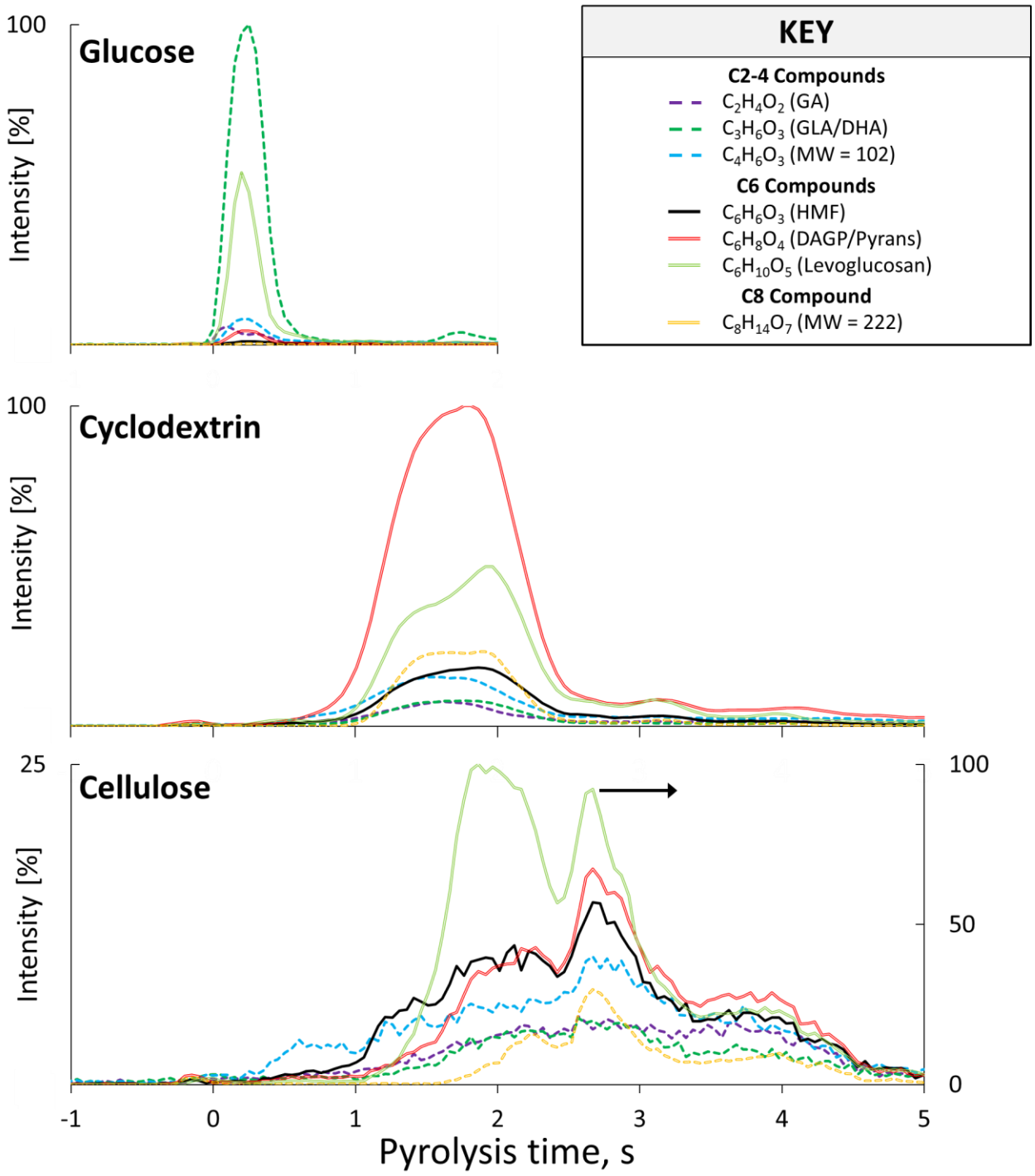

Figure 5. Comparison of time evolution profiles obtained from thin-film pyrolysis at 500 °C for glucose, α-cyclodextrin, and cellulose. Seven molecular products are shown for their time-dependent detection.

hydrogen bonding might also explain the observation in Fig. 4 that increasing DP and thus hydrogen bonding to a smaller extent cause the incremental time delay. Our results suggest that hydrogen bonding may be a significant factor in cellulose pyrolysis chemistry that has been previously ignored in mechanistic modeling, and further work is required for verification.

Another distinct feature observed in Fig.5 is the peak profile difference between CD and cellulose. The profile in CD more closely resembles the Gaussian-like distribution observed in glucose chains (Fig. 4), whereas cellulose has an apparent bimodal distribution. The peak valley at ~2.5 s, which is most exaggerated for time evolution of levoglucosan, could potentially represent a phase transition where the initial peak represents surface pyrolysis and the latter from a molten phase. We have seen an amplified bimodal peak distribution for cellulose powder pyrolysis (shown in Fig. S5) that offers further support to the phase transition hypothesis.

Another key difference is the dominance of $C_6H_8O_4$ relative to levoglucosan in cyclodextrin compared to those observed for cellulose. $C_6H_8O_4$ is tentatively identified as DAGP but two pyrans with matching chemical compositions as DAGP have been previously reported and were included as possible structural isomers [41,42]. Semi-quantification (Fig. S3 and S4) indicated CD had twice the yield of DAGP/Pyrans and about half the yield of levoglucosan compared to cellulose (14% to 7% and 10% to 22%, respectively). One of the pyran compounds, identified as 1,5-anhydro-4-deoxy-ᴅ-glycero-hex-1-en-3-ulose (ADGH), was reported in higher yields in CD than cellulose (5.2% to 3.2% in cellulose). Even if we removed a comparable percent to account for both pyrans, DAGP from CD would still be more abundant. Surprisingly, these specific pyrans were ignored in Dauenhauer's studies despite their reported yields being fairly significant. Furthermore, six carbon pyrans have not been incorporated into the most recent mechanistic modeling of cellulose despite their identification [23,24]. The cyclic structure of CD

provides several possibilities for the formation of DAGP and pyrans. Mid-chain dehydration reactions could occur prior to glycosidic bond cleavage followed by another water loss during depropagation. Ring opening following glycosidic bond cleavage could potentially lead to pyranic compounds. Interestingly, a pyran compound with nearly matching structure as ADGH could be formed by adding a ring closing step to the reaction mechanism described by Schwarzinger et al. for cellobiose [Fig. 7 from ref. 58]. A similar ring opening reaction mechanism was recently used to describe the formation of $C_8H_{14}O_7$, which we also observed in high yields for CD pyrolysis [59].

The idea that cyclodextrin would be an ideal low molecular weight surrogate to study cellulose pyrolysis has been around for over a decade [60]. Recently, Dauenhauer and co-workers used more experimental and computational evidence to support this claim [41]. Their postulation derived from nearly matching product yields across a variety of experimental conditions, e.g., powder, thin-film, and TGA, and end-group-to-monomer ratio (cyclodextrins: 0, cellulose: 0.01-2%). However, CD does not appear to be a good surrogate to study cellulose based on differences observed in real-time data.

Conclusions

A major road block to the complete understanding of pyrolysis chemistry has been the lack of instrumentation capable of providing useful experimental information for molecular product formation and corresponding chemical kinetics. In the current study, we have developed novel instrumentation and applied it towards accomplishing this goal. Micropyrolysis coupled with soft ionization, rapid scanning HRMS was utilized for monitoring of molecular products formed in real-time from the pyrolysis of thin-film glucose and glucose-based carbohydrates.

Our analytical technique was developed to significantly reduce mass transport artifacts, generate time evolution plots for individual pyrolysis species, and provide semi-quantitative yields. The combination of this data enabled us to probe thermochemical conversion of cellulose by building a foundation from glucose and glucose-based carbohydrates. More work and data analysis is necessary for better understanding, particularly towards achieving kinetic information. For example, deconvolution of our time evolution profiles using the time profile of levoglucosan as the sharpening function should theoretically remove peak diffusion caused by laminar flow, which should enable greater accuracy for determining kinetic parameters for comparison to computational values.

Acknowledgment

DPC acknowledges partial support from NSF EpSCOR seed grant.

References

[1] Czernik, S.; Bridgwater, A.V. *Energy Fuels* **2004**, 18, 590–598.

[2] Mohan, D.; Pittman, C.U.; Steele, P.H. *Energy Fuels* **2006**, 20, 848–889.

[3] DOE, *Conversion Technologies for Advanced Biofuels: Preliminary Roadmap & Workshop Report*, Arlington, VA: **2011**.

[4] Talmadge, M.S.; Baldwin, R.M.; Biddy, M.J.; McCormick, R.L.; Beckham, G.T.; Ferguson, G.A.; Czernik, S.; Magrini-Bair, K.A.; Foust, T.D.; Metelski, P.D.; Hetrick, C.; Nimlos, M.R. *Green Chem.* **2014**, 16, 407–453.

[5] Bridgwater, A.V. *Biomass Bioenergy* **2012**, 38, 68–94.

[6] Elliott, D.C.; Baker, E. In *Energy from Biomass and Wastes X*, Klass, D. (ed.), I.G.T.: **1983**, 765–782.

[7] Blin, J.; Volle, G.; Girard, P.; Bridgwater, A.V.; Meier, D. *Fuel* **2007**, 86, 2679–2686.

[8] Cottam, M.-L.; Bridgwater, A.V. *Biomass Bioenergy* **1994**, 7, 267–273.

[9] Smith, E.A.; Lee, Y.J. *Energy Fuels* **2010**, 24, 5190–5198.

[10] Smith, E.A.; Park, S.; Klein, A.T.; Lee, Y.J. *Energy Fuels* **2012**, 26, 3796–3802.

[11] Cole, D.P.; Smith, E.A.; Dalluge, D.; Wilson, D.M.; Heaton, E.A.; Brown, R.C.; Lee, Y.J. *Fuel* **2013**, 111, 718–726.

[12] Cole, D.P.; Smith, E.A.; Lee, Y.J. *Energy Fuels* **2012**, 26, 3803–3809.

[13] Broido, A.; Nelson, M.A. *Combust. Flame* **1975**, 24, 263–268.

[14] Bradbury, A.G.W.; Sakai, Y., Shafizadeh, F. *J. Anal. Appl. Pyrolysis* **1979**, 23, 3271–3280.

[15] Argawal, R.K. *Can. J. Chem. Eng.* **1988**, 66, 403–412.

[16] Argawal, R.K. *Can. J. Chem. Eng.* **1988**, 66, 413–418.

[17] Banyasz, J.L.; Li, S.; Lyons-Hart, J.L.; Shafer, K.H. *J. Anal. Appl. Pyrolysis* **2001**, 57, 223–248.

[18] Diebold, J.P. *Biomass Bioenergy* **1994**, 7, 75–85.

[19] Ranzi, E.; Cuoci, A.; Faravelli, T.; Frassoldati, A.; Migliavacca, G.; Pierruci, S.; Sommariva, S. *Energy Fuels* **2008**, 22, 4292–4300.

[20] Antal Jr., M.J.; Varhegyi, G. *Ind. Eng. Chem. Res.* **1995**, 34, 703–717.

[21] Anex, R.P.; Aden, A.; Kazi, F.K.; Fortman, J.; Swanson, R.M.; Wright, M.M.; Satrio, J.A.; Brown, R.C.; Daugaard, D.E.; Platon, A.; Kothandaraman, G.; Hsu, D.D.; Dutta, A. *Fuel* **2010**, 89, S29–S35.

[22] Vinu, R.; Broadbelt, L.J. *Energy Environ. Sci.* **2012**, 5, 9808–9826.

[23] Zhou, X.; Nolte, M.W.; Mayes, H.B.; Shanks, B.H.; Broadbelt, L.J. *Ind. Eng. Chem. Res.* **2014**, 53, 13274–13289.

[24] Zhou, X.; Nolte, M.W.; Shanks, B.H.; Broadbelt, L.J. *Ind. Eng. Chem. Res.* **2014**, 53, 13290–13301.

[25] Patwardhan, P.R.; Satrio, J.A.; Brown, R.C.; Shanks, B.H. *J. Anal. Appl. Pyrolysis* **2009**, 86, 323−330.

[26] Patwardhan, P.R.; Satrio, J.A.; Brown, R.C.; Shanks, B.H. *Bioresour. Technol.* **2010**, 101, 4646−4655.

[27] Patwardhan, P.R.; Dalluge, D.L.; Shanks, B.H.; Brown, R.C. *Bioresour. Technol.* **2011**, 102, 5265−5269.

[28] Paine, J.B., III; Pithawalla, Y.B.; Naworal, J.D.; Thomas, C.E. *J. Anal. Appl. Pyrolysis* **2007**, 80, 297−311.

[29] Paine, J.B., III; Pithawalla, Y.B.; Naworal, J.D. *J. Anal. Appl. Pyrolysis* **2008**, 82, 10−41.

[30] Paine, J.B., III; Pithawalla, Y.B.; Naworal, J.D. *J. Anal. Appl. Pyrolysis* **2008**, 82, 42−69.

[31] Paine, J.B., III; Pithawalla, Y.B.; Naworal, J.D. *J. Anal. Appl. Pyrolysis* **2008**, 83, 37−63.

[32] Richards, G.N. *J. Anal. Appl. Pyrolysis* **1987**, 10, 251−255.

[33] Ponder, G.R.; Richards, G.N.; Stevenson, T.T. *J. Anal. Appl. Pyrolysis* **1992**, 22, 217−229.

[34] Ponder, G.R.; Richards, G.N. *Carbohydr. Res.* **1993**, 244, 27−47.

[35] Mayes, H.B.; Broadbelt, L.J. *J. Phys. Chem. A* **2012**, 116, 7098−7106.

[36] Hosoya, T.; Sakaki, S. *Chem. Sus. Chem.* **2013**, 6, 2356−2368.

[37] Nimlos, M.R.; Blanksby, S.J.; Ellison, G.B.; Evans, R.J. *J. Anal. Appl. Pyrolysis* **2003**, 66, 3−27.

[38] Shen, C.; Zhang, I.Y.; Fu, G.; Xu, X. *Chin. J. Chem. Phys.* **2011**, 24, 249−252.

[39] Vinu, R.; Broadbelt, L.J. *Annu. Rev. Chem. Biomol. Eng.* **2012**, 3, 29−54.

[40] Mayes, H.B.; Nolte, M.W.; Beckham, G.T.; Shanks, B.H.; Broadbelt, L.J. *ACS Sustainable Chem. Eng.* **2014**, 2, 1461−1473.

[41] Mettler, M.S.; Mushrif, S.H.; Paulsen, A.D.; Javadekar, A.D.; Vlachos, D.G.; Dauenhauer, P.J. *Energy Environ. Sci.* **2012**, 5, 5414–5424.

[42] Paulsen, A.D.; Mettler, M.S.; Dauenhauer, P.J. *Energy Fuels* **2013**, 27, 2126–2134.

[43] Lu, Q.; Yang, X.-C.; Dong, C.-Q.; Zhang, Z.-F.; Zhang, X.-M.; Zhu, X.-F. *J. Anal. Appl. Pyrolysis* **2011**, 92, 430–438.

[44] Fabbri, D.; Chiavari, G.; Prati, S.; Vassura, I.; Vangelista, M. *Rapid Commun. Mass Spectrom.* **2002**, 16, 2349–2355.

[45] Kitahara, Y.; Takahashi, S.; Fujii, T. *Chemosphere* **2012**, 88, 663−669.

[46] Shin, E.-J.; Nimlos, M.R.; Evans, R.J. *Fuel* **2001**, 1697−1709.

[47] Mukarakate, C.; Zhang, X.; Stanton, A.R.; Robichaud, D.J.; Ciesielski, P.N.; Malhotra, K.; Donohoe, B.S.; Gjersing, E.; Evans, R.J.; Heroux, D.S.; Richards, R.; Iisa, K.; Nimlos, M.R. *Green Chem*. **2014**, 16, 1444–1461.

[48] Hurt, M.R.; Degenstein, J.C.; Gawecki, P.; Borton II; D.J.; Vinueza, N.R.; Yang, L.; Agrawal, R.; Delgass, W.N.; Ribeiro, F.H.; Kenttämaa, H.I. *Anal*. *Chem*. **2013**, 85, 10927–10934.

[49] Wampler, T.P. In *Applied Pyrolysis Handbook*; 2nd ed., Wampler, T.P. (ed.), CRC Press: Boca Raton, **2006**, 39–40.

[50] Kawamoto, H.; Murayama, M.; Saka, S. *J*. *Wood Sci*. **2003**, 49, 469−473.

[51] Gao, S.; Zhang, Z.-P.; Karnes, H.T. *J*. *Chromatogr*. *B* **2005**, 825, 98−110.

[52] Cole, D.P.; Lee, Y.J. *J*. *Anal*. *Appl*. *Pyrolysis* **2015**, 112, 129−134.

[53] Raemy, A.; Schweizer, T.F. *J*. *Therm*. *Anal*. **1983**, 28, 95−108.

[54] Oja, V.; Suuberg, E.M. *J*. *Chem*. *Eng*. *Data* **1999**, 44, 26−29.

[55] Ponder, G.R.; Richards, G.N. *Carbohydr*. *Res*. **1993**, 244, 341−359.

[56] Fang, T.T.; Bendiak, B. *J*. *Am*. *Chem*. *Soc*. **2007**, 129, 9721–9736.

[57] Saenger, W.; Jacob, J.; Gessler, K.; Steiner, T.; Hoffmann, D.; Sanbe, H.; Koizumi, K.; Smith, S.M.; Takaha, T. C*hem. Rev*. **1998**, 98, 1787–1802.

[58] Schwarzinger, C.; Tanczos, I.; Schmidt, H. *J*. *Anal*. *Appl*. *Pyrolysis* **2002**, 62, 179–196.

[59] Degenstein, J.C.; Murria, P.; Easton, M.; Sheng, H.; Hurt, M.; Dow, A.R.; Gao, J.; Nash, JJ.; Agrawal, R.; Delgass, W.N.; Ribeiro, F.H.; Kenttämaa, H.I. *J. Org. Chem.* **2015**, 80, 1909–1914.

[60] Trotta, F.; Zanetti, M.; Camino, G. *Polym*. *Degrad*. *Stab*. **2000**, 69, 373–379.

Table S1. ICP-OES analysis results of metal contaminations in most glucose-based carbohydrates and cellulose (Sigmacell Type 20) used for the current study. Concentrations of inorganic ions are shown in ppb.

Sample	[Na]	[K]	[Ca]	[Al]	[Mg]
Levoglucosan	-	-	-	4.9	0.6
Glucose	-	-	1.7	3.2	0.5
Cellobiose	-	-	-	-	-
Cellotetraose	49.6	22.4	75.0	-	14.0
Maltose	-	-	-	-	0.1
Maltotetraose	-	-	-	-	0.3
α-Cyclodextrin	-	-	7.8	1.6	2.9
Cellulose (unwashed)	780.1	233.2	57.2	44.7	7.9
Cellulose (washed)	25.6	-	20.4	-	4.8

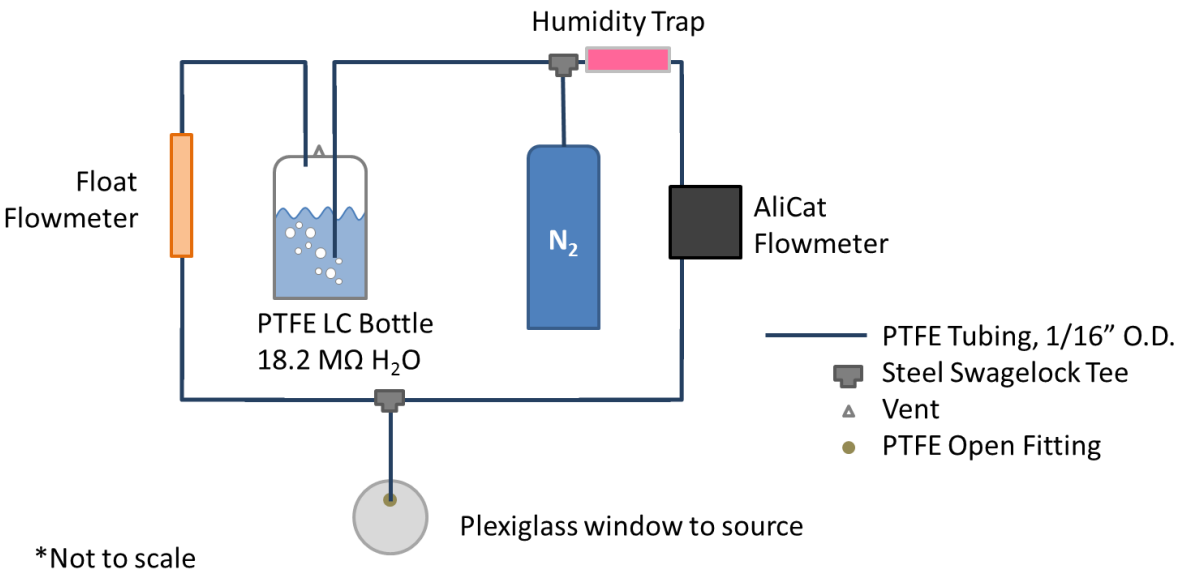

Figure S1. A schematic diagram of the humidity control setup that infuses N_2-bubbled water vapor directly into the source shown in Fig. 1.

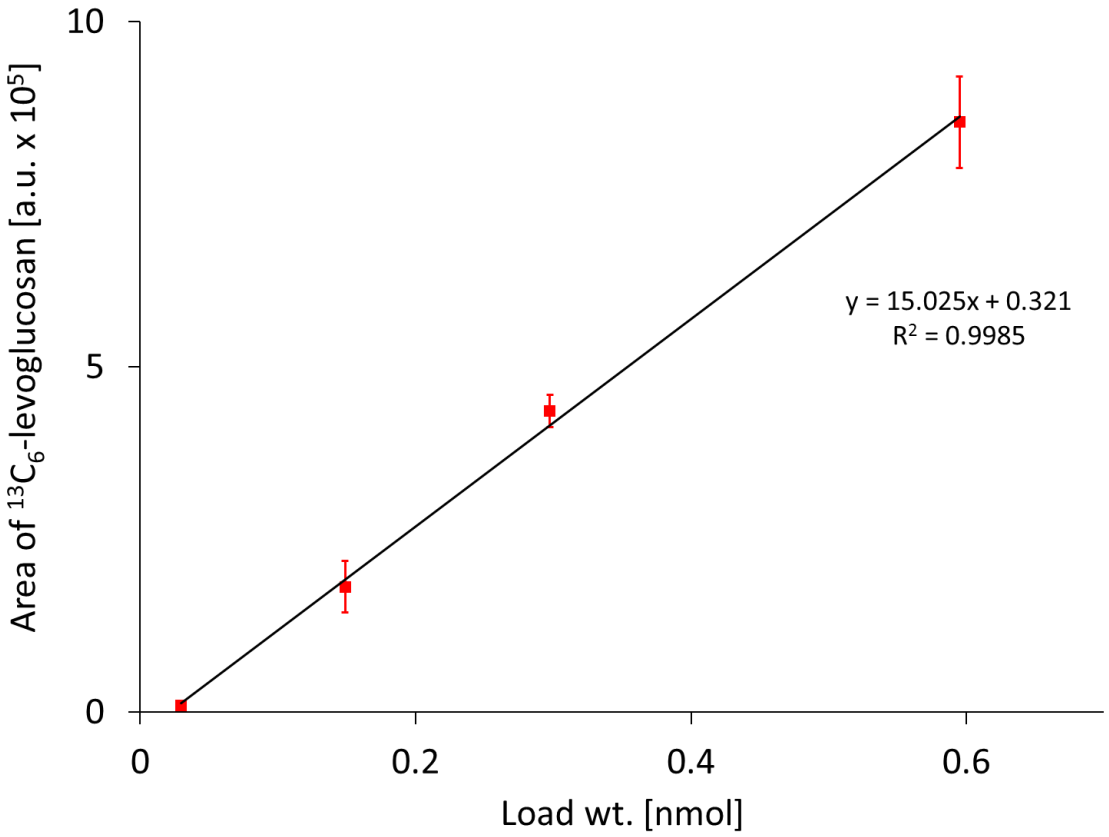

Figure S2. Linear regression analysis from thin-film pyrolysis of $^{13}C_6$-levoglucosan at 500 °C using four different load weights (0.005, 0.025, 0.05, and 0.1 µg) that have been converted to nmol of sample for easier semi-quantitative analysis. Error bars represent a 90% mean confidence interval.

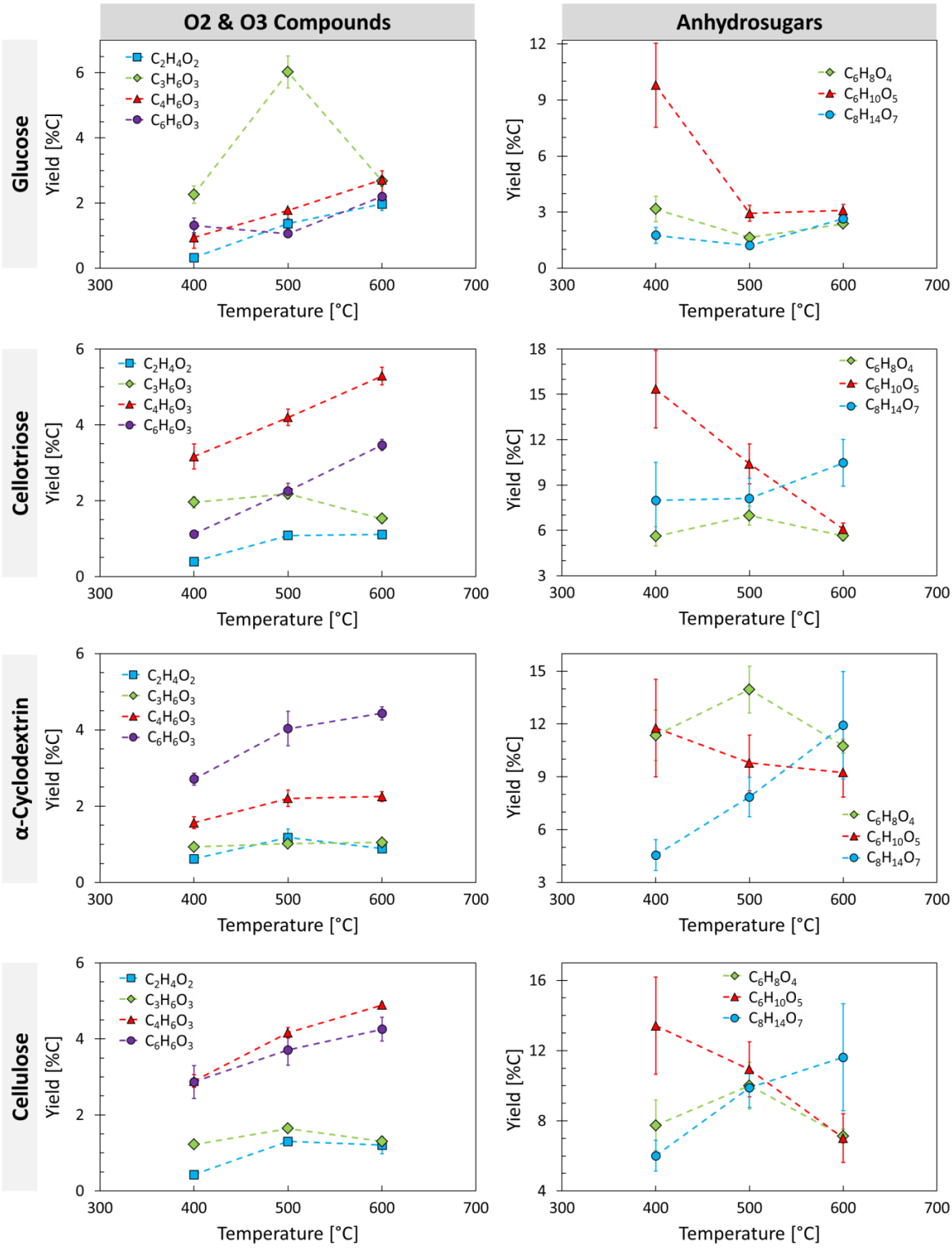

Figure S3. Semi-quantitative yields (in percent of initial carbon) of O2-O3 compounds (left column) and anhydrosugars (right column) based on various pyrolysis temperatures for glucose, cellotriose, α-cyclodextrin, and cellulose (Sigmacell Type 20). Error bars represent 90% mean confidence interval.

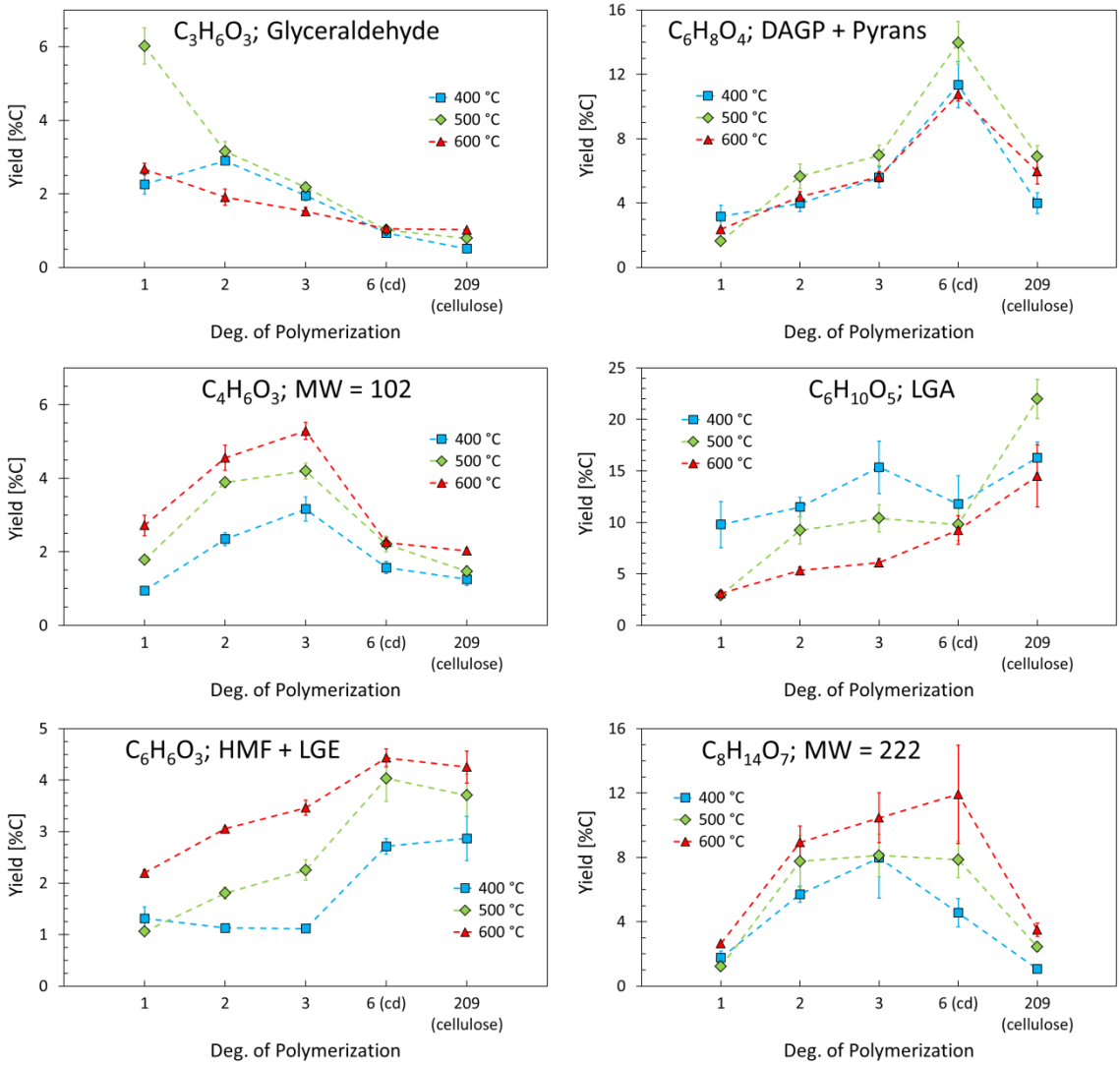

Figure S4. Semi-quantitative yields (in percent of initial carbon) of six individual products showing their dependence by degree of polymerization (DP). Tentative identifications are based on chemical composition assignment from accurate mass and matched with abundant products from literature. Error bars represent 90% mean confidence interval. Abbreviations: HMF, 5-hydroxymethylfurfural; LGE, levoglucosenone; DAGP, 1,4;3,6-dianhydro-α-D-glucopyranose; LGA, levoglucosan.

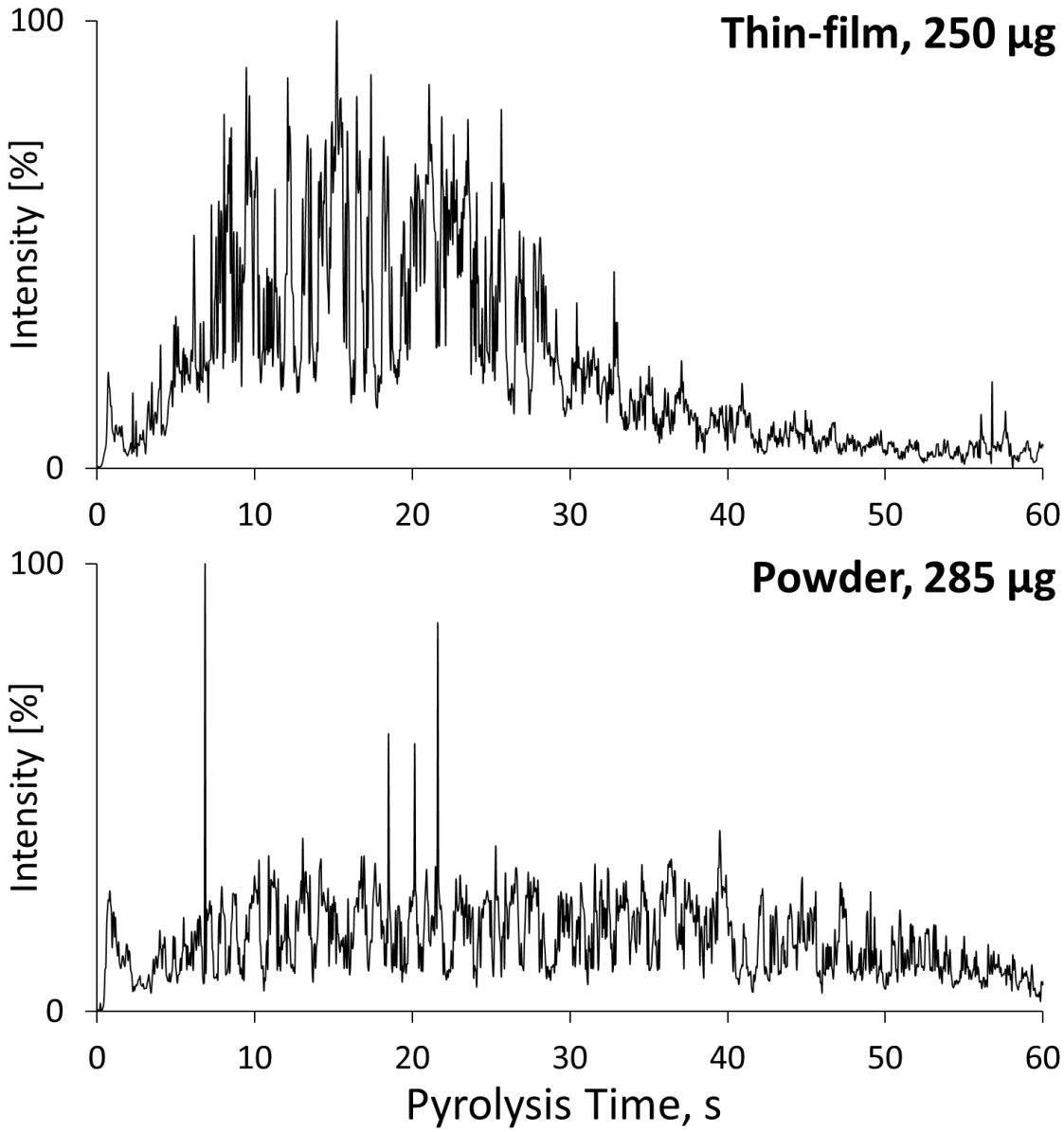

Figure S5. Time evolution profiles of levoglucosan from thin-film (top) and powder (bottom) pyrolysis of Avicel cellulose using sample loading weights similar to those used by Dauenhauer et al. [41,42]. In their studies, they obtained nearly double the yield of levoglucosan for powder pyrolysis. Rough estimation of yield was made based on integrated area of these profiles, and good agreement was found, i.e., thin-film area was half that of powder. Also, two distinct profiles are observed that support a phase transition effect. The first peak eluting within 5 s occurs via surface pyrolysis and the second, extremely broad and spiky distribution from molten phase and subsequent aerosol ejection.

CHAPTER VI
GENERAL CONCLUSIONS

Conclusions

This dissertation presents work that expands the utility of high-resolution mass spectrometry (HRMS) through applications for better understanding of pyrolysis products and kinetics at the molecular level. For example, HRMS was applied to understanding small molecules adsorbed on biochars from various thermochemical processes. In another application, HRMS was able to assign chemical compositions to nearly 300 unique nitrogen-containing species in switchgrass bio-oils, and monitor their change based on harvest month of the switchgrass. A third application demonstrated the usefulness of HRMS for efficiently screening deoxygenation products from catalytic fast pyrolysis. Finally, micropyrolysis coupled with HRMS was developed for real-time monitoring of molecular products that overcame several limitations hindering progress towards understanding the complex pyrolysis chemistry. The rapid scanning and soft ionization capabilities of HRMS, combined with improvements to the thin-film pyrolysis technique, provided ideal experimental and reaction conditions that aid in determining mechanistic and kinetic information.

Future Directions

High-resolution mass spectrometry has been shown in this work to be crucial for molecular-level understanding, and the full extent of this powerful analytical platform has not been achieved. With regard to pyrolysis chemistry, the earliest groundwork has been set for unraveling the complex network of reactions through improvements to the methodologies and instrumentation for real-time monitoring of molecular products.

Chapter 5 was an initial step in piecing together HRMS experimental data with previous literature, but many months, if not years, will be needed to fully understand the enormous amounts of information. Further studies are still needed. For example, as discussed in Chapter 5, hydrogen bonding may play a central role in the thermal degradation of cellulose and has been ignored in computational models. Two possible experiments could be performed to study and verify this hypothesis. The first experiment that was previously discussed would be pyrolysis of α-, β-, and γ-cyclodextrin which have increasing strengths of hydrogen bonding. If the hypothesis is true, real-time detection of molecular products should occur at later pyrolysis times ($\alpha < \beta < \gamma$). Similarly, another study could be performed to test hydrogen bonding effects through modification of hydroxyl side chains on α-cyclodextrin with moieties that enhance or disrupt hydrogen bonding. It would follow then that modified cyclodextrin with the weakest hydrogen bonding should be detected much earlier.

The objective of this work has been the advancement of HRMS into the pyrolysis field. The applications and development of this analytical system demonstrate the continued effort to provide new insight and answers to complex questions. Although the past efforts have been severely hindered by instrumentation, HRMS offers a promising outlook towards achieving a commercially-viable, renewable, and transportable fuel.